

**SEVERE PLASTIC DEFORMATION OF AA2050  
Al-Cu-Li ALLOY BY MULTI-AXIAL FORGING**

Thesis

Submitted in partial fulfilment of the requirements for the degree of

DOCTOR OF PHILOSOPHY

by

**JAGADEESH. C.**



DEPARTMENT OF MECHANICAL ENGINEERING  
NATIONAL INSTITUTE OF TECHNOLOGY KARNATAKA,  
SURATHKAL, MANGALORE - 575025

July, 2024

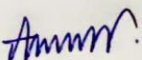


## DECLARATION

I hereby *declare* that the Research Thesis entitled "**SEVERE PLASTIC DEFORMATION OF AA2050 Al-Cu-Li ALLOY BY MULTI AXIAL FORGING**" which is being submitted to the **National Institute of Technology Karnataka, Surathkal** in partial fulfillment of the requirements for the award of the Degree of Doctor of Philosophy in **Department of Mechanical Engineering** is a bonafide report of the research work carried out by me. The material contained in this research thesis has not been submitted to any university or Institution for the award of any degree.

Register Number: **187064ME005**

Name of the Research Scholar: **Jagadeesh C**

Signature of the Research Scholar: 

Department of Mechanical Engineering

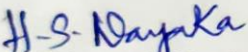
Place : NITK Surathkal

Date : 12-07-2024



CERTIFICATE

This is to certify that the Research Thesis entitled "**Severe Plastic Deformation of AA2050 Al-Cu-Li Alloy by Multi Axial Forging**" submitted by **Mr. Jagadeesh C (Register Number: 187064ME005)** as the record of the research work carried out by him, is accepted as the Research Thesis submission in partial fulfilment of the requirements for the award of the Degree of **Doctor of Philosophy**.

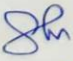
  
Dr. H. Shivananda Nayaka

Research guide

Date: 12-07-2024

Chairman- DRPC

Date:

  
12/7/2024





## ACKNOWLEDGMENT

I would like to express my deepest and heartfelt gratitude to my research supervisor **Dr. H. Shivananda Nayaka**, Professor, Department of Mechanical Engineering, National Institute of Technology Karnataka, Surathkal for unwavering support and guidance throughout this journey. Your insightful feedback and mentorship were invaluable in helping me and I am truly thankful for the opportunity to work with you.

I take this opportunity to express my sincere gratitude to **Dr. S. M. Murigendrappa**, Professor and Head, **Dr. Ravikiran Kadoli**, **Dr. S. Narendranath** and **Dr. Shrikantha S. Rao**, Professors and Former head and all the faculties of Department of Mechanical Engineering, for their continuous help during my stay in NITK.

I also thank the RPAC members, **Dr. Raviraj H. M.** Assistant Professor, Department of Civil Engineering and **Dr. Ramesh M. R.** Professor, Department of Mechanical Engineering for continuously evaluating the work and providing valuable feedbacks throughout my research work.

It is my pleasure to thank **Dr. B. Ravi**, Director, NITK, **K. Umamaheshwar Rao**, Former Director, NITK and **Ministry of Education (MoE)** for the financial support and all other resources provided during my research tennure.

I would like to thank **Dr. Indradev Samajdar**, IITB for providing me with the opportunity to carry out EBSD studies. A special thanks to **Dr. Pruthviraj Shekaran**, PSGT, Coimbatore for helping me with TEM characterizations.

I would like to thank **Dr. H. K. Shivanand**, Professor, U.V.C.E Bangalore for his mentorship and support throughout my carrier.

I am extremely thankful to my fellow researchers at NITK, especially **Mr. Syam Narayan**, **Mr. Karthik Adiga**, **Mr. Naveen Bharadishetter** and **Mr. Arvind G**, for being supportive in all times. A special thanks to my senior labmates, **Dr. Gagannan Anne**, **Dr. Vasu M**, **Dr. Praveen T R**, **Dr. Sachin S** and **Dr. Ramesh Sampath** for your continuous guidance in this journey. I will always be thankful to my fellow labmates **Mr. Vishwanath G**, **Mr. Manoj J**, and **Mr. Ranganath** for being a part of this journey.

I will always be thankful to **Mr. Shailesh** and **Mr. Shashi** from Strength of Materials Lab, **Mr. Kiran** and **Mr. Pradeep**, CRF, NITK for helping me out in successfully executing MDF. I would like to thank all Staff members and chairman of Central Research Facility at NITK for helping me with various instruments for carrying out various characterizations. A special thanks to non teaching staff members from various laboratories for providing various facilities and support.

I wish to express my sincere gratitude to my family for their unwavering belief, prayers, sacrifice and unconditional love. I would also like to extend a special acknowledgment to my father, **Mr. Chandrappa**, and **Mrs. Parvathamma** for their encouragement and never-ending love. This journey wouldn't have been possible without the support of my sister, **Mrs. Prapulla**. Furthermore, I am deeply obliged to my wife, **Mrs. Sindhu K. R.**, for her selfless companionship during all the challenging moments.

**Jagadeesh C**

## ABSTRACT

There is increasing scientific and industrial interest in development of bulk ultra-fine-grained (UFG) alloys intended for structural applications. Multi axial forging (MAF) is one of the simple and most effective methods of severe plastic deformation (SPD) to improve the material properties. Aluminium Copper Lithium (Al-Cu-Li) alloys are known for their lightweight properties and serve as viable substitutes for conventional 2XXX and 7XXX series Aluminium alloys. In this research, we performed MAF on AA2050 Al-Cu-Li alloy and subsequently subject to artificial aging. Our investigation delves into the microstructural characterization, mechanical properties evolution, corrosion properties and wear properties observed during various MAF cycles and post MAF aging.

Microstructural analysis is carried out through various techniques such as optical microscopy, scanning electron microscopy, transmission electron microscopy, electron backscatter diffraction, and X-ray diffraction. Further, mechanical properties are evaluated using tensile and micro hardness tests. Additionally, dry reciprocating wear testing were carried out using a ball-on-disc testing machine for both unprocessed and processed samples. Corrosion properties were evaluated using electrochemical polarization studies with Tafel extrapolation technique to determine corrosion rates.

Microstructural studies revealed fine grain structures with the formation of of large density of deformation bands Upon MAF. Artificial aging of MAF processed samples resulted in a uniform distribution of fine  $T_1$  precipitates in the grain interiors. Microhardness tests shows a significant increase in hardness upto 6 passes with slight increase after 12 passes. With increase in number of MAF passes, enhancement in strength with a trade-off in ductility was observed. Artificial aging of MAF samples showed further increase in strengths, with slight increase in ductility. Overall, an increase in corrosion resistance was observed in all sample upon peak aging, with 12 pass + peak aged samples showing better corrosion resistance. Also, 12 pass MDF processed samples showed better wear resistance.

### **Keywords:**

Severe plastic deformation, Multi axial forging, Al-Cu-Li alloys, Mechanical properties, Corrosion, Wear.



## TABLE OF CONTENTS

<b>LIST OF FIGURES</b>	<b>V</b>
<b>ABBREVIATIONS</b>	<b>X</b>
<b>CHAPTER 1</b>	
<b>INTRODUCTION</b>	<b>1</b>
<b>1.1 Background</b>	<b>1</b>
<b>1.2 Aluminium Alloys</b>	<b>4</b>
1.2.1 Classification of Aluminum alloys	5
1.2.2 Basic concepts of strengthening Aluminum alloys	6
1.2.3 Introduction to Al-Cu-Li alloys	7
<b>1.3 Severe Plastic Deformation</b>	<b>10</b>
1.3.1 Application aspects of Severe Plastic Deformation process	11
<b>1.4 Organization of thesis</b>	<b>14</b>
<b>CHAPTER 2</b>	
<b>LITERATURE REVIEW</b>	<b>15</b>
<b>2.1 Introduction</b>	<b>15</b>
<b>2.2 Al-Cu-Li alloys</b>	<b>15</b>
2.2.1 Precipitates and their effect on Al-Cu-Li alloys	16
2.2.2 Effect of aging on Al-Cu-Li alloys	19
2.2.3 Effect of pre-strain on precipitation and ageing kinetics in Al-Cu-Li alloys	20
2.2.4 Application aspects of Al-Cu-Li alloys	23
<b>2.3 Severe Plastic Deformation Techniques</b>	<b>25</b>
2.3.1 Equal Channel Angular Pressing (ECAP)	26
2.3.2 High Pressure Torsion (HPT)	28
2.3.3 Friction Stir Processing (FSP)	30
2.3.4 Limitation of the above discussed SPD techniques	31
<b>2.4 Multi-Axial Forging (MAF) – An effective solution</b>	<b>32</b>
2.4.1 Principle of MAF process	33
2.4.2 Strain imposed in MAF	36
2.4.3 Factors affecting MAF process	36

<b>2.5 Hall - Petch Relation</b>	<b>37</b>
<b>2.6 Literature Overview</b>	<b>37</b>
<b>2.7 Corrosion of Al-Cu-Li alloys</b>	<b>39</b>
<b>2.8 Wear behavior of Al-Cu-Li alloys</b>	<b>42</b>
<b>2.9 Motivation for the proposed work</b>	<b>43</b>
<b>2.10 Objectives of present work</b>	<b>45</b>
<b>CHAPTER 3</b>	
<b>EXPERIMENTAL WORK</b>	
<b>3.1 Introduction</b>	<b>47</b>
<b>3.2 Material selection and procurement</b>	<b>47</b>
<b>3.3 Multi Axial Forging (MAF)</b>	<b>48</b>
3.3.1 Die Setup	48
3.3.2 Forging Press	50
3.3.3 Heating setup	50
3.3.4 MAF Procedure	51
3.3.5 Artificial Aging Heat Treatment	52
<b>3.4 Structural characterization</b>	<b>52</b>
3.4.1 Optical microscope	53
3.4.2 Microstructural characterization by FESEM-EBSD	53
3.4.3 Transmission electron microscope (TEM)	55
3.4.4 X-Ray diffraction (XRD)	56
<b>3.5 Mechanical properties evolution</b>	<b>58</b>
3.5.1 Vicker's Micro-Hardness Characterization	59
3.5.2 Tensile testing	60
<b>3.6 Corrosion studies</b>	<b>60</b>
3.6.1 Electrochemical studies	60
<b>3.7 Wear studies</b>	<b>61</b>
<b>CHAPTER 4</b>	
<b>RESULTS AND DISCUSSION: MICROSTRUCTURE AND MECHANICAL PROPERTIES</b>	
<b>4.1 Microstructure characterization</b>	<b>63</b>
4.1.1 Optical microscopy	63

4.1.2	Electron Back Scattered Diffraction	65
4.1.2.1	Grain size distribution	69
4.1.2.2	Misorientation angle and Grain boundary character distribution (GBCD)	69
4.1.2.3	Kernel average misorientation (KAM) and grain orientation spread (GOS)	71
4.1.3	Transmission Electron microscopy	73
4.1.3.1	Effect of MAF on microstructures	73
4.1.3.2	Effect of artificial aging heat treatment on microstructures	74
4.1.4	X-Ray Diffraction	77
4.1.5	XRD Macro texture analysis	78
<b>4.2</b>	<b>Mechanical behavior of AA2050 Al-Cu-Li alloy</b>	<b>81</b>
4.2.1	Microhardness characterization	82
4.2.1.1	Effect of MAF processing on microhardness	82
4.2.1.2	Effect of artificial ageing on microhardness	84
4.2.2	Tensile behaviour of MAF processed AA2050 Al-Cu-Li alloy	87
4.2.2.1	Effect of MAF processing on tensile behaviour of AA2050 Al-Cu-Li alloy	88
4.2.2.2	Effect of artificial ageing on tensile behaviour of MAF processed AA2050 Al-Cu-Li alloy on tensile behaviour	90
4.2.3	Fracture surface analysis	92
<b>CHAPTER 5</b>		
<b>RESULTS AND DISCUSSION: CORROSION AND WEAR STUDIES</b>		<b>97</b>
<b>5.1</b>	<b>Corrosion studies</b>	<b>97</b>
5.1.1	Open circuit potential (OCP) of AA2050	97
5.1.2	Potentiodynamic polarization studies	98
5.1.3	Corrosion surface morphology	100
5.1.3.1	Intergranular corrosion (IGC)	103
<b>5.2</b>	<b>Wear analysis results</b>	<b>105</b>
5.2.1	Wear properties	105
5.2.1.1	Average coefficient of friction (COF)	105
5.2.1.2	Specific wear rate (SWR)	109

5.2.2	Wear surface topography analysis through 3D profilometer	110
5.2.3	Wear surface morphologies	111
5.2.4	Counter surface morphologies	115
5.2.5	Wear derbies characterization	116
<b>CHAPTER 6</b>		
<b>CONCLUSION</b>		<b>119</b>
<b>SCOPE FOR FUTURE WORK</b>		<b>122</b>
<b>REFERENCES</b>		<b>123</b>
<b>LIST OF PUBLICATIONS BASED ON PH.D. RESEARCH WORK</b>		<b>133</b>
<b>BIO DATA</b>		<b>135</b>

## LIST OF FIGURES

<b>Figure 1.1</b> Graphical representation of number of MAF articles published v/s time	3
<b>Figure 1.2</b> Bar graph showing number of MAF articles published by various countries/regions.	3
<b>Figure 1.3</b> Bar graph showing number of MAF articles published by top 10 authors across the world.	4
<b>Figure 1.4</b> Classification of Aluminum Alloys.	5
<b>Figure 1.5</b> 300 mm ECAP processed Al <sub>0.5</sub> Cu A) Flat target, B) Non-flat target	12
<b>Figure 1.6</b> 4000-Ton hydraulic press with ECAP die assembly	13
<b>Figure 1.7</b> Biomedical implants fabricated from ultrafine-grained Titanium: a) device for correction and fixation of spinal column, b) plate for bone fixation and c) conic screw for spine fixation.	13
<b>Figure 2.1</b> Schematic representation of microstructure in Al-Cu-Li alloys.	17
<b>Figure 2.2</b> Schematic representation of distribution of precipitates after (a) T6 aging treatment and (b) T6I6 aging treatment on 2195 alloy.	19
<b>Figure 2.3</b> Schematic representation of precipitate evolution pre-rolled and pre-rolled AA2195 Al-Cu-Li alloy samples.	21
<b>Figure 2.4</b> HAADF-STEM images captured in $\langle 110 \rangle_{\alpha}$ zone axis of the specimens, representing both peak-aged and over-aged conditions.	22
<b>Figure 2.6</b> Schematic representation of ECAP process.	27
<b>Figure 2.7</b> High Pressure Torsion.	29
<b>Figure 2.8</b> Friction Stir Processing technique.	30
<b>Figure 2.9</b> Sectional representation of MAF setup.	35
<b>Figure 2.10</b> Process sequence of Multi Axial Forging.	35
<b>Figure 2.11</b> Corrosion surface morphology of al-cu-li alloy observed during aging for (a,b) 26 h, (c,d) 104 h, (e,f) 159 h and (g,h) 242 h, and (i) represents the respective potentiodynamic polarization curves.	41
<b>Figure 3.1</b> MAF die setup in (a) the assembled and (b) the exploded view, (c) assembled die setup on utm bed.	49
<b>Figure 3.2</b> 100-Ton UTM with MAF die and heating setup.	50
<b>Figure 3.3</b> Machined prismatic sample a) before MAF processing, b) after MAF processing.	51

<b>Figure 3.4</b> FESEM setup with EDAX and EBSD attachment.	<b>54</b>
<b>Figure 3.5</b> Schematic representation of FESEM EBSD setup.	<b>55</b>
<b>Figure 3.6</b> JEOL JEM-2100 Transmission electron microscope.	<b>56</b>
<b>Figure 3.7</b> (a) Panalytical EMPYREAN diffractometer, (b) sample holder with source, detector and goniometer configuration, and (c, d) schematic representation of X-ray diffraction.	<b>58</b>
<b>Figure 3.8</b> (a) Vickers microhardness tester, and (b) indentation on the sample surface.	<b>59</b>
<b>Figure 3.10</b> (a) Magnified portion of electrochemical setup depicting the three-electrode configuration, and (b) electrochemical workstation.	<b>61</b>
<b>Figure 3.11</b> (a) Schematic representation of ball-on-disc reciprocating setup, (b) ANTON PAAR TRB <sup>3</sup> ball-on-disc reciprocating setup, and (c) magnified portion depicting sample and the counter ball interface.	<b>62</b>
<b>Figure 4.1</b> Optical micrographs of AA2050 Al-Cu-Li alloy in different processed conditions of (a) SHT, and (b) 3 pass, (c) 6 pass, (d) 9 pass, (e) 12 pass MAF processed conditions.	<b>64</b>
<b>Figure 4.2</b> Optical micrographs of AA2050 Al-Cu-Li alloy in (a) SHT + peak aged, (b) 6 pass + peak aged, and (c) 12 pass + peak aged sample conditions.	<b>65</b>
<b>Figure 4.3</b> Image quality and IPF maps of AA2050 alloy in SHT sample condition.	<b>66</b>
<b>Figure 4.4</b> Image quality and IPF maps of AA2050 alloy after 6 pass MAF processed condition.	<b>67</b>
<b>Figure 4.5</b> Image quality and IPF maps of AA2050 alloy after 12 pass MAF processed condition.	<b>67</b>
<b>Figure 4.6</b> Image quality and IPF maps of AA2050 alloy after 6 pass MAF processed and peak aged condition.	<b>68</b>
<b>Figure 4.7</b> Image quality and IPF maps of AA2050 alloy after 12 pass MAF processed and peak aged condition.	<b>68</b>
<b>Figure 4.8</b> (a-e) Grain size distribution plots for SHT, 6 and 12 pass MAF processed, and peak aged samples of SHT, 6 and 12 pass MAF processed, (f) variation of grain size distribution in various processed conditions.	<b>70</b>

<b>Figure 4.9</b> (a) Grain boundary character distribution, and misorientation angle distribution for (b) SHT, (c) 6 pass, (d) 12 pass, (e) 6 pass + peak aged, (f) 12 pass + peak aged sample conditions.	<b>71</b>
<b>Figure 4.10</b> EBSD generated (a) Kernel Average Misorientation (KAM) and (b) Grain Orientation Spread (GOS) for various processed conditions.	<b>73</b>
<b>Figure. 4.11</b> TEM micrographs of AA2050 alloy in different processed conditions: bright field image and SAED pattern of (a,d) SHT sample, (b,e) 6 pass MAF processed sample, and (c,f) 12 pass MAF processed sample.	<b>74</b>
<b>Figure 4.12</b> Schematic SAED pattern representation of spots and streaks corresponding to various precipitates observed in Al-Cu-Li alloys.	<b>76</b>
<b>Figure 4.13</b> TEM micrographs of AA2050 alloy in different processed conditions: bright field image and saed pattern of (a,d) sht sample, (b,e) 6 pass MAF processed sample, and (c,f) 12 pass MAF processed sample.	<b>76</b>
<b>Figure 4.14</b> (a) X-ray diffraction patterns, (b) analysis of X-ray diffraction peaks corresponding to (111) lattice plane of AA2050 Al-Cu-Li alloy for various processed condition.	<b>78</b>
<b>Figure 4.15</b> Schematic representation of typical orientation and ideal texture components of a FCC material in {111} and {200} pole figures.	<b>80</b>
<b>Figure 4.16</b> {111}, {200} and {220} pole figures of AA2050 alloy in different processed conditions: (a) SHT, (b) 6 pass, and (c) 12 pass MAF processed.	<b>80</b>
<b>Figure 4.17</b> {111}, {200} and {220} pole figures of the AA2050 alloy in different processed conditions: (a) SHT + PA, (b) 6 pass + PA, and (c) 12 pass + PA.	<b>81</b>
<b>Figure 4.18</b> Variation of Vickers microhardness of AA2050 Al-Cu-Li alloy subjected to MAF process.	<b>84</b>
<b>Figure 4.20</b> Variation of Vickers microhardness of AA2050 alloy artificially aged at 155°C under different processed conditions.	<b>86</b>
<b>Figure 4.21</b> Variation of Vickers microhardness of AA2050 alloy artificially aged at 175°C under different processed conditions.	<b>87</b>
<b>Figure 4.22</b> Engineering stress-strain curves of AA2050 alloy subjected to MAF process.	<b>89</b>
<b>Figure 4.23</b> Mechanical properties of MAF processed AA2050 Al-Cu-Li alloy.	<b>89</b>

<b>Figure 4.24</b> (a) Engineering Stress-Strain Curves of MAF processed AA2050 Al-Cu-Li alloy at peak aged condition.	<b>91</b>
<b>Figure 4.25</b> Mechanical properties of AA2050 Al-Cu-Li alloy of SHT and MAF processed samples after peak aging.	<b>91</b>
<b>Figure 4.26</b> SEM observations for the fractured surfaces of the tensile samples, respectively in (a) SHT, (b) 3 pass, (c) 6 pass, (d) 9 pass, and (e) 12 pass MAF processed condition.	<b>94</b>
<b>Figure 4.27</b> SEM observations for the fractured surfaces of the tensile samples, respectively in (a,b) SHT + PA, (c,d) SHT + 6 pass + PA, (e,f) 12 pass + PA MAF processed condition.	<b>95</b>
<b>Figure 5.2</b> Polarization curves of AA2050 alloy in different processed conditions prior to artificial aging in 3.5 wt% NaCl solution.	<b>99</b>
<b>Figure 5.3</b> Polarization curves of AA2050 alloy in different processed conditions after peak ageing in 3.5 wt% NaCl solution.	<b>100</b>
<b>Figure 5.4</b> SEM corrosion surface morphologies of AA2050 Al-Cu-Li alloy in different processed conditions: (a,b) solution heat treated, (c,d) 6th pass MAF processed, and (e,f) 12th pass MAF processed.	<b>101</b>
<b>Figure 5.5</b> SEM corrosion surface morphologies of AA2050 Al-Cu-Li alloy in different processed conditions: (a,b) SHT + peak aged, (c,d) 6th pass + peak aged, and (e,f) 12th pass + peak aged.	<b>102</b>
<b>Figure 5.6</b> Corrosion surface micrographs of the AA2050 in the L-LT plane for (a)SHT, (b) 6 pass, (c) 12 pass, (d) SHT + peak aged, (e) 6 pass + peak aged, and (f) 12 pass + peak aged samples after 10 hours of immersion.	<b>104</b>
<b>Figure 5.7</b> No. of cycles v/s coefficient of friction (COF) at different normal load conditions in SHTsample condition.	<b>106</b>
<b>Figure 5.8</b> No. of cycles v/s coefficient of friction (COF) at different normal load conditions in 6 pass MAF processed sample condition.	<b>106</b>
<b>Figure 5.9</b> No. of cycles v/s coefficient of friction (COF) at different normal load conditions in 12 pass MAF processed sample condition.	<b>107</b>
<b>Figure 5.10</b> No. of cycles v/s coefficient of friction (COF) at different normal load conditions in SHT+peak aged sample condition.	<b>107</b>

<b>figure 5.11</b> No. of cycles v/s coefficient of friction (COF) at different normal load conditions in 6 pass + peak aged sample condition.	<b>108</b>
<b>Figure 5.12</b> No. of cycles v/s coefficient of friction (COF) at different normal load conditions in 12 pass + peak aged sample condition.	<b>108</b>
<b>Figure 5.13</b> Variation of average coefficient of friction (COF) under different normal loads of AA2050 subjecting to (a) MAF process, (b) after aging.	<b>109</b>
<b>Figure 5.14</b> Shows the change in SWR, plotted for various sample conditions after subjecting to artificial aging.	<b>110</b>
<b>Figure 5.14</b> Variation of specific wear rate with various samples conditions for AA2050 al alloy subjecting to (a) MAF process, (b) after aging.	<b>110</b>
<b>Figure 5.15</b> Axonometric projections of wear surface obtained using 3d profilometer in various processing and sample conditions.	<b>111</b>
<b>Figure 5.16</b> FESEM micrograph of AA2050 alloy wear track of SHT sample in (a) 2N, (b) 10N; 6 pass sample in (c) 2N, (d) 10N; and 12 pass sample in (e) 2N, (f) 10N loading conditions.	<b>113</b>
<b>Figure 5.17</b> FESEM micrograph of AA2050 alloy wear track of SHT + PA sample in (a) 2N, (b) 10N; 6 pass + PA sample in (c) 2N, (d) 10N; and 12 pass + PA sample in (e) 2N, (f) 10N loading conditions.	<b>114</b>
<b>Figure 5.18</b> EDS maps measured at the various spots marked in figure 5.16 and figure 5.17.	<b>115</b>
<b>Figure 5.19</b> SEM micrographs of counter steel ball surface under 10 N load for (a) SHT sample, (b) SHT + aged sample and EDS spectrum for regions marked as (c) EDS 1 and (d) EDS 2.	<b>116</b>
<b>Figure 5.20</b> SEM micrographs of counter steel ball surface under 10 N load for (a) 6 pass, (b) 6 pass + peak aged, (c) 12 pass, (d) 12 pass + peak aged sample and EDS spectrum for regions marked as (e) EDS 1, (f) EDS 2, (g) EDS 3 and (h) EDS 4.	<b>117</b>
<b>Figure 5.21</b> SEM micrographs of wear debris obtained during the reciprocating wear tests carried at load of 10N for (a) SHT, (b) 12 pass, (c) SHT + peak aged, and (d) 12 pass + peak aged sample conditions, (e-h) EDS plots of various spots.	<b>118</b>

## ABBREVIATIONS

Al	Aluminium
Cu	Copper
Li	Lithium
Mg	Magnesium
MDF	Multi Directional Forging
MAF	Multi Axial Forging
EBSD	Electron Back Scattered Diffraction
TEM	Transmission Electron Microscopy
SPD	Severe Plastic Deformation
IPF	Inverse Pole Figure
KAM	Kernal Average Misorientation
GOS	Grain Orientation Spread
OIM	Orientation Image Micrographs
CG	Coarse Grain
GB	Grain Boundary
ECAP	Equal Channel Angular Pressing
HPT	High Pressure Torsion
ARB	Accumulative Roll Bonding
UFG	Ultra Fine Grain
LAGB	Low Angle Grain Boundary
HAGB	High Angle Grain Boundary
FCC	Face Centered Cubic
AA	Aluminium Association
GP	Guinier Preston

OM	Optical Microscopy
SEM	Scanning Electron Microscopy
FESEM	Field Emission Scanning Electron Microscopy
SAED	Selected Area Electron Diffraction
XRD	X Ray Diffraction
PFZ	Precipitate Free Zone
RT	Room Temperature
CF	Cryo Forging
ASTM	American Society for Testing Materials
SHT	Solution Heat Treated
UTM	Universal Testing Machine
WR	Wear Rate
SWR	Specific Wear Rate
COF	Coefficient Of Friction
PA	Peak Aged
YS	Yield Strength
UTM	Universal Testing Machine
UTS	Ultimate Tensile Strength
CR	Corrosion Rate
SLC	Severe Localized Corrosion
PID	Proportional Integral Derivative



# CHAPTER 1

## INTRODUCTION

In recent years, advancements in the performance of aircrafts and spacecrafts have relied heavily on the continuous enhancement of materials utilized in their construction. Materials engineers have focused on two fundamental approaches to improve overall alloy performance and achieve optimal material utilization, thereby enhancing low cost-weight ratio. For over eight decades, aluminium alloys have played crucial role as primary materials in structural components of aircraft and aerospace applications. This enduring preference can be attributed to their remarkable characteristics, including lightweight properties, high strength, exceptional damage tolerance, and resistance to corrosion.

Microstructure of materials significantly influence the mechanical properties. To meet the demands of cost-effectiveness and specific property balances, researchers have shown considerable interest in modifying the microstructure of these materials through grain refining processes and grain structure control, in addition to alloy optimization. Generally, two distinct approaches are employed to produce bulk metallic materials with fine or ultra-fine grain structures. The first approach, known as the bottom-up approach, involves the compaction or binding of ultrafine powders or nanoparticles, which act as the building blocks, to form structures with ultra-fine grain sizes. Secondly, the top-down approach which involves reducing the grain size through thermo-mechanical processing techniques (Kecskes et al. 2007).

### 1.1 Background

Human civilization has progressed from relying on natural materials like wood and stone to the synthesis and optimization of diverse metal alloys and composites. Metal working, specifically metal forming, stands as one of the oldest practices employed to fabricate a wide array of metal components that were used for daily household activities. Historical records provide evidence of the extensive use of hammering or forging techniques to shape metals such as gold and copper as early as 8000 B.C. However, in ancient times, the amount of plastic strain that

could be induced through classical metal forming techniques was limited due to the risk of material or tool failure.

In the scientific era, significant advancements in material characterization techniques emerged with the discovery of different types of microscopes. This breakthrough opened up new avenues for research in fields of grain refinement and microstructural modifications. During World War II, as steel and aluminium industries expanded, there was a surge in research, focused on these areas. With the ability to observe microstructures and gain insights into material failure concepts, novel metal forming processes capable of inducing large plastic strain, were developed. These developments marked a pivotal moment in the evolution of material science and metalworking techniques.

Severe plastic deformation, initially referred to as intense plastic straining, emerged with the development of high-pressure torsion (HPT) setup by Bridgman (1952). Over the past three decades, there has been significant interest in exploring various SPD techniques for producing bulk ultrafine-grained materials. Among these techniques, multi axial forging has gained considerable attention due to its simplicity and effectiveness. According to the widely accepted Scopus scientific database, there are currently over 390 publications on MAF contributed by more than 400 researchers from 32 nations worldwide. Figure 1.1 displays annual contributions worldwide extracted from Scopus scientific database, showing an increasing number of publications since the first article on MAF was published in 2002 (Noda et al. 2002). Figure 1.1 also reveals a significant surge in the number of publications in the past five years (2018-2023), highlighting the ongoing exploration and development of the process. Figure 1.2 illustrates the contribution made by different countries towards the development of the MAF process. China leads with over 152 publications, followed by Japan and India, as of today. This indicates the growing research interest among various researchers across the world in the development of MAF process. Further, Figure 1.3 represents the contribution of individual researchers who have each published more than ten articles on MAF.

The ongoing exploration and development of SPD techniques are paying way for their practical applications and commercial productions, transiting from

laboratory-scale research. However, several challenges must be overcome to fully realize their potential. One important aspect is the development of more feasible and economical production procedures. Cost-effective scaling-up of SPD processes is essential for their widespread implementation in industries. SPD techniques often impose limitations on the shape complexity of the processed materials, which can be a hindrance for certain applications. Finding innovative scientific solutions to overcome these shape constraints are key challenging areas of focus for researchers working in the field of SPD. By addressing these challenges, SPD techniques can be further optimized and harnessed for a wider range of practical applications.

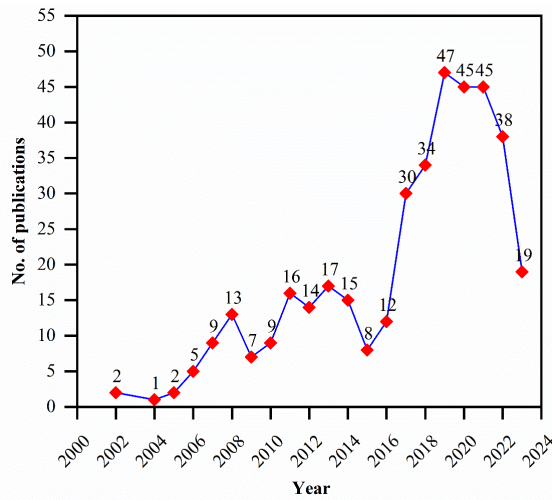


Figure 1.1 Graphical representation of number of MAF articles published v/s time

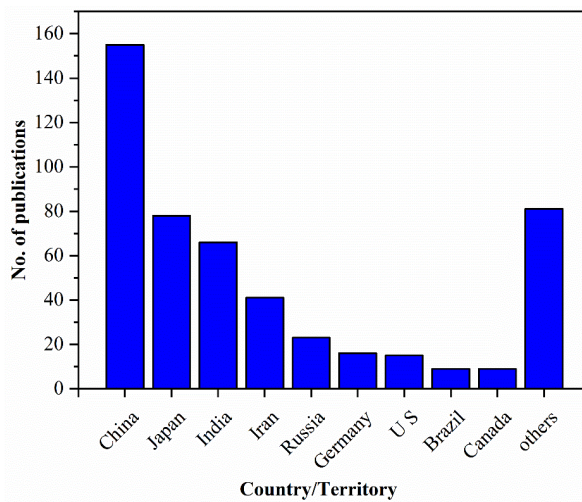


Figure 1.2 Bar graph showing number of MAF articles published by various countries/regions.

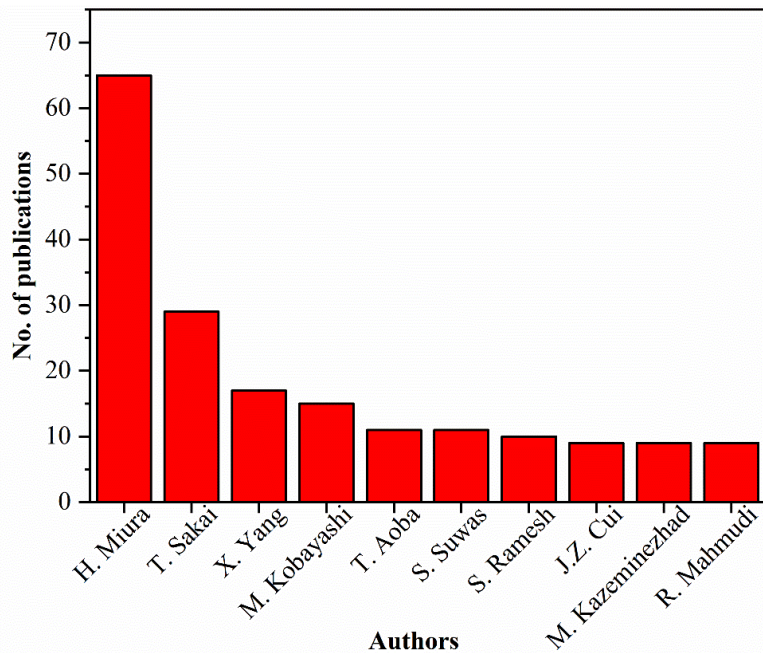


Figure 1.3 Bar graph showing number of MAF articles published by top 10 authors across the world.

## 1.2 Aluminium Alloys

Pure aluminium (Al) also spelled Aluminium, and its alloys have played a pivotal role in the progress of humanity. Aluminium is the 3<sup>rd</sup> most abundant element available in the Earth's crust next to oxygen and silicon and was named by the English chemist Sir Humphry Davy in 1808. Aluminium and its alloys are highly valued for their combination of advantageous properties, making them extensively utilized in various industries. Their relatively low cost, non-ferrous nature, exceptional strength, good corrosion resistance, as well as excellent machinability and weldability, have made them indispensable in aerospace, aircraft, automotive, and structural applications (ASM Handbook 1993).

Aluminium, with an atomic number of 13, is a ductile, soft, and silvery-white non-ferrous metal belonging to group 13 (Boron group) in the periodic table. It possesses a remarkable lightweight characteristic, with an alloy density of 2.7 g/cm<sup>3</sup>. Aluminium alloys possess face-centred cubic (FCC) crystal structure and have a lattice parameter of  $a = 4.046 \text{ \AA}$ . This crystal structure remains stable until its melting point at 657°C. The FCC structure of aluminium alloys is characterized by multiple slip planes, which greatly contribute to their excellent formability.

This property allows for the efficient shaping and processing of aluminium alloys in various manufacturing applications.

Aluminium industries are driven by the primary goal of developing high-strength and lightweight alloys that do not compromise system performance in aerospace and aircraft applications. Aluminium alloys are recognized as the second lightest class of non-ferrous alloys, following magnesium alloys. Thanks to its low density, aluminium is well-suited for various applications, where weight reduction is critical. Additionally, aluminium possesses excellent thermal conductivity, measuring around 250 W/m/K at room temperature. Its high thermal coefficient of expansion further contributes to its versatility. Moreover, aluminium alloys exhibit an impressive strength-to-weight ratio, approximately twice than that of steel. These advantageous properties have led to wide range of applications for aluminium, from everyday kitchen utilities to the construction of aircraft structures.

### 1.2.1 Classification of Aluminum alloys

A broader classification of Aluminium alloys are of two main types, namely wrought alloys and cast alloys, depending on their intended use. Wrought aluminium alloys find extensive applications, ranging from airplane wings to kitchen foils. In contrast, cast aluminium alloys form a substantial category of materials, ranking second only to ferrous casting in terms of tonnage.

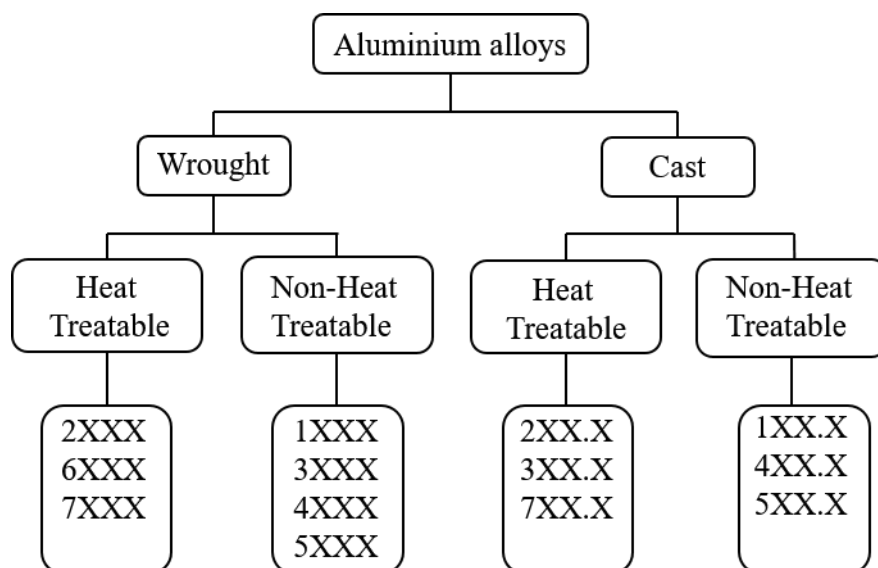


Figure 1.4 Classification of aluminum alloys.

Furthermore, aluminium alloys can be further classified based on their strengthening mechanism. Alloys that can be heat treated to enhance their properties are referred as heat-treatable alloys. Conversely, the remaining alloys are classified as non-heat-treatable alloys. Figure 1.4 provides an overview of the overall classification, with each alloy system designated according to the standard form defined by the Aluminium Association (AA). This classification system serves as a standardized reference for identifying and categorizing different aluminium alloy compositions and properties.

### **1.2.2 Basic concepts of strengthening Aluminum alloys**

In annealed condition, high-purity aluminium possesses relatively low strength, typically measuring around 30 MPa. However, the mechanical properties of pure metals can be enhanced by introducing alloying elements, which impede or act as barriers to mobility of dislocations in the material. Thus, the addition of solute atoms to the aluminium matrix can enhance its strength. This method was initially employed in conventional aluminium alloys to increase their overall strength.

Around a century ago, finding of age-hardening effect in Al alloys introduced an effective strategy for enhancing the strength of heat-treatable (age-hardenable) aluminium alloys through a process known as precipitation hardening. Subsequent research on aluminium alloys revealed that, deforming the material at lower temperatures also contributed to increased strength, due to the strain hardening effect. Additionally, it was observed that microstructures of deformed samples after annealing resulted in the formation of fine-grained microstructures, leading to further strength improvement. Consequently, two additional concepts emerged to enhance the strength properties of aluminium alloys: dislocation strengthening and grain size strengthening.

In general, most aluminium alloys employ one or more of the following four concepts to enhance their resistance to plastic deformation: cold working (strain hardening), grain refinement, solid solution strengthening (alloying), and precipitation hardening (age hardening). These approaches contribute to improving the overall strength properties of aluminium alloys.

### 1.2.3 Introduction to Al-Cu-Li alloys

Aluminum alloys containing lithium (Li) and copper (Cu) as their primary alloying components hold significant significance within the aerospace sector because of their lightweight characteristics and exceptional properties. Al-Cu-Li alloys are heat-treatable, precipitation-hardened wrought alloys that fulfill the requirements of aerospace industry. They have emerged as highly promising materials for latest generations of commercial aircraft, receiving extensive development efforts over several decades.

These alloys offer significant opportunities for enhancing aero-structural performance by reducing density, increasing stiffness, improving fracture toughness, enhancing resistance to fatigue crack growth, and providing superior corrosion resistance. Extensive research in recent years is focused on alloy development, studying precipitation and hardening processes, and exploring further processing techniques to optimize properties of Al-Cu-Li alloys.

Continuous advancement in understanding and refinement of Al-Cu-Li alloys has positioned the alloys as key material for meeting the demanding requirements of aerospace industry. Unique combination of lightweight characteristics and enhanced properties makes them highly desirable for various aerospace applications. Table 1.1 shows the elemental composition and reported density of important Al-Li alloys, developed over the time. Development of Li based aluminium alloys has occurred in three stages or generations as discussed below.

**First Generation Alloys:** These alloys feature magnesium as the second alloying element along with lithium. They were developed early in the process of lithium-based alloy development.

**Second Generation Alloys:** Aluminium alloys containing higher amounts of copper and lithium (with a lithium content exceeding 2 wt%) are considered. These alloys exhibited enhanced properties when compared to their preceding generation alloys.

**Third Generation Alloys:** The development of the third generation of aluminum alloys based on lithium aimed to address the issue of anisotropy associated with increased lithium content. In these alloys, amount of lithium is restricted to below 2 wt% to mitigate the anisotropy concern, without variations in desirable properties.

By refining the alloy compositions and optimizing the lithium content, researchers have made significant progress in improving the performance and characteristics of lithium-based aluminium alloys. Each generation alloys have brought about advancements and addressed specific challenges to enhance the overall properties and usability of these alloys.

Table 1.1 Standard composition of key Al-Cu-Li alloys.

Alloys	Li	Cu	Mg	Ag	Zr	Sc	Mn	Zn	Density $\rho$ (g/cm <sup>3</sup> )	Introduction
<b>First Generation</b>										
2020	1.2	4.5					0.5		2.71	Alcoa 1958
1420	2.1		5.2		0.1				2.47	Soviet 1965
1421	2.1		5.2		0.1	0.2			2.47	Soviet 1965
<b>Second Generation (Li <math>\geq</math> 2wt%)</b>										
2090	2.1	2.7			0.1				2.59	Alcoa 1984
2091	2	2	1.3		0.1				2.58	Pechiney 1985
8090	2.4	1.2	0.8		0.1				2.54	EAA 1984
<b>Third Generation (Li <math>\leq</math> 2wt%)</b>										
2195	1	4	0.4	0.4	0.1				2.71	LM/Reynolds 1992
2196	1.8	2.9	0.5	0.4	0.1		0.35 max	0.35 max	2.63	LM/Reynolds/ McCook Metals 2000
2198	1	3.2	0.5	0.4	0.1		0.5 max	0.35 max	2.69	Reynolds/ McCook Metals/Alcan 2005
2098	1.1	3.5	0.5	0.4	0.1		0.35 max	0.35	2.7	McCook Metals 2000
2099	1.8	2.7	0.3		0.1		0.3	0.7	2.63	Alcoa 2003
2050	1	3.6	0.4	0.4	0.1		0.35	0.25 max	2.7	Pechiney/ Alcan 2004
2055	1.2	3.7	0.4	0.4	0.1		0.3	0.5	2.7	Alcoa 2011
2060	0.8	4	0.9	0.3	0.1		0.3	0.4	2.72	Alcoa 2011
2065	1.2	4.2	0.5	0.3	0.1		0.4	0.2	2.7	Constellium 2012

### **1.3 Severe Plastic Deformation**

Severe plastic deformation has gained considerable research interest in the past two decades and is being considered as an effective technique for producing Ultra-Fine grains (UFG) by imposing large plastic strains in the bulk materials. UFG materials thus formed (via SPD process) exhibits superior material properties. Among the many well explored SPD processes, Multi axial forging also called as Multi-Directional Forging (MDF), has been greatly adopted for processing materials at room temperature or even at cryogenic temperatures.

SPD processes led to the accumulation of strain energy and formation of non-equilibrium grain boundaries in the alloy. These effects result in reduced thermal stability of the material. This reduced thermal stability, during post processing or heat treatment, due to combined effect of stored strain and temperatures could complicate the microstructure evolution. Thus, the combined effect of SPD and thermal processing could be an effective route to modify microstructure that alters the material properties. Understanding this modified microstructural evolution is of greater importance in enhancing the material's performance from scientific point of view and is an interesting issue.

The term severe plastic deformation was originally defined as intense plastic straining under the influence of high pressure. The relevance of SPD process is to produce ultrafine/fine grains in bulk materials, while retaining the shape and dimensions of the original material (Bagherpour et al. 2018; Furukawa et al. 1998). Reduction in grain size further leads to enhancement in material properties such as strengths and hardness. At present, SPD covers all metal forming processes which are capable of imposing large plastic strains that are based on simple shear and/or plane strain and tend to retain the initial shape of the billet. To produce metals with improved material properties, utilization of various SPD techniques in metal processing has a long history and dates to ancient times. However, the process in ancient times was only guided by the experience of craftsman without any knowledge of the material structure and their influence on material properties. Later in the 19<sup>th</sup> century upon the development of compound lens and microscope, Metallurgists were able to observe grain structures and correlate them with physical, structural, and material properties of metals. This led to

the systematic characterization and development of new alloys and exploration of fine-scale structures in polycrystalline materials.

### **1.3.1 Application aspects of severe plastic deformation process**

Despite certain limitations such as larger investments, limitation of materials and wastages, on commercialization of SPD techniques, there are number of instances, on successful adoption of the process for practical applications. The research community has focused a lot on development of new SPD techniques, optimizing processing parameters for maximum output efficiencies which have resulted in the use of SPD processed materials in wide practical applications. In this section, a few such instances are reported.

In 1997, Honeywell Electronic Materials, USA, succeeded in scaling up Equal Channel Angular Extrusion (ECAE) by developing a large die setup. This setup involved the use of presses with capacities of 1000 and 4000 tons, as depicted in Figure 1.6. However, the first commercial utilization of bulk fine-Grained (FG) metals processed through SPD dates to 2003. Honeywell International, Inc. began manufacturing monolithic sputtering targets made of aluminum and copper for physical vapor deposition coatings during that period (Figure 1.5) (Ferrasse et al. 2008). SPD processed sputtering targets exhibited better sputter performance and higher lifetimes compared to conventional counterparts. Figure 1.5(a) is the Al-0.5Cu monolithic flat type sputter target produced through ECAP with overall dimensions of 525 mm diameter x 25 mm thickness. The operational lifetime increments of 52% have been achieved in comparison with conventional counterparts. Figure 1.5(b) shows the Cu 6%Cr non-flat monolithic ECAP processed 300 mm diameter target weighing around 32.5 kilograms produced by Praxair Electronics, France resulted in 65-70% reduction in ownership cost. Additionally, studies have demonstrated that downsizing ECAP process presents possibilities for manufacturing ultrafine grain structured wires, fibers, and microgears (Kim et al. 2002). Downscaling of ECAP process has also been explored for processing of materials intended to produce components for micro electro-mechanical systems (MEMS).

Lack of mechanical and fatigue strength limited the use of biocompatible pure Ti in load bearing orthopedic implants. The works carried out by (Sergueeva et al. 2001)

reported that titanium processed by SPD exhibited excellent biocompatibility with enhanced strengths. Later, Mishnaevsky et al. (2014) and Valiev et al. (2012) were successful in fabricating nanostructured titanium for dental and orthopedic implants. Figure 1.7(a) depicts a 2 mm diameter UFG dental implant developed within the framework of VINAT, funded by the European Commission and the Ministry of Education and Science of the Russian Federation. Similar example is the application of UFG Ti alloy in biomedical applications in trauma cases, plates, and screws shown in Figure 1.7(c), which are widely used for bone fixation.

Figure 1.7(c), shows another biomedical application of SPD processed UFG Ti alloy in trauma cases. These plates and screws are used in bone fixation and the enhanced compressive and bending strength with adequate ductility is an additional advantage. Similar to a special conic screw as shown in Figure 1.7(d), parts shown in Figure 1.7(b) are used for the correction and fixation of spinal column, which possess high static and fatigue strength. These parts are produced from UFG Ti by ECAP. In recent years, SPD has gained considerable importance in processing materials for applications in extreme conditions like cryogenic applications, arctic and subarctic environments or in the oil, gas, and energy sectors.

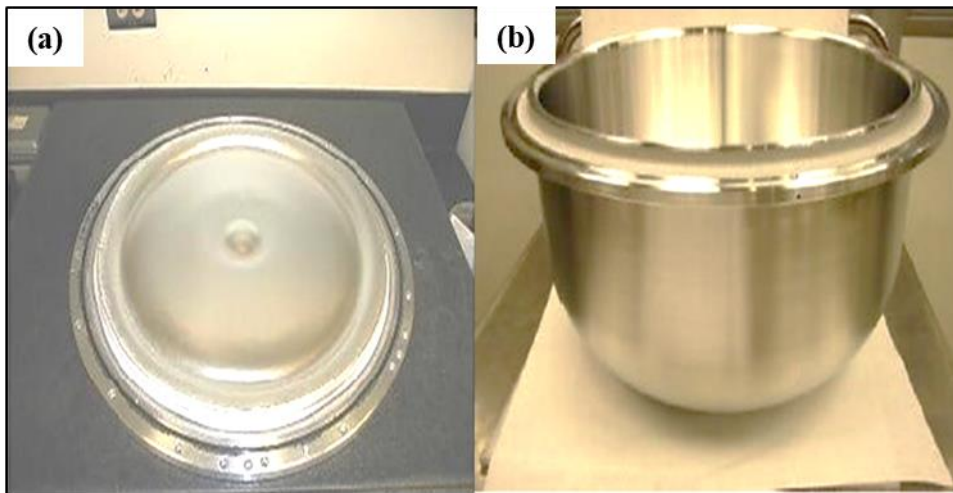


Figure 1.5 300 mm ECAP processed  $Al_{0.5}Cu$  a) flat target, b) non-flat target (Valiev et al. 2007).



Figure 1.6 4000-ton hydraulic press with ECAP die assembly (Ferrasse et al. 2008).

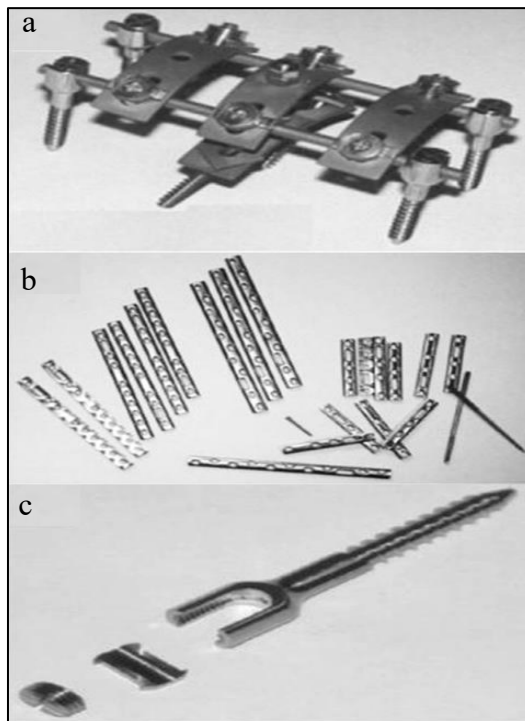


Figure 1.7 Biomedical implants fabricated from ultrafine-grained titanium: a) device for correction and fixation of spinal column, b) plate for bone fixation and c) conic screw for spine fixation (Elias et al. 2013).

## 1.4 Organization of thesis

**Chapter 1** presents the brief introduction to the thesis. Starting from background to SPD process, present research status in the research community has been addressed. Further, Al alloys and their classification, and the various methods of strengthening Al alloys, Al-Cu-Li alloys and their classification are introduced. Introduction to SPD process and its application aspects are highlighted in the later sections.

In **Chapter 2**, a thorough literature review is provided, with a specific focus on Al-Cu-Li alloys and various SPD techniques, specifically multi-axial forging process. The review encompasses key concepts, microstructures, mechanical behavior, corrosion studies, and wear characterizations of Al-Cu-Li alloys. Furthermore, a concise, yet critical evaluation of existing literature regarding the impact of thermo-mechanical processing of Al-Cu-Li alloys on the microstructure, texture properties, mechanical properties, corrosion resistance, and wear resistance are discussed. The literature review not only showcases the promising mechanical properties displayed by Al-Cu-Li alloys but also underscores the existing gap in knowledge regarding the impact of thermo-mechanical processing on the microstructural evolution, texture, and mechanical properties of these alloys. These aspects serve as a primary motivation for current research endeavour.

**Chapter 3** provides a comprehensive presentation of the experimental aspects of the research. This chapter incorporates the alloy preparation, design of thermo-mechanical processing treatments, and utilization of various characterization techniques.

In **Chapter 4**, results and a discussion pertaining to microstructural characterization and mechanical properties of MAF and artificial aging post-MAF in AA2050 Al-Cu-Li alloy are discussed.

In **Chapter 5**, the results and discussions regarding the corrosion behavior and wear properties of the AA2050 Al-Cu-Li alloy following MAF processing and subsequent artificial aging treatments are discussed.

Finally, in **Chapter 6**, based on the findings and the available literature, the key conclusions of the present research are summarized and future scopes in the current area are provided.

## CHAPTER 2

### LITERATURE REVIEW

#### 2.1 Introduction

This chapter provides a thorough review of the literature that explores the relevance of severe plastic deformation techniques and Al-Cu-Li alloys. Specifically, it delves into the existing literature pertaining to the effect of multi-axial forging process and post-MAF aging on the microstructural evolution, mechanical properties, corrosion studies, and wear resistance of Al-Cu-Li alloys. Literature review also aims to shed light on the precipitation behaviour observed in Al-Cu-Li alloys, including the factors that influence the evolution of precipitates and the kinetics of precipitation. Understanding these precipitation phenomena is crucial for comprehending the overall microstructural evolution and its subsequent impact on mechanical properties of the alloys.

This chapter not only emphasises the current knowledge on the effects of SPD and MAF processes on Al-Cu-Li alloys, but also highlights the gaps in understanding and identifying the areas that warrant further investigation. Specifically, the review underscores the necessity for a comprehensive understanding of how thermo-mechanical processing affects the microstructure, texture, and mechanical properties of Al-Cu-Li alloys. Insights gained from this literature review will lay the foundation for the subsequent chapters of this thesis, which aim to achieve the objectives of the presented work.

#### 2.2 Al-Cu-Li alloys

Aluminium exhibits a maximum solubility of upto 14 wt% of Lithium at a temperature of 600 °C. The primary effect of introducing Lithium into Aluminium is the reduction in density of Al-based alloys. For every 1 wt% addition of Li, the density of the Al-based alloy decreases by 3%. Additionally, Young's modulus increases by 6% (Ahmed and Wu 2014; Zhang et al. 2018). Al-Li based alloys are the lightest among all other Al-based alloys. To further enhance the mechanical properties of Al alloys, Copper (Cu) is often combined with Lithium to form the  $T_1$  ( $Al_2CuLi$ ) secondary phase. Addition of Cu contributes to the overall mechanical strength of the alloy. This results in Al-Cu-Li alloys having superior

specific mechanical properties and lower density compared to alloys from the 2XXX and 7XXX series. However, the presence of a high Li content (>2 wt.%) in aluminum alloys has been found to cause anisotropy issues (Eswara Prasad et al. 2013). Anisotropy in Al-Cu-Li alloys can be attributed to various factors, including crystallographic texture, grain morphology and size, as well as precipitates that form during the aging process. These alloys are also known to exhibit reduced toughness and inadequate corrosion resistance. To address these limitations, recent studies have focused on optimizing the composition. For instance, advanced 2199 Al-Cu-Li alloy exhibits a fracture toughness that is 20 MPa higher than earlier 8090 Al-Li alloy. This improvement is achieved through optimization of alloy composition, selection of suitable thermal-mechanical processing routes, and precise control over the precipitates formation. However, the trade-off for these enhancements is the reduction in strength.

### **2.2.1 Precipitates and their effect on Al-Cu-Li alloys**

Addition of lithium (Li) into alloy matrix facilitates the formation of various strengthening precipitates, thereby enhancing material properties. While lithium exhibits highest solubility in aluminum (Al), it has been observed that, exceeding a certain limit of Li addition can lead to reduction in strength, despite its contribution to reduced density. Precipitates or dispersoids are terms used to refer to secondary phase particles that develop in aluminum alloys during the homogenization or aging process.

The major precipitates, reported in various Al-Cu-Li alloys in the literature are  $\delta'(Al_3Li)$ ,  $T_1(Al_2CuLi)$ ,  $\theta'(Al_2Cu)$ ,  $\beta(Al_3CuZr)$  and  $Al_3(Sc,Zr)$  (Chen et al. 1998; Dorin et al. 2014; Noble and Bray 1998; Noble and Thompson 2010; Williams and Edington 2010). Figure 2.1 represent the schematic visualization of various precipitates and their occurrence in microstructure on wide range of Al-Cu-Li alloys. However, for high strength third generation Al-Cu-Li alloys such as AA2050, AA2090 and AA2099,  $T_1(Al_2CuLi)$  is the major strengthening phase and is widely distributed throughout the alloy (Yan et al. 2018).

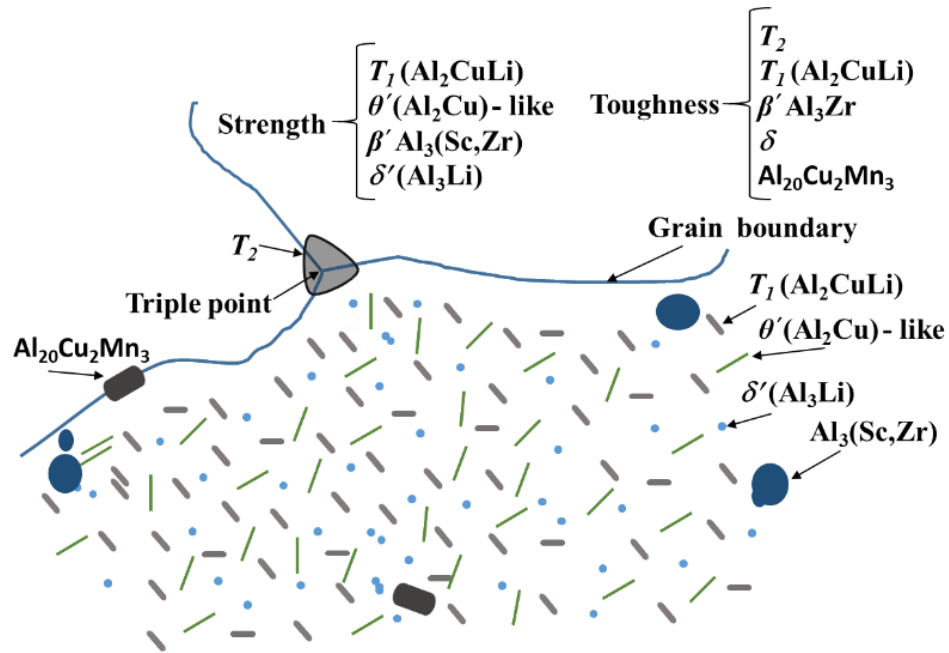


Figure 2.1 Schematic representation of microstructure in Al-Cu-Li alloys.

Similarly, addition of Sc has been more effective in Al alloys and has led to the formation of  $Al_3Sc$  dispersoids, which imparts sub grain stability and influence other attributes of recrystallization. A study performed by Suresh et al. (2018) on the effect of Sc addition on microstructure and mechanical properties in AA2195 alloy, has revealed the presence of high density  $Al_3(Sc,Zr)$  dispersoids. It was observed that, yield strength and hardness improved on Sc addition, which has attributed to decrease in grain size and strengthening, due to the presence of fine  $Al_3(Sc,Zr)$  dispersoids. Further, ageing kinetics was also accelerated due to Sc addition.

Distribution of  $Al_3Sc$  precipitates throughout the aluminum matrix effectively hinders the movement of dislocations and grain boundaries. As a result, this impedes recrystallization and enhances the overall strength of the alloy.  $Al_3Sc$  precipitates exhibit a comparable crystal structure and lattice parameters to the aluminum matrix, and they tend to maintain coherence with the aluminum matrix, leading to a coherent strengthening effect. It's important to note that these enhancements are particularly prominent when the  $Al_3Sc$  precipitates are relatively small in size. But it was reported that, these precipitates coarsened above 300°C, resulting in weakening of strength and recrystallization resistance of the alloy (Jiang et al. 2018).

Comparative work was conducted by Decreus et al. (2013) to understand the influence of Cu/Li ratio on the precipitate sequence and kinetics of two different Al-Cu-Li alloys: AA2198 (Li-lean (1.0 wt.%)) And AA2196 (Li-rich ( 2.0 wt.%)). It was found that in Al-Cu-Li systems, small variation in Li content had greater impact on precipitation sequence. For instance, Li-rich AA2196 showed the presence of  $\delta'(Al_3Li)$  phases throughout the precipitate sequence, whereas Li-lean AA2198 alloys were dominated by a Cu-rich clusters and GP zones during natural ageing which further dissolves to form  $T_1(Al_2CuLi)$  and  $\theta'(Al_2Cu)$  during artificial ageing.

In their study, Cassada, Shiflet, and Starke (1991) utilized TEM and HR-TEM to investigate the nucleation and growth process of  $Al_2CuLi$  ( $T_1$ ) precipitates. It was discovered that the nucleation and growth of  $T_1$  plates occurred through the dissociation of matrix dislocations into partials. These partials then form the growth interface of the plate as well as, plate edges. Further, examination of structural images provided insights into initial nucleation and growth of  $T_1$  plates. It was observed that the initial nucleation results in the formation of a hexagonal plate consisting of four (0001)-layers, equivalent to one unit cell. As the process continued, plate thickening took place through the addition of growth ledges. These ledges contribute four new layers of  $T_1$  material, as they move across the wider surface of the plate.

Deschamps et al. (2013) presented that Al-Cu-Li alloys containing only  $\delta'$  precipitates show high strain hardening rate, but the samples that contain only  $T_1$  shows lower strain hardening rate. However, larger than other precipitate hardenable aluminium alloys. The alloy systems that contain  $\delta'$  concurrently with  $T_1$  precipitates however showed further detonation in plastic properties. The normal precipitation sequence of various precipitates reported in aluminium alloys during aging of the supersaturated solid solution is tabulated below.

Xia et al. (2023) carried out a comparative study on interrupted aging treatment T6I6 and T6 aging treatment on 2195 alloy. Schematic representation of distribution of precipitates in T6I6 and T6 aging is shown in the Figure 2.2. Increase in density of  $T_1$  ( $Al_2CuLi$ ) phases within the interior of the grains and at the grain boundaries was observed in the T6I6 sample when compared to the T6

aged samples. This was due to the suppressing of nucleation and precipitation of  $\theta'$  ( $Al_2Cu$ ) phases during the low temperature interrupted aging.

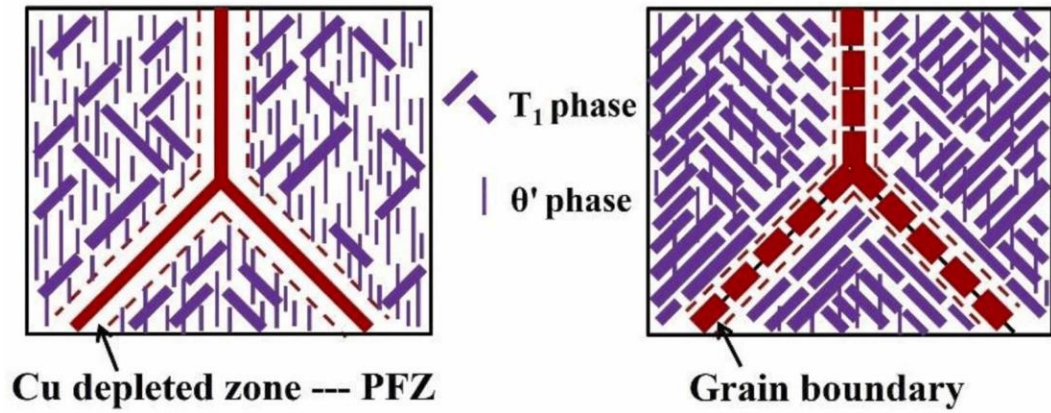


Figure 2.2 Schematic representation of distribution of precipitates after (a) T6 aging treatment and (b) T6I6 aging treatment on 2195 alloy (Xia et al. 2023).

Table 2.1 Precipitate sequence in common Aluminium alloys.

<i>Aluminium Alloy</i>	<i>Sequence of precipitates</i>	<i>Equilibrium precipitate</i>
Al-Cu	G-P zones(discs) $\rightarrow$ $\theta''$ (discs) $\rightarrow$ $\theta'$ (plates)	$\theta$ ( $CuAl_2$ )
Al-Ag	G-P zones (spheres) $\rightarrow$ $\gamma'$ (plates)	$\gamma$ ( $Ag_2Al$ )
Al-Zn-Mg	G-P zones (spheres) $\rightarrow$ $\eta'$ (plates)	$\eta$ ( $MgZn_2$ )
Al-Cu-Mg	G-P zones (rods) $\rightarrow$ $S'$ (laths)	$S$ ( $Al_2CuMg$ )
Al-Mg-Si	G-P zones (rods) $\rightarrow$ $\beta'$ (rods)	$\beta$ ( $Mg_2Si$ ) plates
Al-Cu-Li	G-P zones	$T_1$ ( $Al_2CuLi$ )
Al-Li	G-P zones $\rightarrow$ $\delta'$ (spheres)	$\delta$ ( $AlLi$ )

### 2.2.2 Effect of aging on Al-Cu-Li alloys

Aging of Al alloys promotes nucleation and growth of various secondary particles or precipitates within the grain interiors or grain boundaries. The shape, size, type and place (grain interiors or grain boundaries) of precipitate nucleation and growth depends upon several factors such as alloy composition, aging parameters such as time and temperature, pre aging heat treatments and pre aging deformation.

In a study by Jiang et al. (2019), artificial aging treatment of Al-Cu-Li alloy sheets at a temperature of 160 °C were investigated. The objective of the study was to investigate the impact of the aging duration on both the microstructure and

mechanical properties of the alloy. Evolution sequence observed during aging revealed that the major strengthening phases in the alloys were  $T_1$ ,  $\delta'$  and  $\theta'$ . Specifically, the sequence of strengthening phases observed during aging was  $SSS \rightarrow \delta', \theta', T_1 \rightarrow \theta', T_1$ . Increase in yield strength and tensile strength from 140 MPa and 250 MPa in SHT condition to 305 MPa and 376 MPa after 159 hours of aging were observed. However, further aging did not show any increase in strength, upon aging for 20 hours, YS and TS were found to be 300 MPa and 360 MPa respectively.

Balducci et al. (2017) Evaluated the effect of overaging on AA2050 alloy. Upon exposing the alloy to the aging temperature of 215 - 305 °C, its effect on microstructure and mechanical properties were evaluated. Microstructural analyses revealed that in the severely overaged state (after 24 hours at 305 °C), the  $T_1$  precipitates ( $Al_2CuLi$ ) dissolved, subsequently resulting in the formation and growth of  $\theta'$  and  $\Omega$  phases. However, this coarsening of precipitates resulted in increasing of strain hardening exponent. Hardness and tensile tests conducted at room temperature demonstrated higher strength properties in comparison to AA2099 across all over-aging conditions. Nonetheless, under severe over-aging conditions (24 hours at 305 °C), the alloy's performance was notably reduced in contrast to the peak aging condition.

### **2.2.3 Effect of pre-strain on precipitation and ageing kinetics in Al-Cu-Li alloys**

Duan et al. (2021) carried out detailed investigations to understand the effect of pre-rolling at different strains on microstructural evolution and precipitation in AA2195 Al-Cu-Li alloy. It was observed that, artificial aging at 200 °C on unprocessed or non pre-rolled samples resulted in a complicated precipitation behavior. Large sized  $T_1$  ( $Al_2CuLi$ ) precipitates were observed, due to abnormal precipitation, resulting in reduced density of  $T_1$  precipitates throughout the Al matrix during aging period. This is due to the lack of nucleation sites, as dislocation free recrystallized grains featured the initial non-rolled alloy. However, aging of pre-rolled samples resulted in nucleation of large density  $T_1$  phase, as the dislocations induced during rolling, act as the nucleation sites for precipitation. The initial stage precipitation of  $T_1$  phases inhibited formation of

other phases, making the precipitation behaviour simpler, unlike non-rolled samples. Figure 2.3 shows the schematic representation, depicting the precipitation evolution in non-rolled and rolled samples during artificial aging. Furthermore, it was observed that as the pre-strain increased, the precipitation kinetics of the  $T_1$  phase were significantly accelerated. This led to a reduced aging time required to achieve the peak aging condition.

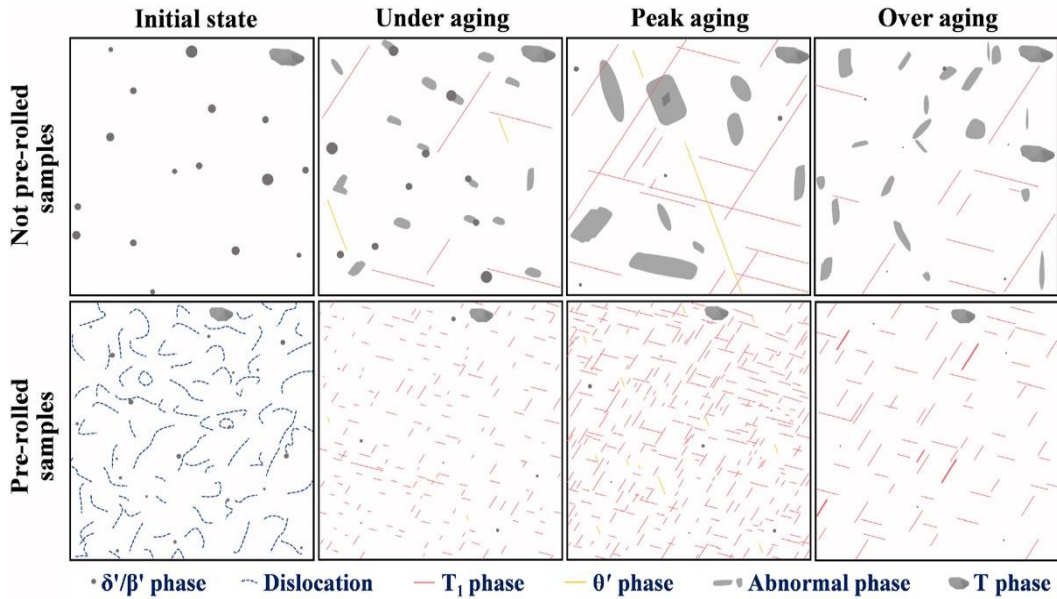


Figure 2.3 Schematic representation of precipitate evolution pre-rolled and pre-rolled AA2195 Al-Cu-Li alloy samples (Duan et al. 2021).

Wang and his co-researchers carried out a study to elucidate the effect of pre straining and natural aging on precipitation sequence and aging kinetics of Al–Cu–Li alloy during artificial aging. As shown in the Figure 2.4, it was found that, at the early stage of aging of pre strained samples, formation of GP zones were prevented by Mg–Cu co-clustering resulting in larger nucleation of  $T_1$  precipitates (Figure 2.4(c and e)). Further prolong aging showed rapid growth rate of  $T_1$  precipitates, thus enhancing precipitation kinetics (Figure 2.4(d)). It was also observed that, pre straining, prior to aging, has not only accelerated the aging kinetics, but also refined the  $T_1$  precipitates and higher  $T_1$  volume fraction were formed (Wang et al. 2020).

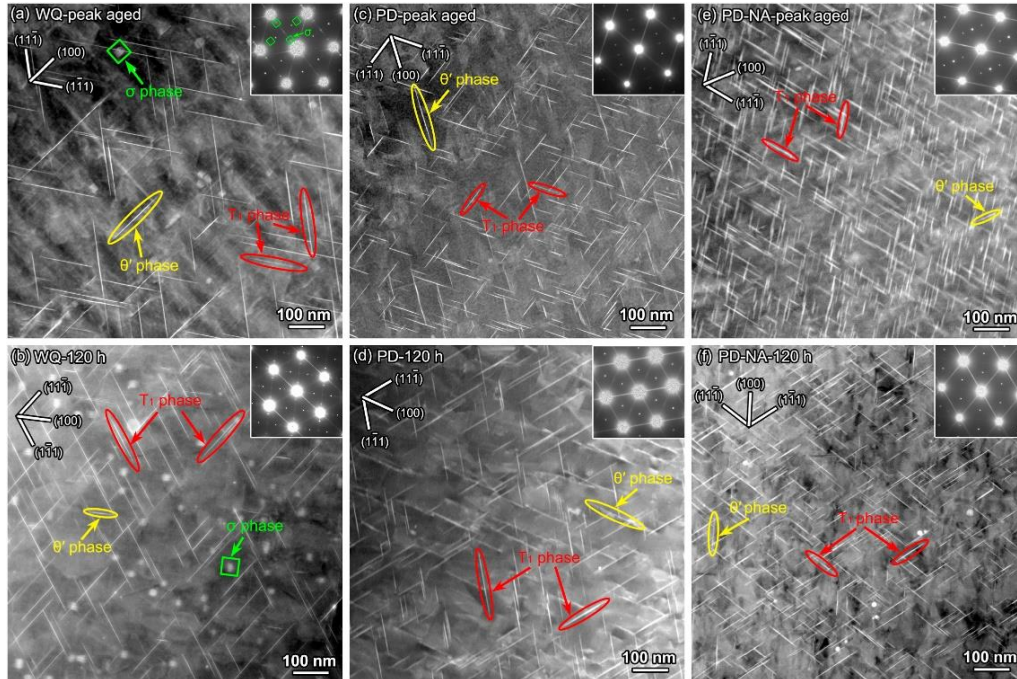


Figure 2.4 HAADF-STEM images captured in  $\langle 110 \rangle_{\alpha}$  zone axis of the specimens, representing both peak-aged and over-aged conditions. The samples examined were as follows: (a) and (b) WQ sample subjected to aging at 155 °C for 48 and 120 hours; (c) and (d) PD sample subjected to aging at 155 °C for 24 and 120 hours; (e) and (f) PD-NA sample subjected to aging at 155 °C for 24 and 120 hours (Wang et al. 2020).

Kim et al. (2003) reported similar findings of significant enhancement in mechanical properties of 2024 Al alloy after ECAP prior to aging. Accumulation of high dislocations density during ECAP processing and nucleation, and distribution of fine strengthening precipitates in aged state, attributes to increase in strength. Slight improvement in ductility was also reported in pre ECAP processed samples, compared to non-ECAP processed samples, after aging and was attributed to the annealing effect during aging.

Gable et al. (2001) conducted a study to investigate the impact of plastic deformation before artificial aging on the microstructural changes and mechanical properties of Al-Li-Cu alloy AF/C 458, which had a composition similar to that of AA2099. Solutionized samples (heat treated at 540 °C for 1h and subsequently water quenched) were immediately stretched upto 8% followed by artificial ageing at 150°C. TEM and XRD results showed the presence of  $Al_2CuLi$  ( $T_1$ ),  $Al_2Cu$  ( $\theta'$ ) and  $Al_3Li$  ( $\delta'$ ) strengthening precipitates. The results of this study indicated that plastic deformation prior to aging led to accelerated aging kinetics,

enhanced strength, and high density of strengthening precipitates due to the introduction of heterogeneous nucleation sites within the matrix. Additionally, it was noted that the relative volume fraction of  $T_1$  to  $\theta'$  significantly increased with an increase in deformation prior to artificial aging.

Building upon their previous research on the nucleation and growth mechanism of  $T_1$  precipitates, Cassada et al. (1991b) conducted further investigations to explore the influence of plastic deformation on  $Al_2CuLi$  ( $T_1$ ) precipitates. The solutionized material was stretched before aging at 463 K and observed significant effects on mechanical properties. Stretching of the material prior to aging resulted in a notable increase in observed yield stress at peak strength, varying from 20 to 25 percent. The extent of cold working played a major role in determining the exact increase in yield stress. Additionally, the material that underwent stretching of 4 to 8 percent, reached its peak strength, four to five times faster, compared to the unstretched material. Transmission electron microscopy (TEM) experiments were conducted to gain insights into the underlying mechanisms responsible for the improved alloy strength. Researchers found that the enhancement in relative alloy strength, was not solely attributed to  $T_1$  volume fraction. Stretching also played a significant role in increasing the number of nucleation sites for dislocations, leading to  $T_1$  formation. This was evidenced by substantial increase in the number density of  $T_1$  precipitates.

#### **2.2.4 Application aspects of Al-Cu-Li alloys**

Use of recent third-generation Al-Cu-Li alloys in structures that are critical to stiffness and weight in aerospace, military, and aviation applications has drawn attention (Warren 2004). Figure 2.5 depicts the proposed structural applications of 3<sup>rd</sup> generation Al-Cu-Li alloys, replacing conventional AA2024-T3 and AA7075-T6 aluminium alloys, in commercial transport aircraft. Utilization of aluminum-lithium (Al-Cu-Li) alloys in the aerospace industry can be traced back to the 1950s with the development of first-generation AA2020 Al-Li alloy, for applications in the wings of the Navy's RA-5C Vigilante aircraft.

Further 2<sup>nd</sup> generation Al-Li alloys (AA2090, AA2091, AA8090 and AA8091) were developed in the early 1980s. However, the second-generation alloys did not find considerable applications due to undesirable characteristics such as

anisotropic (in-plane and through-thickness) mechanical properties, lack of toughness and corrosion resistance. Micro-cracking during hole expansion, crack deviation and delamination also accounted for this. Low fracture toughness due to strong crystallographic textures along the short-transverse direction was the major shortcomings among the class of alloys. However, everlasting demand for high strength and less weight alloy designs for aircraft applications and intense works on alloy developments have resulted in the development of the third generation of Al-Li alloys. Careful optimization of composition, adaption of proper thermal-mechanical processing routes and precipitation control resulted in new generation alloys to overcome the shortcomings of second-generation alloys. Third generation Al-Cu-Li alloys have higher Cu/Li ratio than the second generation alloys (Heinz et al. 2000). Table 1.1 in Chapter 1 showed the detailed chemical compositions of the widely known Al-Cu-Li alloys among all the stages of their development. In order to maximize the payload, Reynolds Metals Ltd, the company in cooperation with Lockheed Martin and NASA, developed a third generation Al-Cu-Li alloy 2195 for cryogenic fuel tank in space shuttle launch systems. In 1994, cryogenic sections of Super Light Weight External Tank (SLWT) were fabricated using alloy 2195, replacing legacy 2219 aluminium-copper alloy (Rambabu et al. 2017). Later, forty of such SLWL were made by utilizing the reengineered alloy. The low lithium and copper content of the alloy provides higher specific strength and specific modulus than the alloy 2219. However, other alloys like 2197, 2096 and 2097, have lower copper content, but slightly higher lithium content than 2195 limited their applications.

In 2004, Alcan developed AA2050 alloy as an evolution of previously developed AA2195 to match or exceed the properties of legacy AA7050 aluminium-zinc alloy. In comparison to conventional AA7050 alloy, AA2050 alloy in addition to the density benefits, offers improved strength, toughness and corrosion resistance. Initial intent for the design of the alloy was to cater to requirements of thick frames and wing ribs in military aircraft. However, exceptional fracture toughness and stability at cryogenic temperatures extended for cryogenic tank applications (Dursun and Soutis 2014).

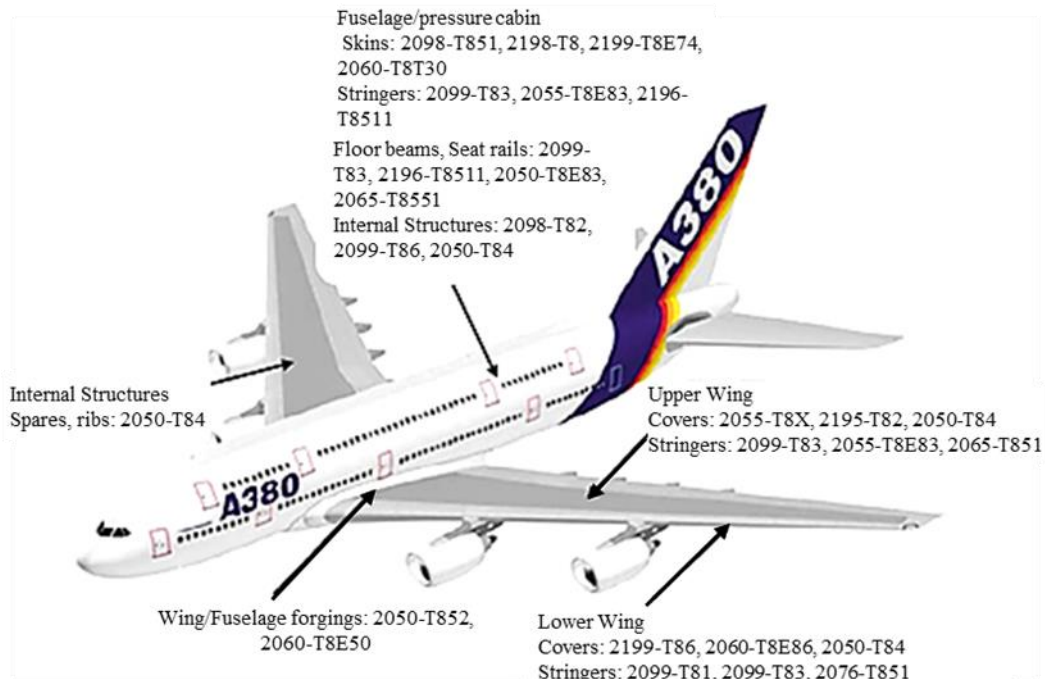


Figure 2.5 Actual and proposed application areas of third generation Al-Cu-Li alloys in a transport aircraft (Wanhill and Bray 2013).

### 2.3 Severe Plastic Deformation Techniques

The historical development of severe plastic deformation process can be traced back to the 19<sup>th</sup> century when the initial attempts to apply SPD principles in practical applications were made. In the early 1930s, Professor P.W. Bridgman, a Nobel Prize recipient, from Harvard University, conducted series of experiments involving the application of high pressure on bulk materials. His pioneering work, documented in the book "Studies in Large Plastic Flow and Fracture," showcased the processing of metals through a combination of compression and torsional straining, as detailed by Bridgman in (1952). This approach eventually evolved into the widely recognized high-pressure torsion (HPT) process. In 1980s, a new approach to SPD processing was introduced by Segal and his colleagues, known as Equal-Channel Angular Pressing (ECAP). This innovative technique has become the most significant and widely used method, among all other SPD processing techniques (Segal 1995a).

In 1999, Accumulative roll-bonding (ARB), another new concept of SPD was proposed by Saito et al. (1999) which involves repeated stacking of materials in the

form of sheets, in conventional roll-bonding to induce high plastic strain in the materials.

The increasing demand for producing UFG material for various applications and intensive research on the development of processes on achieving the same has resulted in the development of various SPD techniques to date. Some of the SPD processes reported in the literature to date are listed below:

- a. High-pressure torsion (HPT) (Bridgman 1952)
- b. Accumulative roll-bonding (ARB) (Saito et al. 1999)
- c. Multi-directional forging (MAF) (Salishchev et al., 1993; Valitov et al., 1994; Sitdikov et al., 2004)
- d. Cylinder covered compression (CCC) (Zhao et al., 2004)
- e. Equal-channel angular pressing (ECAP) (Segal 1995a)
- f. Constrained groove pressing (CGP) (Shin et al., 2002)
- g. Twist extrusion (Beygelzimer et al., 2004; Varyutkhin et al., 2006)
- h. Reciprocating extrusion (Chu et al., 2001)
- i. Friction stir processing (FSP) (Rhodes et al., 1997; Mishra and Ma, 2005)
- j. Cyclic extrusion/compression (Richert and Ritchert, 1986)

Above-mentioned SPD processes have the ability to introducing large plastic strain in the bulk crystalline solids, leading to significant grain refinements. Among them, some of the well-established methods are ECAP, MAF, ARB and HPT. These processes are capable of producing UFG materials having grain sizes with the range of ~70–500 nm. In the following part of this section, some of the well-developed SPD techniques and their principles are briefed.

### **2.3.1 Equal Channel Angular Pressing (ECAP)**

ECAP is a well-known and well studied SPD process which involves imparting large plastic strains on the metal billet by pressing through a die consisting of two equal cross-section channels as shown in Figure 2.6. Typically, the angle at the intersection lies between 90° to 120°. The seminal works of (Iwahashi et al. 1997; Langdon et al. 1998; Segal 1995b) experimentally demonstrated the ECAP process and its effect on microstructural development. Later, several researchers introduced various sample process routes, where the billet orientation is altered after every press in a sequence. Considerable literature on understanding the effect

of various ECAP process parameters such as die angle, processing temperature, pressing velocity, processing route, number of passes etc., were also reported.

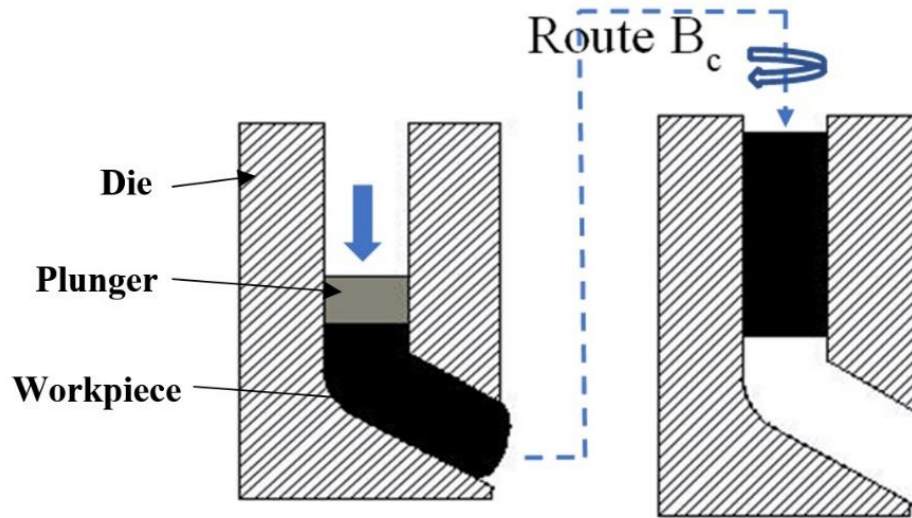


Figure 2.6 Schematic representation of Equal Channel Angular Pressing process.

Iwahashi et al. (1997) carried out experimental investigations to develop UFG pure aluminium with an initial size of  $\sim 1.0$  mm using ECAP process and were successful in achieving an equi-axial UFGs of  $\sim 1$   $\mu\text{m}$  after 10 passes. The die was designed to impose a strain of  $\sim 1.05$  in each pass and processing route C was adopted, where the samples were rotated by  $180^\circ$  between each pressing. The result concluded that pure aluminium can be successfully processed by ECAP at room temperature to achieve ultra-fine grains.

Mao et al. (2005) carried out a studies on microstructure and tensile properties of the 2024 alloy subjected to ECAP with initial aging treatment conditions. ECAP processing has resulted in the formation of ultrafine grains measuring around  $0.25$   $\mu\text{m}$  on both peak-aged and over-aged conditions. Upon subsequent annealing up to  $300^\circ\text{C}$ , there was limited grain growth. An increase in proof stress and ultimate tensile strength (UTS) was observed for both peak-aged and over-aged specimens after ECAP pressing up to two passes. These values remained relatively constant with an increasing number of passes. Similarly, elongation to failure decreased up to two passes and showed a slight increase with further processing for both peak-aged and over-aged conditions. The work concludes that subjecting the alloy to peak aging treatment before ECAP pressing significantly enhances the strength of the alloy, resulting in notably high strengths after ECAP when compared to the

over-aged alloy. Similar investigations were carried out by Zhao et al. (2004) in which he investigated the impact of ECAP on the mechanical properties and precipitate kinetics of a solution-treated Al 7075 alloy. The solutionized specimens were subjected to two passes of ECAP using route Bc with a die featuring an intersecting channel angle of  $90^\circ$  and an outer arc angle of  $45^\circ$ . The kinetics of phase precipitation were notably accelerated, although there was no observed alteration in the sequence of phase precipitate formation. The strength of the naturally aged ultra-fine grained 7075 alloy was significantly higher than that of its naturally aged coarse-grained counterparts. This finding highlights the potential to combine the strengthening effects resulting from ECAP processing with those from precipitation hardening.

Suresh et al. (2019) successfully processed Al-Cu-Li alloy AA2195 using ECAP upto 4 passes (cumulative strain  $\sim 4$ ) following route C at  $250^\circ\text{C}$ . After four ECAP passes, grain size reduction from  $56 \pm 3.5 \mu\text{m}$  to  $2.8 \pm 0.7 \mu\text{m}$ . Enhancement in hardness, yield strength, and ultimate tensile strength were observed and were attributed to dislocation strengthening, precipitation strengthening and grain boundary strengthening, with increase in ECAP passes. EBSD analysis revealed an increase in fraction of high angle grain boundaries and the average of grain boundary misorientation angle with increase in number of passes. TEM results showed the occurrence of CRDX which led to the formation of fine grain structure and also attributed to weakening of overall texture.

### **2.3.2 High Pressure Torsion (HPT)**

In High pressure torsion, grain refinement was accomplished by the combined compression and shear stresses induced on the work material. Figure 2.7 illustrates the schematic of simple HPT setup. The combined effect of pressure and larger shear strain results in larger refinement in microstructure compared to other SPD processes. However, some researchers reported that the variation in strain imposed along the radial direction was zero at the center and maximum at the outer region.

Lee et al. (2012) successfully enhanced the strength of AA2091, an Al-Li-Cu-Mg alloy, by implementing a two-step process consisting of grain refinement through High-Pressure Torsion (HPT) and subsequent age hardening. Through

HPT applied to the solid-solution treated alloy, they achieved a reduction in grain size of approximately 140 nm. Vickers microhardness exhibited an increasing trend with higher levels of strain and eventually stabilized at a constant value of 225 HV. By subjecting the HPT-processed alloy to aging at temperatures of 100 °C and 150 °C, the hardness was further elevated to approximately 275 HV. Bending tests conducted on samples treated under optimal aging conditions demonstrated a significant increase in stress, accompanied by the retention of considerable ductility. Observations made, using transmission electron microscopy, revealed that fine grains achieved through grain refinement persisted even after extended periods of aging. Furthermore, within these fine grains, precipitation of fine  $\delta'$  particles were observed, confirming the concurrent strengthening effects resulting from both grain refinement and age hardening.

Kaigorodova et al. (2018) carried out TEM characterisation on high-pressure torsion processed Al-Li-Cu alloy AA1461. The alloy, in solution treated state, is HPT processed under a pressure of 4 GPa, at room temperature. Upon HPT, the developed microstructure consisted of nanofragmented and nano grains formed in the course of partial dynamic recrystallization. Artificially aged alloy at 160°C for 32 hours showed homogeneous precipitation of  $\delta'$  and  $T_1$  phases whereas HPT, at room temperature, showed heterogeneous precipitation of dispersed  $T_2$  phase, and no  $\delta'$  and  $T_1$  phases are detected. Tensile test results showed an increase in the elastic modulus and a slight decrease in the plasticity and is mainly due to the formation of a mixed structure.

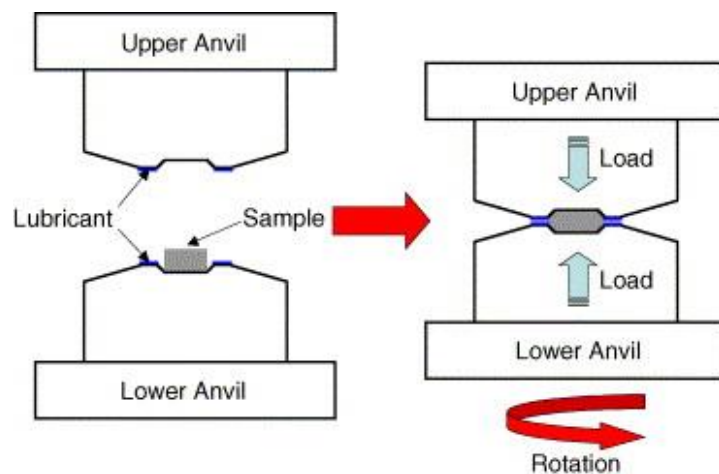


Figure 2.7 High pressure torsion (Sakai et al. 2005).

### 2.3.3 Friction Stir Processing (FSP)

Another most commonly used SBD technique for bulk material processing is friction stir processing (FSP). It involves the utilization of a rotating tool that is inserted into the work material and moved along the intended path, as illustrated in Figure 2.8. The application of intense strain on the material beneath the tool shoulder leads to significant refinement of the microstructure. This deformed area is referred to as the stir zone. Friction at the interface during the process generates substantial heat, which affects the region surrounding the stir zone, commonly known as the heat-affected zone.

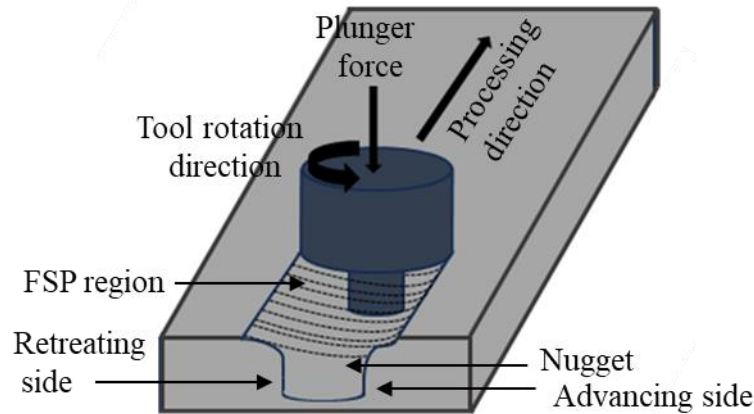


Figure 2.8 Friction stir processing technique.

Zhu et al. (2017) carried out a comparative studies on microstructural changes and mechanical characteristics of Al-Cu-Li AA2198-T8 alloy processed by two distinct SPD techniques—friction stir processing (FSP) and high-pressure torsion (HPT). Microstructural analysis demonstrated that grain refinement could be achieved in both the process (FSP and HPT) in Al-Cu-Li 2198-T8, with HPT yielding significantly finer grains. The mechanical characterization revealed a slight decrease in hardness and strength of FSPed alloy in comparison with as received state, while HPT processed alloy demonstrated a substantial increase in strength and hardness due to high degree of grain refinement and dislocation density. The findings indicate that in the as-received base material, the primary mechanisms for enhancing strength are precipitation hardening and dislocation strengthening. In the case of FSP-processed 2198-T8 alloy, a significant portion of the strength improvement can be attributed to grain refinement and solid

solution formation. On the other hand, in HPT-processed 2198-T8 alloy, the dominant factors contributing to strength enhancement are dislocations and grain boundaries.

#### **2.3.4 Limitation of the above discussed SPD techniques**

Despite the positive outcomes of aforementioned SPD processes in terms of grain refinement and improved mechanical properties, they are not without their drawbacks. One major disadvantage is the high processing temperature involved in these SPD techniques. Even when performed at room temperature, materials still experience high temperatures due to the intense plastic deformation and the significant amount of frictional heat generated during the process (Moradi et al. 2009). Ghazani and Shaban (2014) demonstrated that the temperature of Al-Mg alloy can reach upto 100 °C during ECAP at room temperature, further highlighting the issue of temperature rise during SPD. At these elevated deformation temperatures, aluminum tends to recover by eliminating the stored dislocations due to its high stacking fault energy (Sarma et al. 2010). As a result, large strain is required to effectively refine the microstructure. Moreover, in age-hardenable alloy systems like Al-Cu-Li alloys, high processing temperature during SPD leads to dynamic precipitation. However, precipitates formed under such conditions tend to be coarse in nature and do not significantly contribute to enhancement of mechanical properties through precipitation hardening. Additionally, dynamic precipitation depletes the solute concentration in the solid solution, which limits the feasibility of post-process aging techniques aimed at producing nano-sized precipitates (Ke et al. 2010).

Given these factors, there is a clear demand for a low-temperature SPD process that offers several advantages over high-temperature techniques:

- 1) **Suppression of dislocation annihilation:** It is essential for the low-temperature SPD process to effectively suppress dislocation annihilation through dynamic recovery. By doing so, the material can attain high strength even with a relatively low imposed strain. This would enable the production of refined microstructures and enhanced mechanical properties, without the requirement for excessively high deformation strains.

2) Prevention of dynamic precipitation: Another crucial aspect of the low-temperature SPD process is the ability to prevent dynamic precipitation. By avoiding the occurrence of dynamic precipitation during deformation, the material's mechanical properties can be further improved through subsequent post-process aging. This ensures that the benefits of precipitation hardening, such as the formation of nano-sized precipitates, can be fully utilized to enhance the material's strength and other desirable properties.

By addressing these two key requirements, a low-temperature SPD process has the potential to offer significant advantages over high-temperature techniques. This can lead to the development of materials that possess superior mechanical performance and microstructural characteristics.

#### **2.4 Multi-Axial Forging – An effective solution**

MAF, also known as multi-directional forging, is considered one of the simplest and extensively explored SPD techniques. MAF is based on the principles of plane strain deformation, primarily due to the constraints imposed by the plunger and die assembly used in the process. In a work carried out by Aoba et al. (2017), a systematic investigation was carried out to understand the microstructure evolution and changes in the mechanical properties of Al 6000 series alloys subjected to MAF, as well as, subsequent artificial aging following the MAF process. The aim was to analyse how MAF, and the subsequent aging treatment affect the material properties. The solutionized samples of initial average grain size of 230  $\mu\text{m}$  were MAF processed up to 40 passes (i.e; cumulative strain of  $\sim 16$ ) at room temperature and isothermally aged. Upon MAF, with increase in cumulative strain, the initial coarse grains fragmented by shear bands formation. At the end of 40th MAF pass, an ultrafine grained structure with average grain size of 220 nm was reported with an increase in UTS from 150 MPa (Solutionized) to 310 MPa. Further, improvement in strength by 31 MPa after aging at 393 K was reported. Change in precipitation behavior in MAF processed sample in comparison with coarse grained samples, were also observed.

Cherukuri, Srinivasan and Chaudhury (2005) carried out the heat treatment of AA 6061 after severe plastic deformation. AA 6061 samples in solutionized (W) condition were severely deformed by MAF to produce ultrafine grain (UFG)

structures in the order of 0.5 microns. Hardness and tensile testing of W tempered and MAF processed material was carried out at 120 °C, 170 °C and 200 °C at different times. The results were compared to conventionally aged material. Hardness and tensile properties of the MAF processed samples showed peak ageing at shorter periods indicating accelerated precipitation.

Khamsepour and Kazeminezhad (2020) examined the effect of strain rate on flow stress of RT-MAF processed and RT-MAF + annealing on pure aluminium. Annealing was carried out at different temperatures (150 °C, 200 °C, 350 °C and 450 °C) for 1 hr. Increase in number of passes increases dislocation density and thus yield strength and hardness. Strain rate too had a significant effect, as yield strength increased with increase in strain rate. Annealing of MAF processed samples at 150 °C did not affect hardness and yield strength. However, with increase in annealing temperature, due to recrystallization, the effect of strain rate becomes insignificant as the dislocations annihilated.

In a study conducted by Kapil et al. (2019), the impact of Cryo-MAF (cryogenic multi-axial forging) and RT-MAF (room temperature multi-axial forging) on the fracture toughness of AA8090 alloys was investigated. Results showed that Cryo-MAF, performed up to a cumulative strain of 3.6, resulted in a 15% increase in fracture toughness compared to RT-MAF. Additionally, other mechanical properties also exhibited improvements. In contrast to RT-MAF condition, tensile strength and yield strength increased by 12% and 9%, respectively, and the elongation decreased by 25% for the Cryo-MAF samples processed up to a cumulative strain of 3.6. The strengths exhibited by the Cryo-MAF processed AA8090 alloys were found to be superior to those of other coarse-grained aluminum alloys. This improvements in strength was a result of suppression of dynamic recovery and the presence of an ultrafine-grained (UFG) microstructure, which is a result of Cryo-MAF process.

#### **2.4.1 Principle of MAF process**

The simple and inexpensive MAF process involves, repetitive compression of prismatic shaped samples along their three orthogonal axes. In MAF process, same amount of average strain is imposed in all the compression steps. Figure 2.9 shows the schematic representation of the MAF process. The process involves

compression of the specimen inside a confined die which allows the lateral expansion of the specimen until faces contact the die walls. The plunger of die cavity dimensions is used to apply a large compressive force on the specimen. Till the specimen faces come in contact with die walls, the process is much similar to a free compression process. The flat die walls result in the formation of flat and parallel opposite faces on the sample and this eliminates the need for machining between each press. In MAF process, One cycle is referred to as the three consecutive orthogonal compressions or presses along the specimen's X, Y, and Z axes, as shown in Figure 2.10.

Among the various SPD techniques discussed in section 2.3, MAF offers several advantages:

**a. Simple Process:** MAF is a relatively simple process that involves repeated compression. It can be performed using conventional forging or hydraulic presses, making it easily accessible and cost-effective. This simplicity allows for practical implementation without the need for specialized equipment.

**b. Determination of Flow Stress:** MAF enables the systematic determination of the flow stress versus strain relationship. This is achieved by applying sequential compressions while changing the pressing directions. This feature provides valuable insights into the material's behavior and allows for precise control and optimization of the deformation process.

**c. Grain Shape retention:** MAF maintains the original shapes of the grains throughout the process. As a result, the analysis of deformation substructures becomes simpler.

**d. Easily scalable:** MAF has the potential for industrial application, particularly for large-scale workpieces. The technique can be seamlessly integrated into existing conventional forging machines with the use of simple dies. This scalability and compatibility with established industrial practices make MAF an attractive option for implementing SPD in industrial settings.

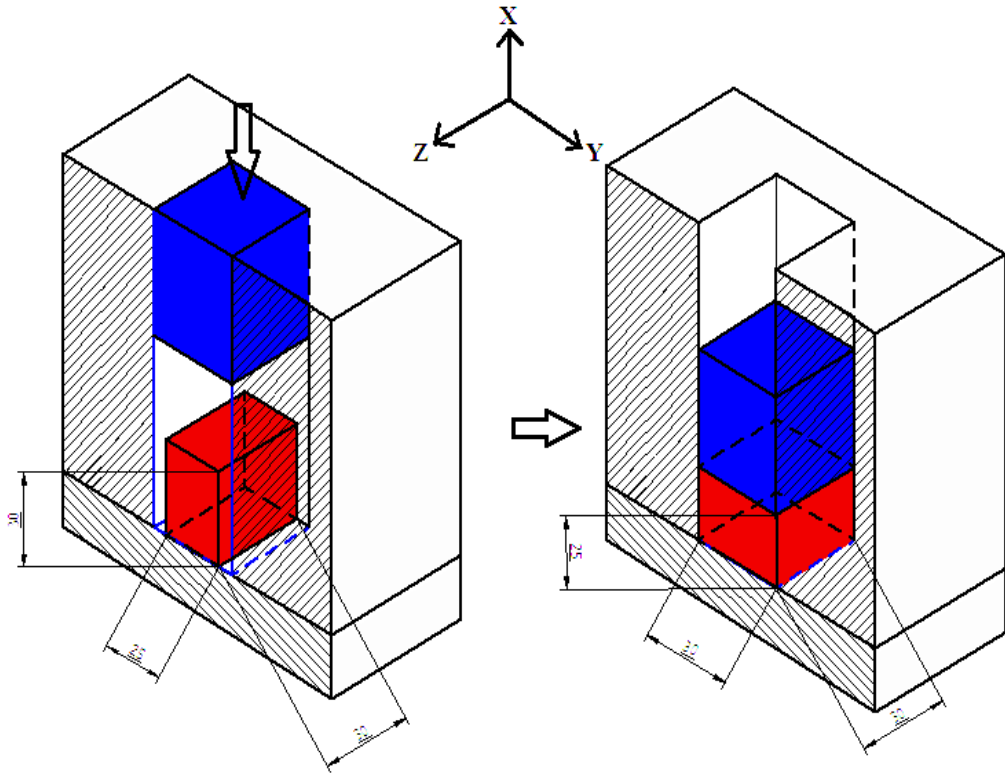


Figure 2.9 Sectional representation of MAF setup.

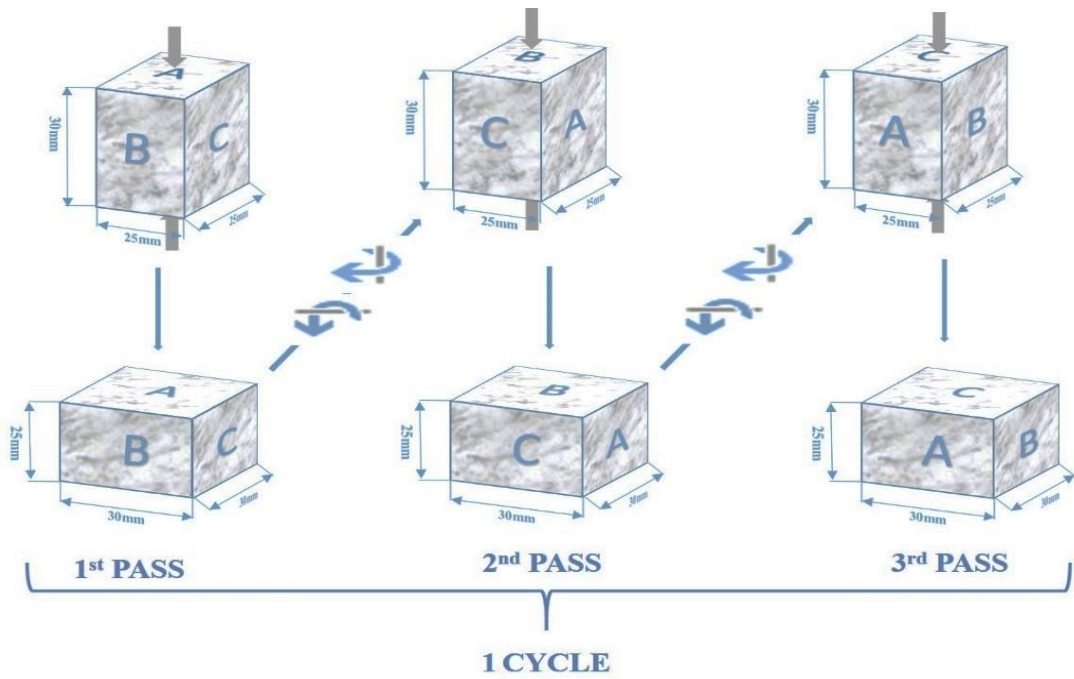


Figure 2.10 Process sequence of Multi Axial Forging.

### 2.4.2 Strain imposed in MAF

The total strain accumulated in the billet depends on the number of cycles, it has been processed through. Equation 2.1 gives the amount of strain imposed in each pass of MAF process. Total strain imposed per cycle is the summation of strains imposed in three sequential orthogonal compressions or pressings along the X, Z and Y-axes of the specimen, is given by Equation 2.2. Higher strains per pass can be achieved by increasing  $h_i/h_f$  ratio.

$$\epsilon_{pass} = \ln \frac{h_i}{h_f} \dots\dots\dots \text{Equation 2.1}$$

Where,  $\epsilon_{pass}$  is the strain imposed per pass,  $h_i$  and  $h_f$  are initial and final height of the sample.

$$\epsilon_{cycle} = \epsilon_x + \epsilon_y + \epsilon_z \dots\dots\dots \text{Equation 2.2}$$

Where,  $\epsilon_{cycle}$  is the strain imposed per cycle,

$\epsilon_x$ ,  $\epsilon_y$  and  $\epsilon_z$  are strains imposed in each pass along the X, Z and Y axis of the specimen in three sequential orthogonal pressings.

### 2.4.3 Factors affecting MAF process

a) **Pressing Speed (Strain rate):** Pressing speed, also known as strain rate, is a crucial factor in any SPD process, as it significantly influences grain size and mechanical properties. It is widely recognized that higher strain rates can lead to the production of fine grain sizes through dynamic recrystallization. However, employing high rate of strain can result in faster hardening rate and sample breakage due to suppression of recovery mechanisms.

b) **Pressing Temperature:** Pressing temperature during SPD plays a vital role in determining the grain refinement mechanism and the resulting microstructure evolution (Sakai et al. 2014). Materials with high stacking fault energy can experience dynamic recovery at elevated deformation temperatures, which necessitates larger strains to achieve microstructure refinement. In case of age-hardenable aluminum alloys, especially, when processing occurs after solution treatment, it is preferred to maintain low pressing temperature. This is because higher temperature can accelerate dynamic precipitation during deformation stage itself, which is not a favorable condition for the age hardenable class of alloys.

**c) Lubrication:** In MAF process, proper lubricating medium is essential at the die-specimen, specimen-plunger, and the die-plunger interfaces. Friction, at this interface, act as barriers for deformation to occur and results in heat generation, that can further affect the final microstructure, particularly when processed at low temperatures.

## 2.5 Hall - Petch Relation

Hall-Petch Relation was initially proposed to quantify the strengthening effect of grain boundaries in polycrystalline metals (O Hall E, 1951). However, its applicability has extended to a wide range of boundaries introduced by plastic deformation. Flow stresses, within a crystal, upon reaching a critical value, break the grain boundaries and then the dislocations will be converted to adjacent grains. Further the relation between flow stress and the grain size  $d$  is given by,

$$\sigma_o \propto \frac{1}{d^{1/2}} \dots\dots\dots \text{Equation 2.3}$$

In single crystal, since flow is restricted below its yielding stress  $\sigma_y$ , the above equation is further modified as below.

$$\sigma_o - \sigma_y \propto \frac{1}{d^{1/2}}$$

Or  $\sigma_y = \sigma_o + kd^{-(1/2)} \dots\dots\dots \text{Equation 2.4}$

Where  $\sigma_o$  and  $k$  are constants.  $\sigma_o$  is the flow stress of an undeformed single crystal or approximately the yield stress of a very coarse-grained, textured polycrystalline metal. The above Hall-Petch relation expresses the dependency of the lower yield point or the fracture stress on the grain size. The empirical validity of the Hall-Petch relation (Equation 2.3) has sparked extensive research and development in grain refinement techniques for various metals and alloys. The results obtained from several studies consistently demonstrate good agreement with Equation 2.4, supporting the utilization of Hall-Petch relation for enhancing the yielding strength of materials.

## 2.6 Literature Overview

In a study by Calderon and Morris (2008), rolling operations were performed on

solutionized Al-Cu-Li alloy. The alloy was heat treated at 540°C of 1 hour, followed by water quenching. The samples were rolled at various temperatures, and the evolution of deformation precipitates and substructures was examined. Rolling process induced a high density of dislocations in the material, which were retained regardless of the rolling temperature. Strength and ductility of the rolled samples exhibited significant variations depending on the rolling temperature. Interestingly, both strength and ductility reached their maximum values at higher temperatures. The findings from this study suggest that selection of processing temperature plays a crucial role in determining the mechanical properties of the Al-Cu-Li alloy.

Additionally, Sun et al. (2019) investigated the impact of adding Zn to Al-Cu-Li alloy in different proportions, up to 1.1%. The influence of microstructural characterisation on the alloys mechanical properties was the primary focus of study. In accordance with microstructural studies, Zn addition caused more MgZn<sub>2</sub> phases to develop at the grain boundaries. Also, grain size was also considerably refined as a result of Zn addition. Additional research was done to evaluate the mechanical characteristics of 4Cu-1Li-0.1Zr alloys that were extruded under various circumstances (T4, T6, and T8). Zn addition was found to improve the alloys yield strength (YS) and ultimate tensile strength (UTS) without having a negative impact on its ductility.

In their review, Rioja and Liu (2012) focused on evolution of Al-Li alloy based products specifically designed for aerospace and space applications. Challenges associated with the 2<sup>nd</sup> generation Al-Li alloys, such as 2090-T81 plate, 8090-T86 plate, and 2091-T84 sheet were discussed. One of the key drawbacks identified with these alloys was their through-thickness anisotropy. The review emphasized the importance of understanding the underlying metallurgical causes behind these undesirable characteristics and the need for key alloy design principles.

Chen et al. (1998) developed multistep heating rate controlled aging treatment process to enhance fracture toughness at cryogenic temperature of AA2195 alloy. The studies showed that, the cryogenic fracture toughness decrease considerably with increase in density of  $T_1$  precipitates at subgrain boundaries and their size in the matrix. Similar trends were observed with ambient temperature fracture

toughness, as well. Further, higher strengths were achieved by promoting  $T_1$  and  $\theta'$  nucleation in the matrix, rather at the sub grain boundaries.

Chen and Bhat (2002) conducted TEM analysis to investigate the time-temperature-precipitation (TTP) behavior of an AA2195 Al-Cu-Li alloy. The alloy was subjected to a 3% stretching deformation and then solutionized for 1 hour prior to heat treatments. A series of heat treatments were performed at temperatures ranging from 365 K to 810 K for varying durations up to an hour. TTP diagrams were constructed separately for the matrix and subgrain boundary regions of the alloy. These diagrams provided valuable information about the precipitation behaviour of different phases. Based on the TTP diagrams, various precipitate phases were identified in the alloy, including GP zone,  $\theta'$ ,  $\theta$ ,  $\delta'$ ,  $T_1$ ,  $T_B$ , and  $T_2$ . These precipitate phases exhibited distinct formation kinetics and temperature ranges. The TTP diagrams served as a reference for inhibiting the precipitation of  $T_1$  phases specifically at subgrain boundaries thereby enhancing the alloy's cryogenic fracture toughness.

Suresh et al. (2018) carried out the systematic studies on understanding the effect of Sc addition on mechanical properties and microstructural evolution of AA2195 Al-Cu-Li alloy. Addition of 0.25wt% Sc accelerated ageing kinetics and reduction in grain size. Formation of  $Al_3(Sc,Zr)$  dispersoids led to the improvement in yield strength and hardness. However slight decrease in ductility was observed leading to change in fracture mode.

## **2.7 Corrosion of Al-Cu-Li alloys**

Aluminium and its alloys possess wide range of properties, including high resistance to corrosion in various service conditions. This is primarily attributed to the formation of a self-protecting thin oxide layer on the surface, when exposed to atmosphere. This oxide layer provides excellent corrosion resistance to aluminium. However, it should be noted that, alkalis have the potential to destroy this protective layer, leading to surface corrosion (Davis 1999). In the context of aerospace applications, the widely used AA2XXX series alloys have been found to be highly susceptible to localized forms of corrosion rather than uniform corrosion. Examples of localized corrosion include intergranular corrosion (IGC), pitting corrosion, crevice corrosion, exfoliation, and stress corrosion cracking.

Among these localized corrosion forms, intergranular corrosion (IGC) and pitting corrosion are particularly significant in aluminium alloys. IGC refers to preferential attack occurring at grain boundaries or adjacent regions without substantial attack of the grain matrix. On the other hand, pitting corrosion takes place at intermetallic particles or within the grain matrix. These localized forms of corrosion can be particularly problematic, as they lead to localized material degradation, reduced structural integrity, and potential failure. Therefore, understanding and mitigating the risks, associated with intergranular corrosion, pitting corrosion, and other localized corrosion forms, are crucial in ensuring long-term durability and reliability of aluminium alloys used in aerospace applications.

Aluminium alloys are known to exhibit good corrosion resistance in most working environments. One of the main factors that affects the corrosion behavior of Al-Cu-Li alloys is the alloy's elemental composition. Al-Cu-Li alloys typically contain between 2-7% copper and 0.5-2.5% lithium as the major alloying elements. Copper contributes for increase in corrosion resistance, while the presence of lithium can enhance the corrosion susceptibility of the alloy, particularly in acidic environments. The microstructure of the alloy can also impact its corrosion behavior, with finely dispersed precipitates or grain boundaries being more prone to corrosion than more homogeneously distributed ones. Several research has been carried out in recent times to understand the corrosion behavior and various factors that affect the corrosion properties of Al-Cu-Li alloys.

Jiang et al. (2020) carried out a study to understand the effect of aging time on corrosion properties of Al-Cu-Li alloy. The corrosion surface morphology of sample aged at 160 °C after polarization studies in 0.6 M NaCl solution is shown in Figure 2.11. From Figure 2.11, it is evident that the corrosion modes were consistent and identified as IGC for all the aging durations. However, grain boundary attack was more severe in 26 hours aged samples. This resulted in the separation of entire grain region from the alloy. However, grain interior were less corroded. From the Figure 2.11, it is clear that at lower aging duration, grain boundaries dissolve first and the corrosive medium then diffuse into the sample

through the grain boundaries. When an increase in aging time corrosion diffuses into the grain interiors resulting in corrosion of entire grain.

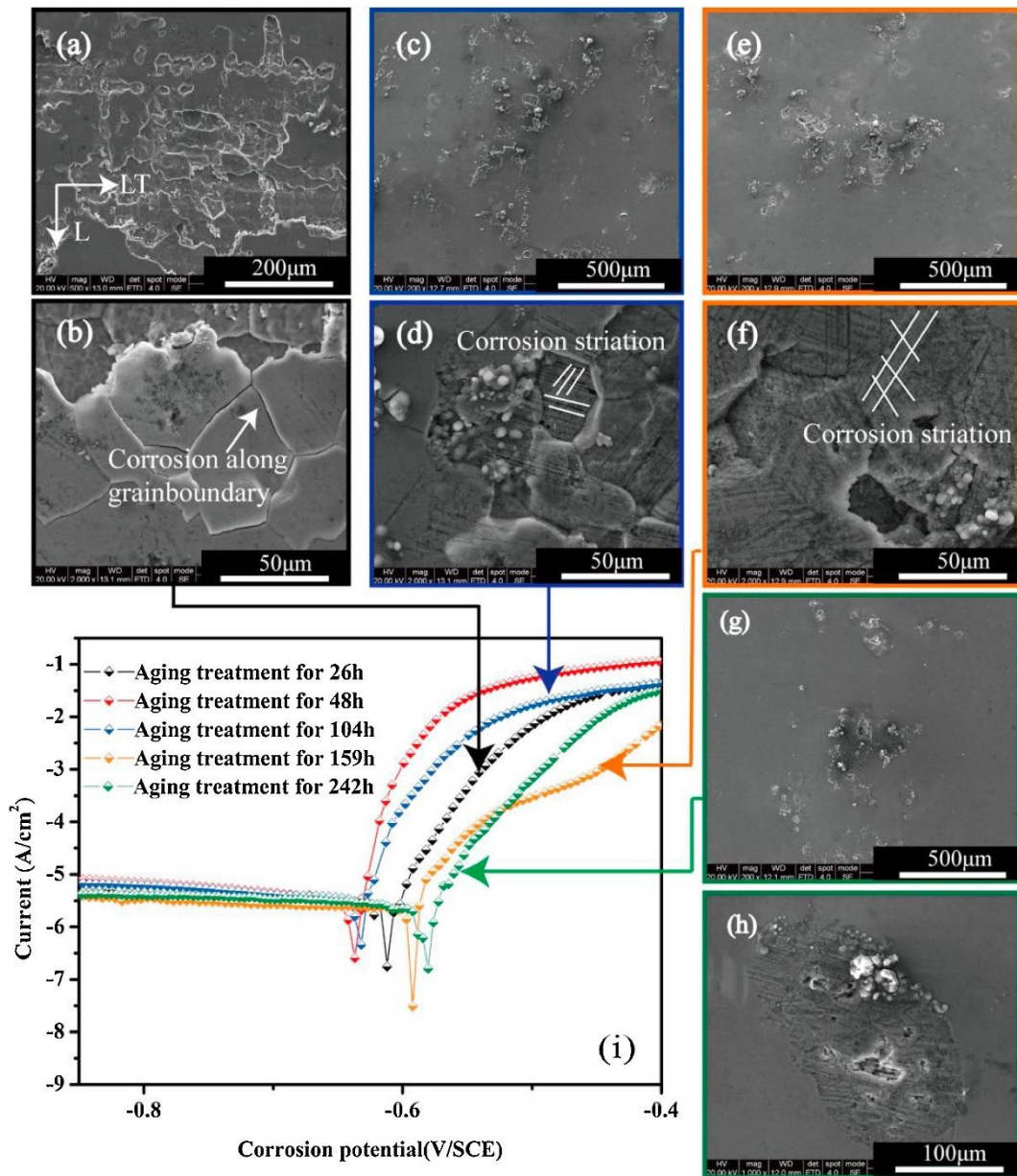


Figure 2.11 Corrosion surface morphology of Al-Cu-Li alloy observed during aging for (a,b) 26 h, (c,d) 104 h, (e,f) 159 h and (g,h) 242 h, and (i) represents the respective potentiodynamic polarization curves (Jiang et al. 2020).

Ye et al. (2018) studied the effect of annealing on AA2050 Al-Cu-Li alloy prior to solution treatment on intergranular corrosion (IGC) behaviour. Reduction in open circuit potential with ageing, has been observed for both solution treated (ST) and annealing + solution treated (AST) conditions. This is because different precipitates that are formed upon ageing, have different electrochemical potentials

compared to matrix. It was also observed that both ST and AST samples, without ageing, remained immune to IGC, due to homogeneous microstructure, as the potential at both grain interior and grain boundaries remain almost same, and does not drive IGC.

## **2.8 Wear behavior of Al-Cu-Li alloys**

Wear properties of Al-Cu-Li alloys are critical factor as they significantly impact durability and serviceability of the alloy when used for structural applications. Therefore, wear properties are crucial when designing engineering parts, that undergo wear and tear, under different operating conditions. Microstructure, hardness, and surface topography primarily influence the wear resistance of Al alloys (Kumar et al. 2007). Various wear mechanisms, including adhesive, abrasive, delamination, and fatigue wear, can occur in Al-Cu-Li alloys, depending on the operating conditions. While common techniques like heat treatment and surface coating can improve wear properties, as wear resistance is generally proportional to the hardness of metals and alloys. However, despite improving strength and hardness, surface modification techniques, such as shot peening, ball burnishing (Ramesh et al. 2021a) and laser shock peening, have shown limited effectiveness in resisting wear (Chang et al. 2021; Rodríguez et al. 2019). Therefore, strengthening the matrix through grain refinement, has emerged as a promising method for improving wear resistance. It is worth knowing that, SPD processing of materials results in grain refinement to nanometer or sub-micrometer regime (Azushima et al. 2008).

The impact of SPD on the wear characteristics of alloys has been a topic of debate in the literature. While some studies have reported an enhancement in wear resistance in materials subjected to SPD processing, while others have reported a decrease. Kim et al. (2004) processed AA6061 Al alloy by ECAP and performed wear analysis of ECAP processed samples. It was found that wear resistance decreases in ECAP processed samples. Similarly, Wang et al. (2011) reported reduction in wear resistance, with no significant changes in coefficient of friction, in ECAP processed AA1050 Al alloy. Another study on accumulative roll bonding (ARB) processed pure Al alloy sample showed higher wear rate, compared to unprocessed alloy, with a slight increase in wear rate at lower normal loads and

much higher at higher loads (Talachi et al. 2011). On the other hand, pin-on-disc dry sliding wear tests on Al–Cu alloys with 2, 3 and 5% Cu showed improved wear resistance after ECAP processing. With increase in the number of ECAP passes, increase in wear resistance was observed (Abd El Aal et al. 2010). Ortiz-Cuellar et al. reported improved wear resistance under lubricated conditions after ECAP processing of Al–Mg–Si alloy (Ortiz-Cuellar et al. 2011). Reduction in wear rate of 92.5% and 85.4% was obtained in nanostructured 2024 Al alloy samples compared to coarse-grained Al2024-O and Al2024-T6 alloy conditions (Jafari et al. 2010). However, impact of aging on the wear properties of Al alloys processed by SPD prior to artificial aging has yet to be explored.

## **2.9 Motivation for the proposed work**

Aluminium alloys have significant applications in aerospace industries for nearly a century, because of their excellent strength and light weight. As compared to polymer based composites, Al alloys have various advantages. Composite materials are often considered for wing and fuselage structures. But, composite materials also have certain drawbacks of higher certification and production costs. Also composites are prone to moisture absorption and can exhibit softening or becoming brittle under hot or extreme cold operating environments. These factors contribute to the continued preference for aluminium alloys in the aerospace industry, as they offer a unique balance of strength, lightweight properties, recyclability, ease of fabrication, and flame-retardant characteristics that are crucial for aircraft applications.

In addition to the development of higher performance aluminium alloys by the industry, there is an increasing interest in optimizing the utilization of materials as an additional and complementary approach to enhancing airframe structure performance. Al-Cu-Li alloys are finding increasing applications in the latest and upcoming generations of commercial aircraft, especially in applications that require high specific strength and exceptional damage tolerance.

Although most recent studies have focused on severely deformed, low Li content aluminum alloys, there is a lack of literature addressing alloy stability for these alloys. Moreover, little information about the effect of deformation temperature, and in particular cryogenic temperature, on the material properties exists.

Existing literature indicates that deformation or working, such as stretching, performed subsequent to solution heat treating and quenching, leads to a more evenly dispersed arrangement of lithium containing metastable precipitates during artificial aging. The process involves subjecting the material to deformation prior to heat treatment, which introduces significant number of defects (such as dislocations, vacancies, and vacancy clusters). These defects serve as preferential sites for nucleation, promoting the formation of additional metastable precipitates uniformly within each grain. This combination of uniform precipitation throughout each grain and reduced precipitation at grain boundaries contributes to the superior combination of strength and fracture toughness observed in aluminium-lithium alloys.

During the SPD processing of materials that are susceptible to precipitation hardening, several phenomena can occur, influenced by factors such as the deformation process, deformation temperature, initial tempering procedures, and strain level. Although the behavior can be complex, some general observations are summarized:

1. Precipitates that were previously present in the material before to SPD processing either gradually fragment during deformation or dissolve or continue to precipitate. Temperature and strain conditions have a significant impact on the occurrence and extent of precipitates formed.
2. The presence of Guinier-Preston (GP) zones in fine grain structures formed during SPD processing at room temperatures has not yet been completely defined.
3. Solution heat-treated alloys do not processes precipitates. However, subjecting to SPD at high temperatures significantly accelerates dynamic precipitation, leading to the formation of new precipitates during the deformation process.
4. Artificial aging process following SPD of solution-treated materials has significant impacts on precipitation kinetics. It promotes more uniform distribution of lithium-containing metastable precipitates throughout the grains, further enhancing the material's properties.

Considerable research was carried out on the precipitation evolution and its impact on the mechanical properties of Al-Cu-Li alloys. However, to effectively

utilize the full potential of 3<sup>rd</sup> generation Al-Cu-Li alloys, to obtain exceptional mechanical properties, grain refinement, through SPD, has been identified as a promising approach. It is believed that combination of enhanced uniform precipitation, within grains and reduced precipitation at grain boundaries, contributes to the observed superior combination of strength and fracture toughness in Al-Cu-Li alloys. Present study aims to address the research gap that exists in previous studies, by investigating the effect of MAF followed by artificial aging on precipitate hardenable Al-Cu-Li alloys. This specific approach of MAF has not been explored extensively in the past, and its potential impact on the microstructure characteristics and mechanical behaviour of Al-Cu-Li alloys remains unexplored. By focusing on this novel processing technique, we aim to gain a deeper understanding of its effects and evaluate its viability for enhancing the performance of Al-Cu-Li alloys.

## **2.10 Objectives of present work**

In a pursuit of demonstrating the multi axial forging as a potential method for achieving high strength ultra-fine grained third generation AA2050 Al-Cu-Li alloy, the following objectives are framed:

- a. To develop ultrafine grained third generation AA2050 Al-Cu-Li alloy by thermo-mechanical processing through multi axial forging and post deformation artificial ageing.
- b. To investigate microstructural development and mechanical behaviour of the MAF processed AA2050 Al-Cu-Li alloy.
- c. To study the influence of post deformation ageing treatment on mechanical and microstructural properties of MAF processed AA2050 Al-Cu-Li alloy.
- d. To evaluate the corrosion behaviour of the developed ultrafine grain third generation Al-Cu-Li alloy.
- e. To evaluate the effect of MAF and post deformation ageing treatment on wear behaviour of Al-Cu-Li alloys.



## **CHAPTER 3**

### **EXPERIMENTAL WORK**

#### **3.1 Introduction**

The current study investigates the impact of MAF and artificial aging after MAF on the third generation AA2050 Al-Cu-Li alloy. This chapter provides a comprehensive overview of the material used, MAF setup, processing parameters, various characterization techniques employed, and their corresponding sample preparation procedures. The chapter commences with a discussion of the elemental composition of AA2050 Al-Cu-Li alloy, which serves as the basis for understanding its properties and behavior under different conditions. Subsequently, this chapter delves into the sample preparation procedure for MAF processing, including the steps involved and the equipment used to carry out the process. The different characterization techniques utilized in this study and the corresponding sample preparation techniques employed are further discussed in detail.

#### **3.2 Material selection and procurement**

The broader objective of this study is to enhance the utilization of Aluminium alloys in aerospace and aircraft applications by modifying their microstructure through thermomechanical processing. A thorough review of existing literature has revealed that the 3<sup>rd</sup> generation Al-Cu-Li alloys possess significant potential in the aerospace and aircraft industry. Consequently, the present investigation focuses on studying the lightweight AA2050 Al-Cu-Li alloy. The commercial AA2050 alloy was procured from Bharat Aerospace Alloys Pvt. Ltd. in Mumbai, India.

To ensure the adherence of material composition to necessary standards, the elemental composition of the AA2050 alloy was assessed using Optical Emissive Spectroscopy (OES) technique. The findings were then compared to the standard data, and the results are presented in Table 3.1. Comparison analysis shows that the elemental compositions of the procured material are within the standard limits established by the Aluminium Association (AA).

Table 3.1 OES results and comparison with standard data.

AA2050 Al-Cu-Li alloy		
Elements	Standard range (wt.%)	OES results (wt.%)
Cu	3.2-3.9	3.53
Li	0.7-1.3	0.85
Zn	0.02-0.25	0.033
Mg	0.20-0.6	0.358
Mn	0.2-0.5	0.345
Zr	0.06-0.14	0.0868
Ti	0.10 max	0.0375
Fe	0.07 max	0.0511
Si	0.05 max	0.0354
Be	0.0001 max	-
Al	Remainder	94.2

### 3.3 Multi Axial Forging (MAF)

MAF is an economical and relatively simple SPD method compared to other established techniques. The experimental setup of MAF process generally comprises three primary components: the die, forging press, and heating arrangement. The die retains the material that needs to be deformed, whereas the forging press exerts the requisite force for deforming the material. The heating arrangement is utilized for heating the material to the required temperature.

#### 3.3.1 Die Setup

Figure 3.1 displays MAF die setup in (a) assembled and (b) exploded view utilized in the current study. The die setup comprises two split dies, which are made from AISI H11 Hot Die Steel (HDS) with a composition of 0.4wt% C, 0.4wt% Mn, 1.1wt% Si, 5wt% Cr, 1.2wt% Mo, and 0.5wt% V. The dies are bolted together to create a single unit that forms a square-groove of 30 mm x 30 mm. The bottom surface of the die is supported by a base plate, that not only provides support to the die, but also rests on the Universal Testing Machine (UTM) bed. Figure 3.1 (c) depicts the assembled die setup on UTM bed. Some of the salient features of MAF die setup are,

- a. Dimension of die side plate: 100 x 100 x 50 mm
- b. Dimension of base plate: 100 x 100 x 25 mm
- c. Dimension of plunger: 30 x 30 x 150 mm
- d. Overall die dimensions as one part: 100 x 100 x 125 mm
- e. Dimensions of inner die cavity: 30 x 30 x 100 mm
- f. Clearance between the inner die cavity and plunger wall: 0.2 mm
- g. Die material: AISI H11 Hot Die Steel heat treated to hardness of 60 HRc
- h. Two die halves are bolted together with four sets of bolts and nuts.

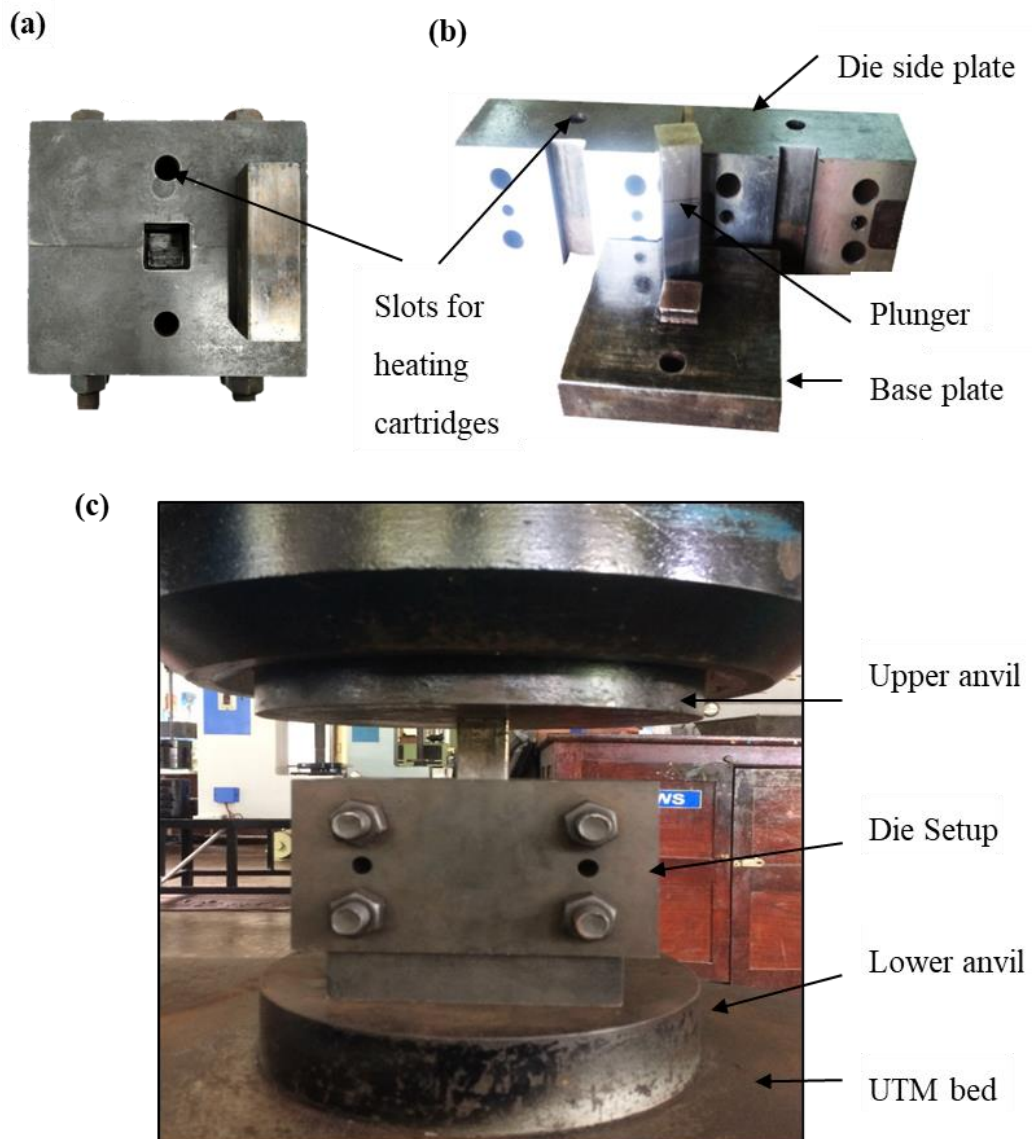


Figure 3.1 MAF die setup in (a) the assembled and (b) the exploded view, (c) assembled die setup on UTM bed.

### 3.3.2 Forging Press

A 100-ton hydraulic press (UTM) with fine control over load and displacement was used to carry out MAF process. The base plate of the assembled die is positioned directly on the bottom anvil or UTM bed, while the upper anvil transfers the load via a plunger, as depicted in Figure 3.1 (c).

### 3.3.3 Heating setup

To execute MAF process at temperatures higher than ambient conditions, specialized attachments comprising heating cartridges and temperature controller have been employed. Two heating cartridges are placed into the slots provided on the die side plates and connected to a control panel. A thermocouple is inserted inside the die to record the actual die temperature and provide feedback to the control panel. The die is covered with ceramic wool to prevent heat loss and enable effective temperature control. The arrangement of the temperature control unit attached to a MAF die is depicted in Figure 3.2.



Figure 3.2 100-Ton UTM with MAF die and heating setup.

### 3.3.4 MAF Procedure

AA2050 Alloy was received in the form of rectangular slabs of approximately 450 x 110 x 50 mm in size. The as-received materials were then cut down into smaller prismatic blocks, measuring 24mm x 30mm x 30mm, using a combination of a power hacksaw and a lathe with a four-jaw attachment. After machining, blocks are solution heat-treated (SHT) and immediately subjected to MAF process. SHT treatment involves heating the blocks at  $515 \pm 5$  °C for a time of 1 hr 30 min and immediate water quenching. After SHT, the blocks were placed inside the die setup at a pre-set temperature for 10 minutes. Once the sample reaches the desired temperature inside the die, the plunger is pressed at an optimized strain rate.

After the first pass, the block is rotated to the next forging axis, as previously explained, and then placed back inside the die for 5 minutes before the next pass. This process is repeated for consecutive passes. Figure 3.3 presents the machined block before MAF process and after MAF processing. Based on the number of trial experiments that were carried out and from the literature, the pressing speed, soaking time, and other related parameters were optimized and are reported in Table 3.2.

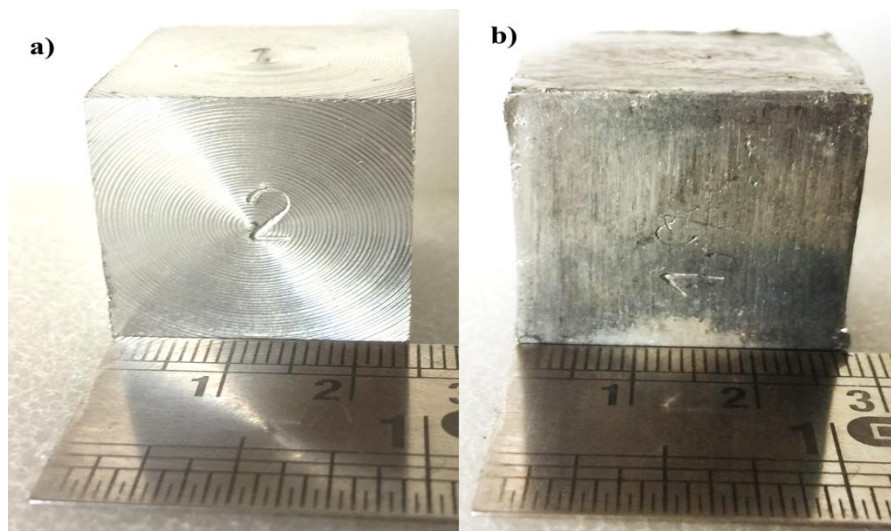


Figure 3.3 Machined prismatic sample a) before MAF processing, b) after MAF processing.

Table 3.2 List of Optimization parameters for MAF process.

Sl. No.	Parameter	Optimized Condition
1	Pre-Deformation Heat treatment	Solution Heat treatment
2	Solution Heat treatment	515 ± 5 °C for 1 hr 30 min
3	Number of MAF passes	12 passes (4 cycles)
4	MAF temperature	170 °C
5	Pressing speed	2 mm/ min
6	Post Deformation Heat treatment	Artificial ageing
7	Ageing temperature	125, 155 and 175 °C

### 3.3.5 Artificial Aging Heat Treatment

Several sets of SHT and MAF processed samples were subjected to artificial aging heat treatment. Aging was carried out at three different temperatures (125 °C, 155°C and 175°C) upto a time period of 80 hours. To evaluate the variation of hardness over the time period, for all the three aging temperatures, at regular time intervals, set of samples were aged and examined for microhardness. Aging was carried out in an in-house developed low temperature furnace, equipped with closed loop PID controller, to monitor the temperature continuously and accurately. Samples, after SHT and MAF process, were immediately subjected to aging, to prevent the effect of natural aging. Samples were air cooled to room temperature, after the desired duration of aging.

### 3.4 Structural characterization

The specimens under various processed conditions were subjected to several characterization techniques. The samples for all structural characterization from MAF processed blocks are extracted from the near mid-plane perpendicular to the previous forged axis. Samples were cut using a low-speed sample cutting metallurgical saw, with continuous supply of coolant, to prevent the effects of heat generated during cutting. Similar steps were followed to extract the samples after artificial ageing heat treatment. The subsequent sections provide a brief discussion of the several characterization methods and the corresponding sample preparation techniques used in the current study.

### **3.4.1 Optical microscope**

Samples for optical microscopy are polished to mirror-finish surface using standard metallurgical sample preparation procedure. This process involves mechanically polishing of samples on silicon carbide emery sheets up to 2000 grade. The process is further followed by polishing with 3-micron and 1-micron diamond paste, using diamond aerosol spray as a lubricant. For all optical microscopy observations, the samples are etched using Kellar's reagent (5ml HNO<sub>3</sub> + 3ml HCl + 2ml HF + 190ml H<sub>2</sub>O) approximately for 13 seconds.

### **3.4.2 Microstructural characterization by FESEM-EBSD**

Electron back scattered diffraction (EBSD) technique utilizes focused beam of high-energy electrons to probe the crystal structure of a sample. Sample is bombarded with a beam of electrons and the diffraction patterns that are produced are collected and analyzed. The diffraction patterns are the results of interaction between the electron of the atoms in the sample, and they can provide information about the crystal structure, grain orientation, and other microstructural features of the sample. Sample preparations for EBSD analysis involves mechanical polishing using silicon carbide sheets up to 2000 grade followed by electro polishing. Electro polishing was carried at 12V for 15 seconds at -20 °C using 20% Nitric acid and 80% methanol as an electrolyte.

EBSD attachment (EDAX-AMETEK Inc., USA) integrated into a field emission gun-scanning electron microscope (FE-SEM) (Model: Gemini 300, Make: Carl Zeiss, Germany) was utilized. To illustrate the setup, refer to Figure 3.5, which presents a schematic representation of a typical SEM-EBSD system.



Figure 3.4 FESEM setup with EDAX and EBSD attachment.

During the experiments, specimens were fixed to a pre-tilted brass holder using conductive silver paste. The holder had a tilt angle of  $70^\circ$ , resulting in a  $20^\circ$  tilt relative to electron beam. With an accelerating voltage of 20 kV, SEM-EBSD measurements were conducted. The commercial Texture and Elemental Analytical Microscopy software (TEAM TM) provided by EDAX-AMETEK Inc. was utilized to automatically acquire the orientation information from the Kikuchi diffraction patterns. This software facilitated the analysis of microstructure and microtexture.

The scan step-size has been varied from ( $0.5 \mu\text{m} - 2 \mu\text{m}$ ) depending on the processing conditions of the specimens. For the deformed materials, the scans were performed with a fine step-size, ( $0.5 \mu\text{m}$ ), whereas the step-size varied from ( $1 \mu\text{m} - 2.5 \mu\text{m}$ ) for non-deformed specimens. Obtained raw data were analyzed using TSL-OIM TM (EDAX-AMETEK Inc., USA) software. Key parameters for the microstructural analysis include average grain size (GS), GS distribution, low- and high-angle grain boundaries (LAGBs and HAGBs), twin boundaries (TBs), and misorientation angle distribution were obtained.

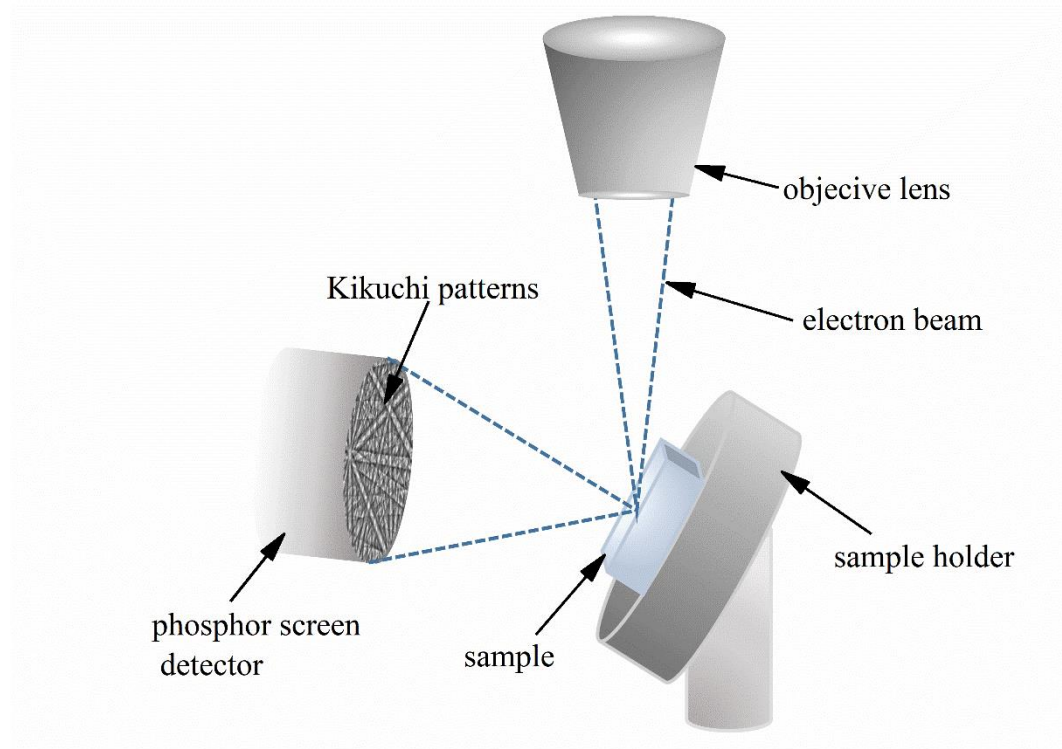


Figure 3.5 Schematic representation of FESEM EBSD setup.

### 3.4.3 Transmission electron microscope (TEM)

To gain insights into the microstructural evolution and precipitate formation within selected specimens, TEM (Transmission Electron Microscopy) studies were conducted. A TEM operating at 200 kV (Model: JEM-2100; Manufacturer: JEOL, Japan), as depicted in Figure 3.6, was employed for this purpose.

Standard sample preparation technique was followed for sample preparation. Initially, mechanical polishing was performed using silicon carbide emery papers, until a thickness of 300 microns was achieved. Subsequently, 3 mm discs were punched out from the mechanically polished sheets. These discs were further polished using a disc grinder to reduce the thickness to approximately 80 microns, followed by dimple grinding, resulting in further thinning. To achieve electron transparency necessary for TEM examination, the specimens were thinned using Argon ion milling at 4.5 kV (PIPS-691, Gatan Inc.) for a duration of 30 minutes.



Figure 3.6 Jeol JEM-2100 Transmission Electron Microscope

#### 3.4.4 X-Ray diffraction (XRD)

XRD measurements were carried out in the  $2\theta$  range of  $20^\circ$  to  $105^\circ$  at a step size of  $0.06^\circ$  at room temperature using Malvern Panalytical's Empyrean diffractometer fitted with Cu  $K\alpha$  ( $\lambda = 0.1542$  nm) source. The measured XRD patterns are analyzed using Xpert Highscore V3 software for determining the secondary phase formation when subjected to MAF processing and artificial thermal treatment. Further quantitative analysis of XRD patterns were carried out on MAF processed and post MAF aged samples to determine the crystallite size ( $D$ ), microstrain ( $\epsilon L$ ) and Dislocation density ( $\rho$ ) via Rietveld refinement using Pan analytical's Xpert highscore software. Standard Silicon sample was used to determine the effect of instrumental broadening.

For the bulk texture measurements, the most commonly used Schulz Method of texture measurement is adopted (Socrates 2003). This method involves stereographic projection of pole densities in the form of intensities obtained from X-ray diffractions at a particular (hkl) plane. This stereographic projection also known as pole figures depicts the position of pole densities of crystallographic plane with respect to the sample reference axis. The diffraction data is obtained using Cobalt  $K\alpha$  X-ray source of wavelength ( $\lambda = 1.79$  nm) for three different (hkl) planes. Cobalt source is selected

to eliminate the perchance of fluorescence resulting from the sample. The sample is tilted upto  $75^\circ$  with standard step sizes of  $5^\circ$  and for every tilt, sample is rotated from  $0^\circ$  to  $360^\circ$ . To overcome the effect of defocusing error, the maximum tilt is limited to  $75^\circ$ . In Schulz method of XRD measurements (Decker et al. 2004), background intensities vary with increase in tilt angle, thus background error creeps in. To overcome the effect of background intensities on actual peak intensities, background correction is made by measuring the background intensities separately along the  $2\theta$  angle and integrating it over the  $\chi$ . Thus the corrected pole figure intensity is obtained from the following equation (Suwas and Ray 2014).

$$I_{corrected} = I_{measured}(\varnothing, \varphi) - I_{background}(\varnothing)$$

Where,  $I_{corrected}$  is the corrected pole figure intensity,  $I_{measured}(\varnothing, \varphi)$  is the experimentally measured intensity and  $I_{background}(\varnothing)$  is the background intensity measured separately.

Bulk texture measurements of samples in various processed conditions were recorded in Panalytical EMPYREAN diffractometer according to Schulz reflection geometry. Four incomplete pole figures were measured on three (hkl) planes namely (111), (220) and (200) for all the sample conditions. All the measurements were carried out with tilt range of  $\varphi = 0^\circ - 75^\circ$  and sample rotation of  $\varnothing = 0^\circ - 360^\circ$  with step size of  $5^\circ$ . Further, analysis of bulk texture measurements was performed on ATEX software.

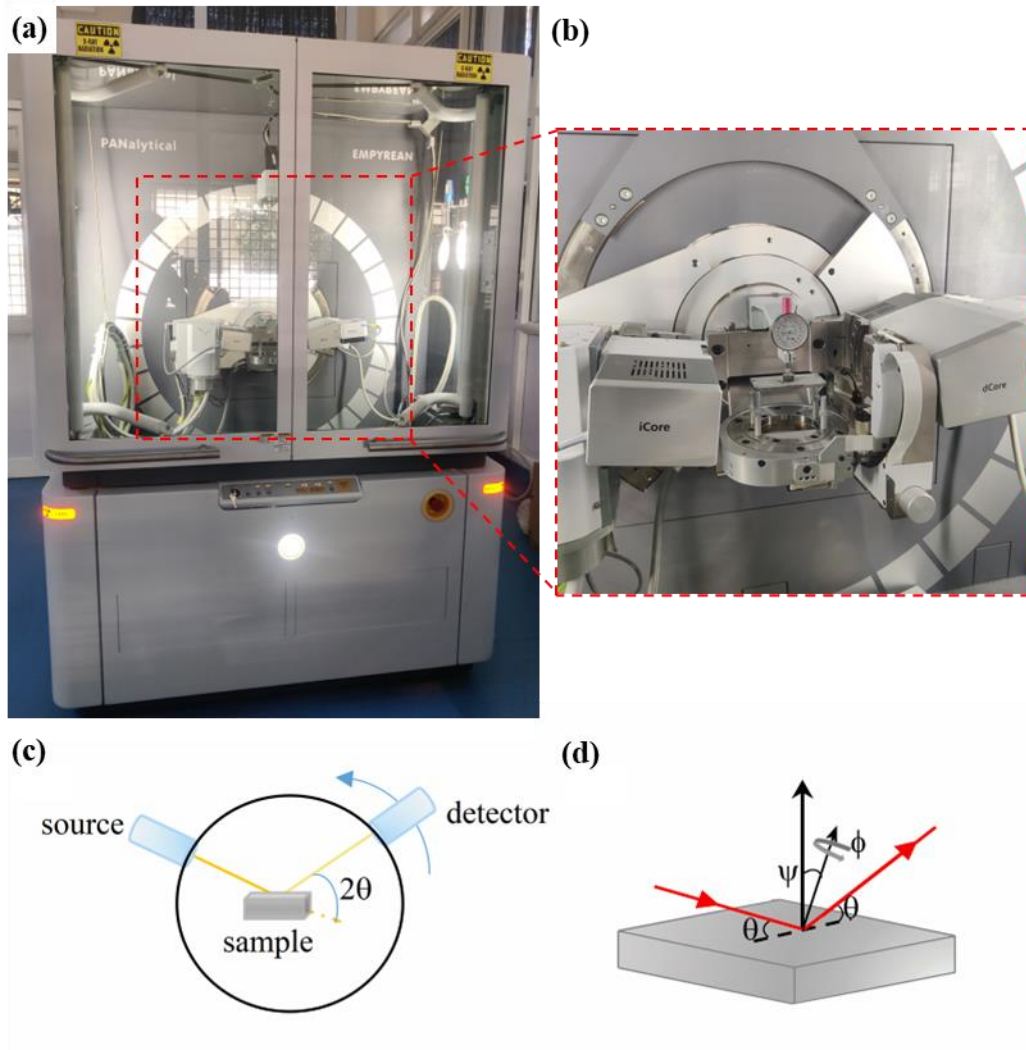


Figure 3.7 (a) PANalytical EMPYREAN diffractometer, (b) Sample holder with source, detector and goniometer configuration, and (c, d) schematic representation of X ray diffraction.

### 3.5 Mechanical properties evolution

To gain a comprehensive understanding of the mechanical behavior of AA2050 alloy under different processed conditions, a thorough investigation of its mechanical properties was carried out. This investigation involved the utilization of two key testing methods: microhardness testing and tensile testing. Experimental procedures and parameters utilized for both microhardness and tensile testing were carefully standardized to ensure accurate and reliable results. Multiple samples were tested for each processed condition to obtain statistically significant data and establish the repeatability of the findings.

### 3.5.1 Vicker's Micro-Hardness Characterization

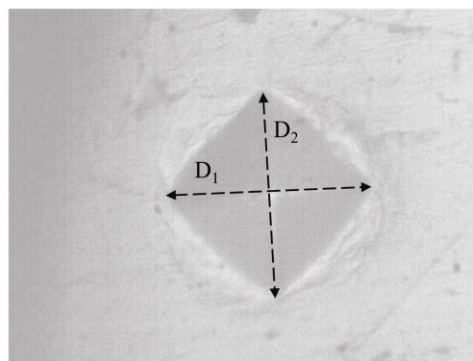
Vickers micro-indentation hardness tests are performed on all material conditions (i.e., solution treated, MAF processed and post MAF heat treated samples) and for each processed condition, a minimum of five indentation results are recorded and the average values are reported. Microhardness tests were carried using Omnitech microhardness tester shown in Figure 3.8(a). All hardness measurements were recorded on a mirror polished flat sample surface at different locations by applying weight of 150 grams for a dwell period of 15 seconds. Indentation on sample surface is shown in Figure 3.8 (b), and distance between the diagonal are recorded. Vickers microhardness (HV) is calculated using the Vickers hardness formula as shown in Equation 3.1.

$$HV = \frac{0.1891 * F}{d^2} \quad \text{Equation 3.1}$$

Where,  $F$  is the load applied (measured in kilograms-force, kgf) and  $d$  is the area of the indentation (measured in square millimetres, mm<sup>2</sup>).



(a)



(b)

Figure 3.8 (a) Vickers microhardness tester, and (b) indentation on the sample surface.

### 3.5.2 Tensile testing

The schematic representation of tensile specimens can be observed in Figure 3.9(a). It is worth noting that a minimum of three sets of samples were tested for each processed condition. Tensile specimens were prepared according to the ASTM E8 Subsize standard, as depicted in Figure 3.9(b). To assess the tensile properties of the alloy in different conditions under ambient temperatures, a floor-mounted universal tensile machine (UTM) manufactured by Shimadzu (Model: AGX-V2) was employed, as illustrated in Figure 3.9(c). Circular gripper utilized to securely hold samples during the testing process is illustrated in Figure 3.9(d). All tests were conducted at an initial strain rate of  $10^{-3} \text{ s}^{-1}$ .

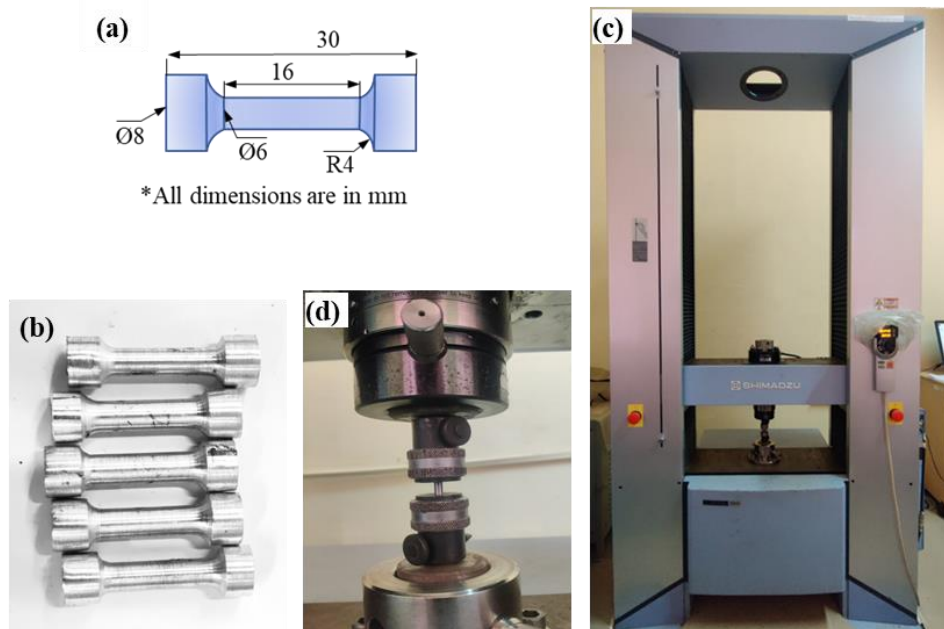


Figure 3.9 (a) Schematic of tensile sample as per ASTM E8 subsize standard, (b) AA2050 tensile samples as per ASTM E8 subsize standard, (c) Shimadzu 40KN universal testing machine, and (d) magnified portion of (c).

## 3.6 Corrosion studies

### 3.6.1 Electrochemical studies

Open circuit potential (OCP) and potentiodynamic polarization tests were performed to investigate the effect of MAF process and the combined effect of MAF and post MAF artificial ageing treatments on corrosion behaviour of AA2050 Al alloy. All the electrochemical measurements are recorded using three-electrode configuration system with graphite as the reference electrode (RE), saturated calomel electrode as counter

electrode (CE) and aluminium (sample) as the working electrode (WE). A surface area of 1.0 cm<sup>2</sup> of the working electrode was exposed to the electrolyte. All corrosion experiments were carried out in a naturally aerated 3.5 wt.% NaCl solution as the electrolyte at constant room temperature. Prior to polarization, specimens were immersed in electrolyte solution for 300-seconds. Subsequently, a sweep rate of 30 mV/min was employed, spanning from -100 to 1000 mV in reference to OCP. Monitoring and recording of anodic polarization were carried out using a Solartron ECI 1286 potentiostat connected to a computer equipped with CorrWare software. Before EIS, OCP measurements were carried out by measuring potential between RE and WE without current being transferred to CE to ensure stability in corrosion potential. EIS measurements were made immediately after OCP measurements in the frequency range of 100KHz to 10mHz with a voltage perturbation of 2 mV over 100 measuring points. The current range was 10 mA and acquisition period were 2.0 s. From the obtained electrochemical information, corrosion potential ( $E_{corr}$ ), Corrosion current density ( $i_{corr}$ ) and corrosion rate (mm/y) are determined.

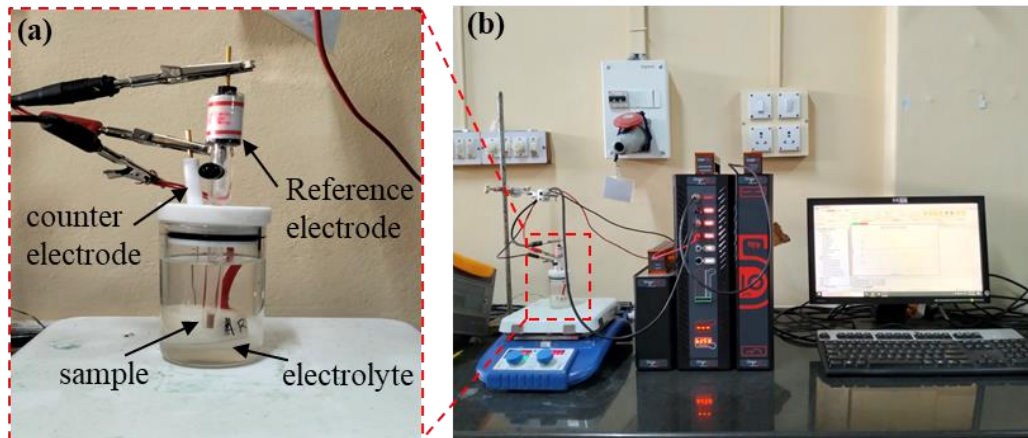


Figure 3.10 (a) Magnified portion of electrochemical setup depicting the three-electrode configuration, and (b) Electrochemical workstation.

### 3.7 Wear studies

To evaluate the wear behavior of AA2050 alloy in different processed conditions, wear tests were conducted using an Anton Paar TRB<sup>3</sup> ball-on-disc reciprocating setup. Produced a sinusoidal velocity profile in accordance with ASTM G133 standards. Figure 3.11(b) illustrates the schematic representation of the ball and disc interface. The setup consisted of a reciprocating sample holder (Al samples) and a pin that held the

counter ball (steel ball). The specimens and the counter ball moved relative to each other in a linear, back and forth sliding motion under a prescribed set of conditions. Load was applied on the pin, and the corresponding load and frictional force were measured and recorded in the system. The counter ball made of 14 Cr steel of diameter 3 mm slides against a flat oxide-free mirror polished aluminum sample. Steel balls with higher hardness and wear resistance than AA2050 Al alloy were chosen to minimize wear and shape change at the counter face and to prevent any change in the contact geometry of the tribo-system. The specimens were securely fastened inside a wear chamber, and the friction and wear tests were conducted at a constant amplitude of 8 mm and a frequency of 2 Hz under varying load conditions of 2, 4, 6, and 10 N for up to 5000 cycles. All tests were carried out in an unlubricated laboratory environment with an average humidity of 60%. Frictional force was quantified using a load-cell attached to the reciprocating pin, while the coefficient of friction was determined by dividing the frictional force by the applied normal load.

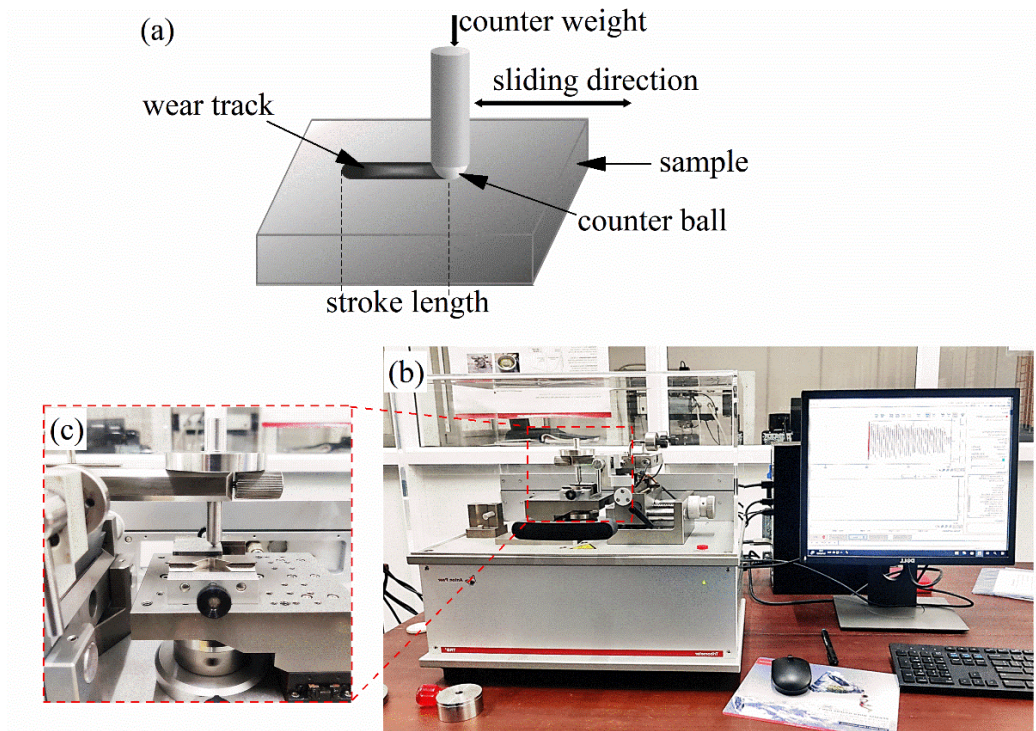


Figure 3.11 (a) Schematic representation of ball-on-disc reciprocating setup, (b) Anton Paar TRB3 ball-on-disc reciprocating setup, and (c) magnified portion depicting sample and the counter ball interface.

## CHAPTER 4

### RESULTS AND DISCUSSION: MICROSTRUCTURE AND MECHANICAL PROPERTIES

This chapter presents detailed results and observations obtained through a series of experiments on microstructural analysis and mechanical characterizations. Results obtained from these characterizations are discussed and their implications are drawn. The findings contribute to an in-depth understanding the performance of AA2050 Al-Cu-Li alloy subjected to MAF and post MAF artificial aging heat treatments. A comparative analysis and comparison with existing literature is also performed, to draw meaningful conclusions and highlight the material's unique attributes.

#### 4.1 Microstructure characterization

In this section, various techniques, used to characterize the microstructure of AA2050 are discussed. This includes optical microscopy, scanning electron microscopy (SEM), transmission electron microscopy (TEM), and X-ray diffraction (XRD). The results of these studies are presented, highlighting the material's grain structure, phase composition, and precipitates formed.

##### 4.1.1 Optical microscopy

This section presents the optical microstructures of AA2050 alloy in different processing conditions. SHT (solution heat treated) samples exhibit elongated/laminar morphology (Figure 4.1(a)). Similar, grain structure in Al<sub>2</sub>Cu-Li alloys was reported by Ye et al. (2022). In MAF processed samples, after 1 cycle, a strain of approximately 0.7 was induces which resulted in the formation of deformation bands as seen in Figure 4.1(b). As the number of MAF passes increases, the density of deformation bands also increases, as observed in the optical micrographs of the 2 cycle MAF processed sample with a cumulative strain of 1.4 (Figure 4.1(c)). Further, Figure 4.1(d) displays the microstructure after 3 cycles of MAF with a cumulative strain of 2.1, showing a large density of deformation bands. Figure 4.1(e) shows the microstructure of 4 pass MAF processed sample, which also confirms the presence of large density of deformation bands. A similar results were reported by Rao et al. during the deformation of AA6061 alloy at liquid nitrogen temperature (Rao et al. 2015). Under the influence of severe

plastic deformation, micro shear bands, and deformation bands form, with the number and misorientation of bands increasing with the number of forging passes, resulting in fine equiaxed type substructure/grains (Gupta et al. 2016). From the optical microscopy observations, it is shown that, MAF processing has resulted in formation of deformation bands and the density of deformations further increases with increase in number of MAF passes.

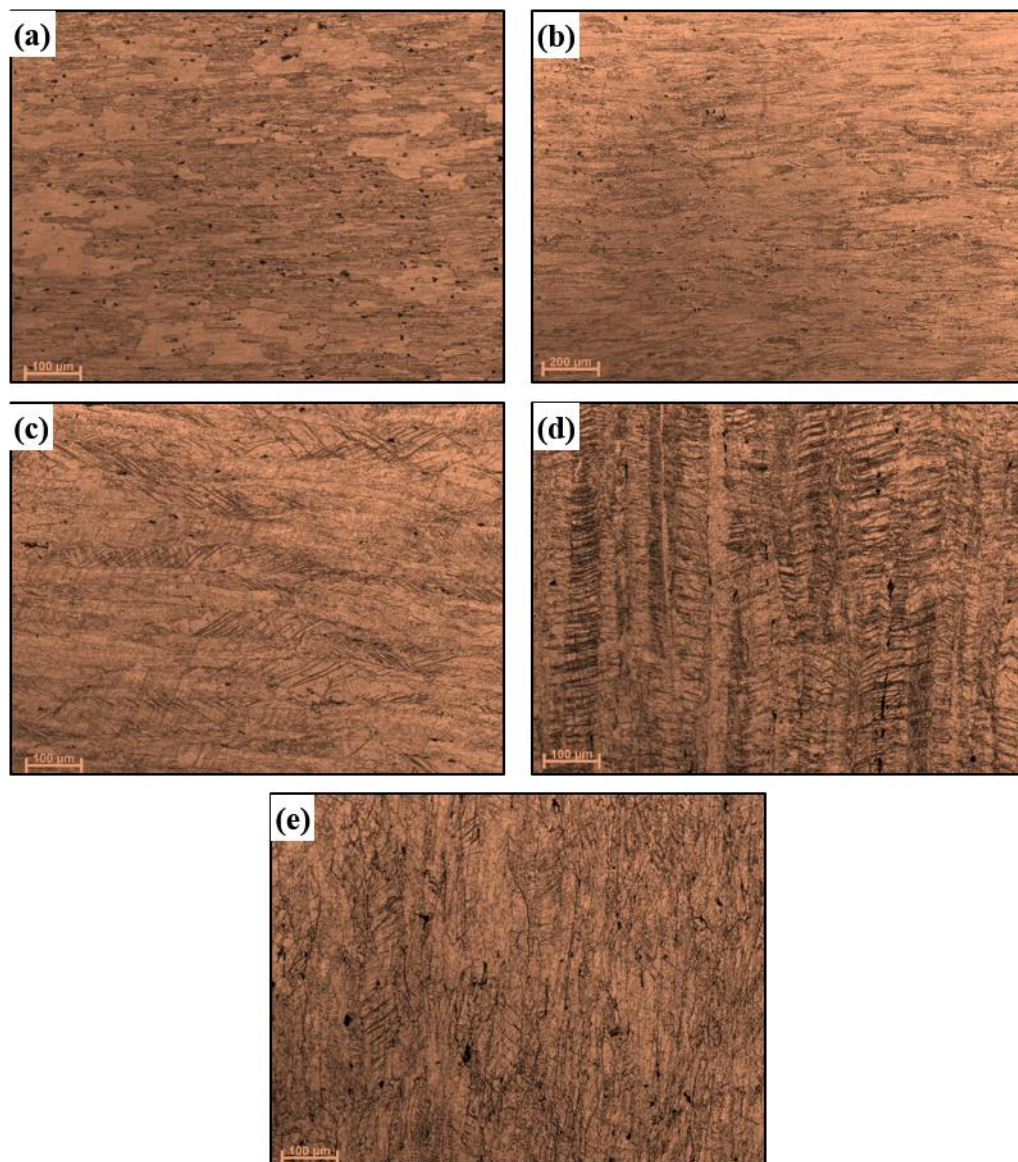


Figure 4.1 Optical micrographs of AA2050 Al-Cu-Li alloy in different processed conditions of (a) SHT, and (b) 3 pass, (c) 6 pass, (d) 9 pass, (e) 12 pass MAF processed conditions.

Figure 4.2 presents the microstructure of SHT and 6, 12 pass MAF processed samples subjected to artificial peak aged at 155 °C. SHT + peak aged samples, as seen in Figure 4.2(a), shows similar characteristics of un-aged SHT sample, similar to Figure 4.1(a), with elongated/laminar morphology. Figure 4.2(b) and (c) show the microstructures of 6 and 12 pass MAF samples after peak aged condition, which consist of large amount of deformation bands induced during MAF processing. From the microstructural observations, it is evident that, aging has no effect on grain structure modification. Either change in shape and size has occurred due to recrystallization, or the reduction in deformation bands. This is probably due to the low aging temperature that could not drive grain structure modification.

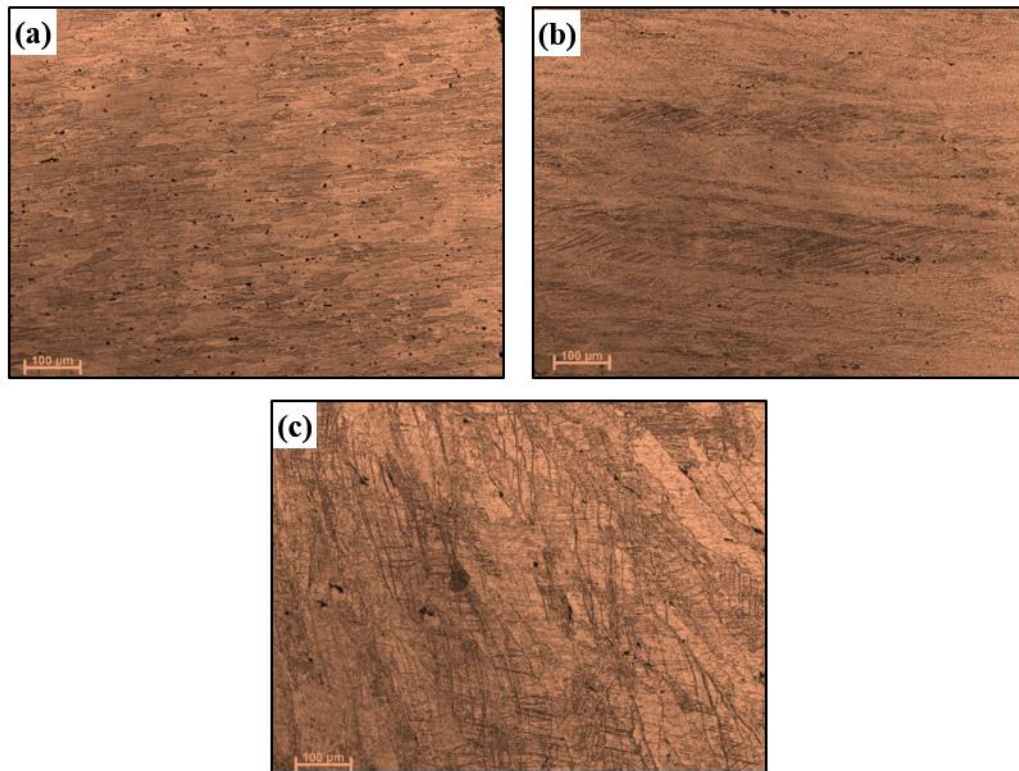


Figure 4.2 Optical micrographs of AA2050 Al-Cu-Li alloy in (a) SHT + peak aged, (b) 6 pass + peak aged, and (c) 12 pass + peak aged sample conditions.

#### 4.1.2 Electron Back Scattered Diffraction

Image quality maps and inverse pole figure maps obtained by EBSD analysis of SHT, MAF processed and post MAF peak aged samples are presented in this section. Image quality map is superimposed with orientation image micrographs (OIM) to extract high angle grain boundaries (HAGB) and low angle grain boundaries (LAGB). The grain

boundaries with misorientation angle  $\theta \geq 15^\circ$  are characterized as high angle grain boundaries (HAGB) and grain boundaries with misorientation angle  $\theta < 15^\circ$  are characterized as low angle grain boundaries (LAGB). Inserts represents inverse pole figure (IPF) maps of the crystallographic directions of the grains those are parallel to previous forging axis. OIM of SHT revealed the presence of elongated coarse grains (CGs) with larger fraction of HAGBs (Figure 4.3).

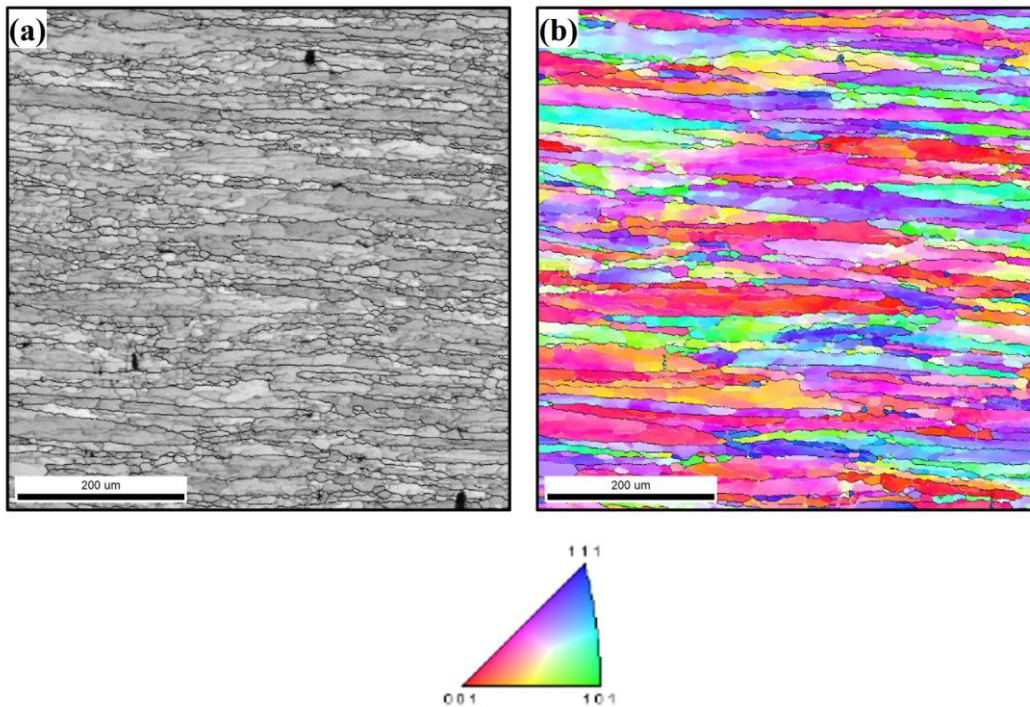


Figure 4.3 Image quality and IPF maps of AA2050 alloy in SHT sample condition.

Figure 4.4 refers to 6 pass MAF processed sample, where initial grains are fragmented by shear bands and/or deformation bands. Formation of large density of deformation bands, due to the influence of large plastic strains, is evident. Further, with increase in cumulative strain after every pass of MAF process, increase in misorientation angles, from sub-boundaries to HAGBs, were observed in Figure 4.5, at region-1 in 12 pass sample. Width of the sub-grains formed by fragmentation of coarse grains are observed to be approximately  $10 \mu\text{m}$ . Careful examination of the microstructures of 12 pass sample indicated as region 2 in Figure 4.5 reveals the presence of new fine grains with diameter of few microns. Occurrence of continuous dynamic recrystallization at higher cumulative strains promotes new UFGs due to restoration and recovery (Sakai et al. 2014).

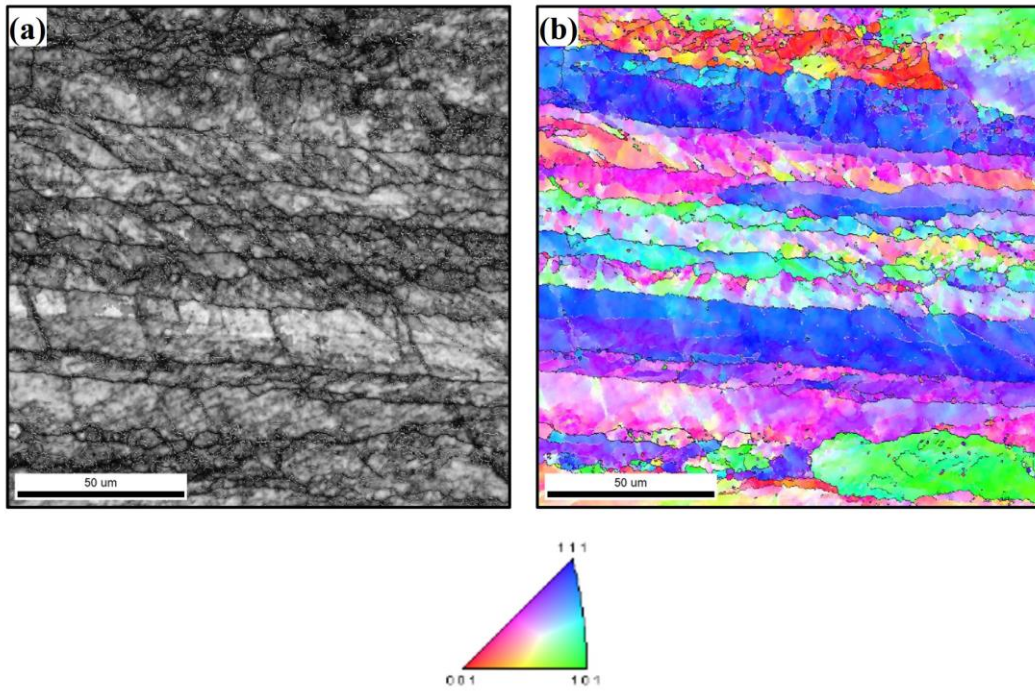


Figure 4.4 Image quality and IPF maps of AA2050 alloy after 6 pass MAF processed condition.

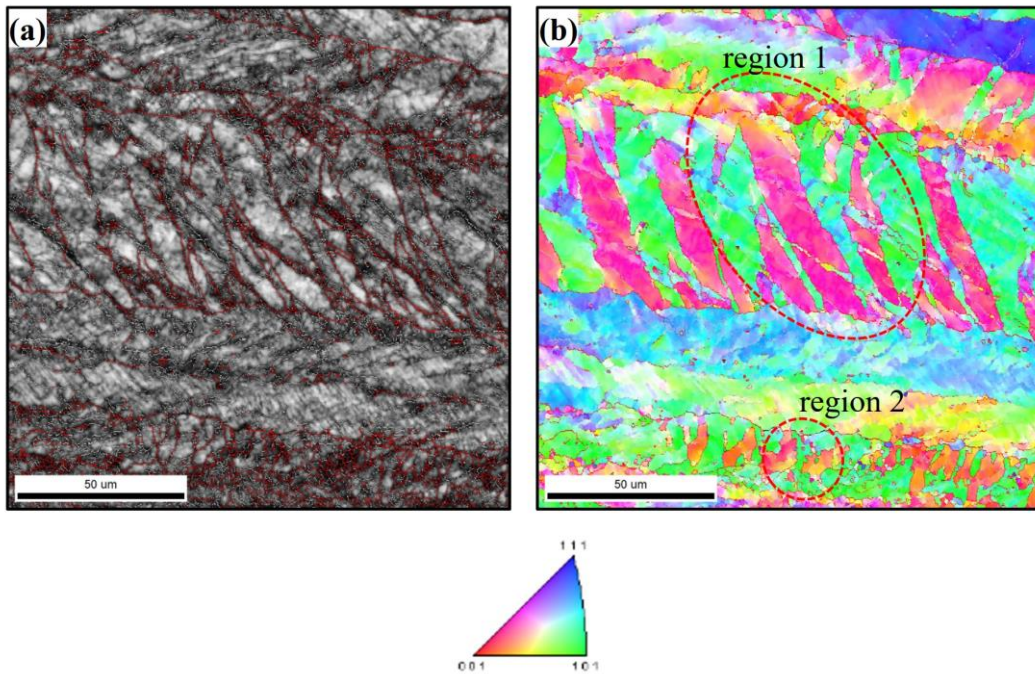


Figure 4.5 Image quality and IPF maps of AA2050 alloy after 12 pass MAF processed condition.

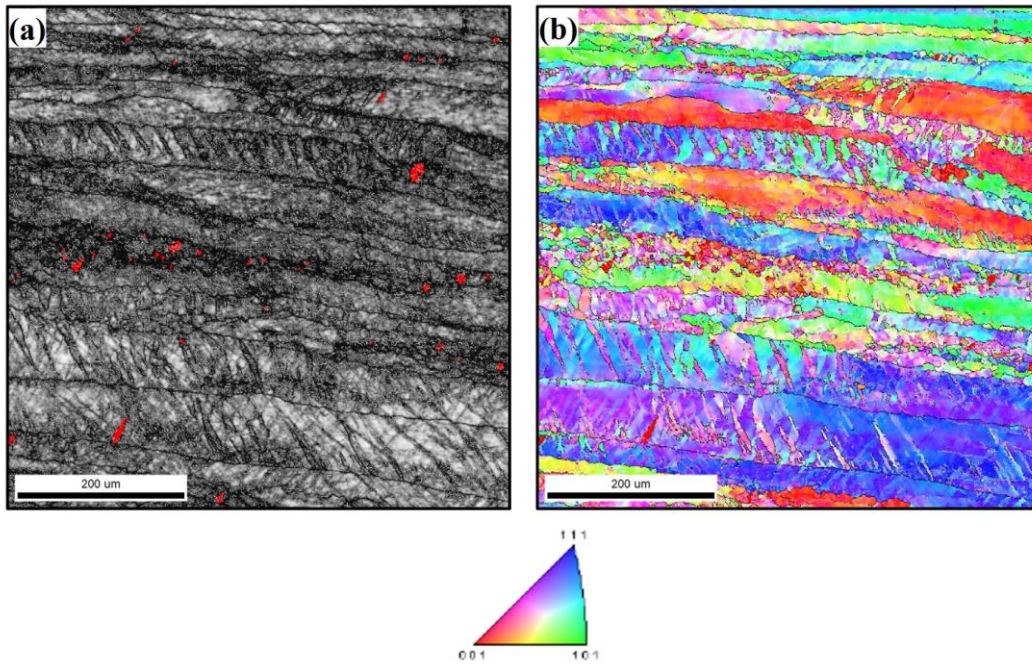


Figure 4.6 Image quality and IPF maps of AA2050 alloy after 6 pass MAF processed and peak aged condition.

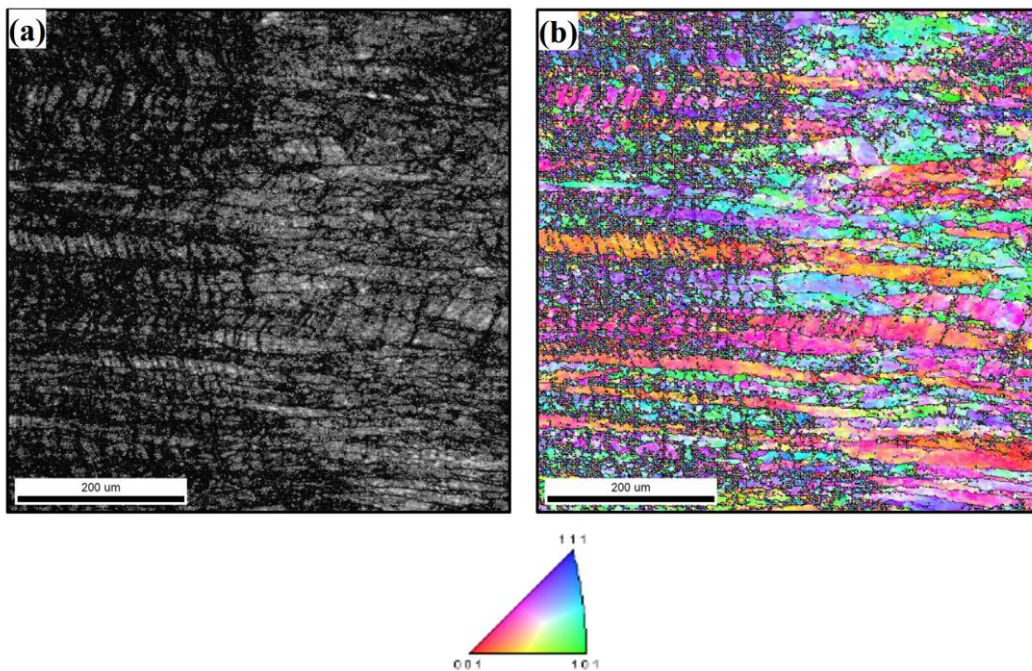


Figure 4.7 Image quality and IPF maps of AA2050 alloy after 12 pass MAF processed and peak aged condition.

Various researchers have reported the formation of UFG at cross overs of micro shear bands at higher strains (Hurley and Humphreys 2003; Sitdikov et al. 2006). Thus, overall microstructure, developed in 12 pass sample, is the combination of sub-grains,

formed by transformation of deformation bands and UFGs due to dynamic recrystallization. Peak aged 6 and 12 pass samples processed at 155 °C is shown in Figure 4.6 and Figure 4.7, respectively, represent similar microstructure in comparison with un-aged counterparts indicating no further recrystallization or microstructural changes, during ageing. Overall observation of OIMs of all processed conditions does not show any preferred orientation of crystallographic planes.

#### **4.1.2.1 Grain size distribution**

Figure 4.8 represents grain size distribution of samples under various processing conditions and are to be bi-modal distribution. Grains having size less than or equals to 20  $\mu\text{m}$  are considered to be fine and greater than 20  $\mu\text{m}$ , as coarse grains. Variation of grain size for various processing conditions are shown in Figure 4.8(f). SHT sample shows large fraction of coarse/larger grains (approx. 86%) and fewer smaller/fine grains, with average grain size of  $74.3 \pm 12$  microns.

MAF processing has shown reduction in average grain size from  $38.81 \pm 8$  to  $22.1 \pm 2.8$   $\mu\text{m}$  from 6<sup>th</sup> pass to 12<sup>th</sup> pass samples, respectively. Figure 4.8(f). shows the fraction of fine grains, which increased from ~14% (SHT) to ~31% in 6 pass and ~70% in 12 pass samples, indicating the formation of fine grains, upon MAF processing. Average grain size of  $40.12 \pm 2$  and  $17 \pm 2$   $\mu\text{m}$  are observed for peak aged conditions on 6<sup>th</sup> and 12<sup>th</sup> pass MAF processed samples.

#### **4.1.2.2 Misorientation angle and Grain boundary character distribution (GBCD)**

GBCD plots obtained by considering the individual number fraction of LAGBs and HAGBs and misorientation angle distribution plots for samples processed at different conditions are shown in Figure 4.9. SHT samples have high fraction (0.8) of HAGBs due to presence of recrystallized grains, with misorientations distributed over wide range (Figure 4.9(a)). After 6 pass of MAF, considerable increase in LAGBs with decrease in HAGBs, was observed, and average misorientation shifts to lower angle (Figure 4.9(b-c)), due to formation of deformation bands and subsequent transformation into sub grains. 6 to 12 pass samples of MAF shows mild increase in HAGBs, which is contrast with SHT to 6 pass samples due to presence of sub grains and recrystallized grains (Jazaeri and Humphreys 2004; Kapoor et al. 2020). From Figure 4.9(a,e,f), post-

MAF peak aged samples shows similar misorientation characteristics, as ageing was carried out below MAF processing temperature.

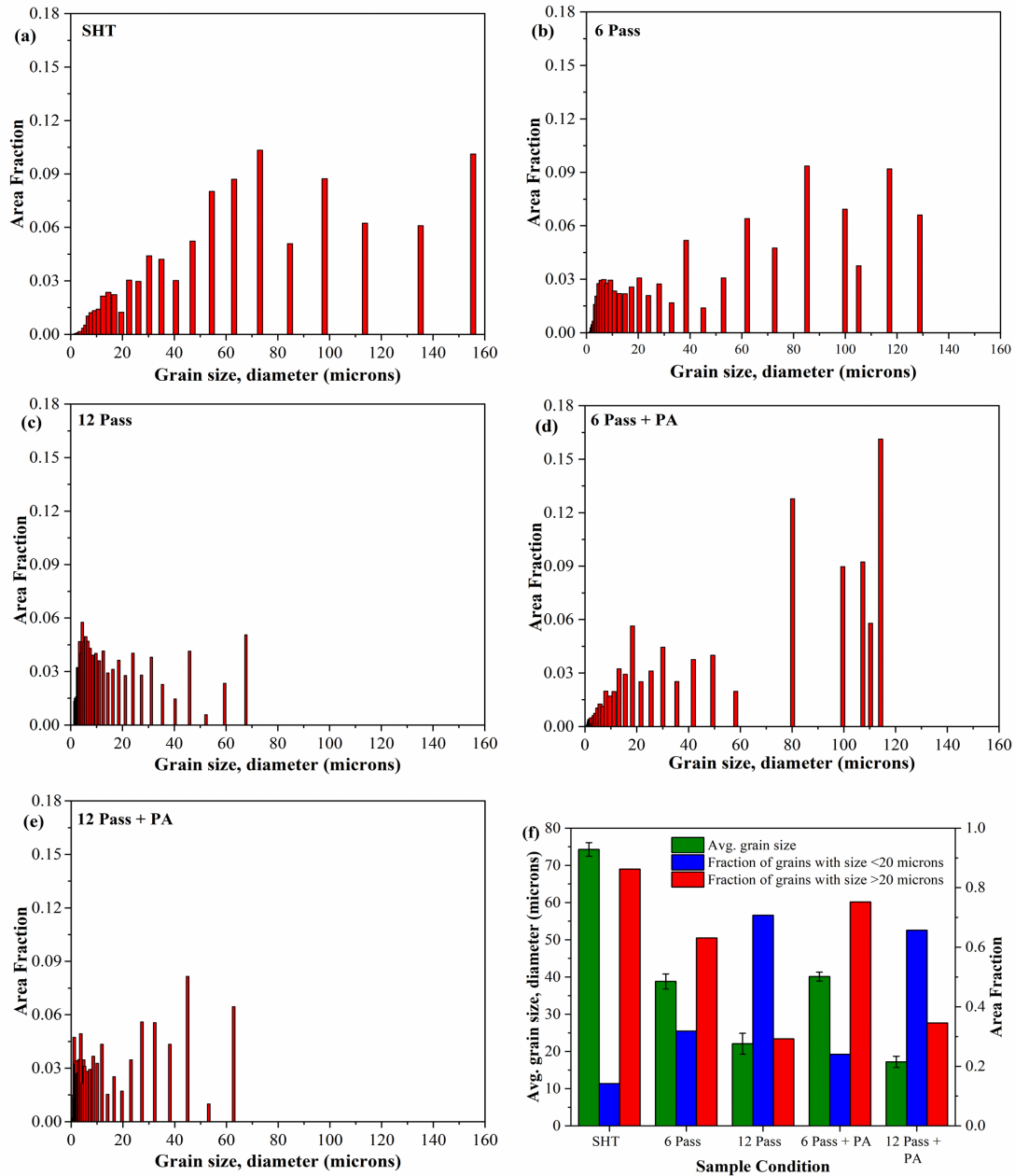


Figure 4.8 (a-e) Grain size distribution plots for SHT, 6 and 12 pass MAF processed, and peak aged samples of SHT, 6 and 12 pass MAF processed, (f) variation of grain size distribution in various processed conditions.

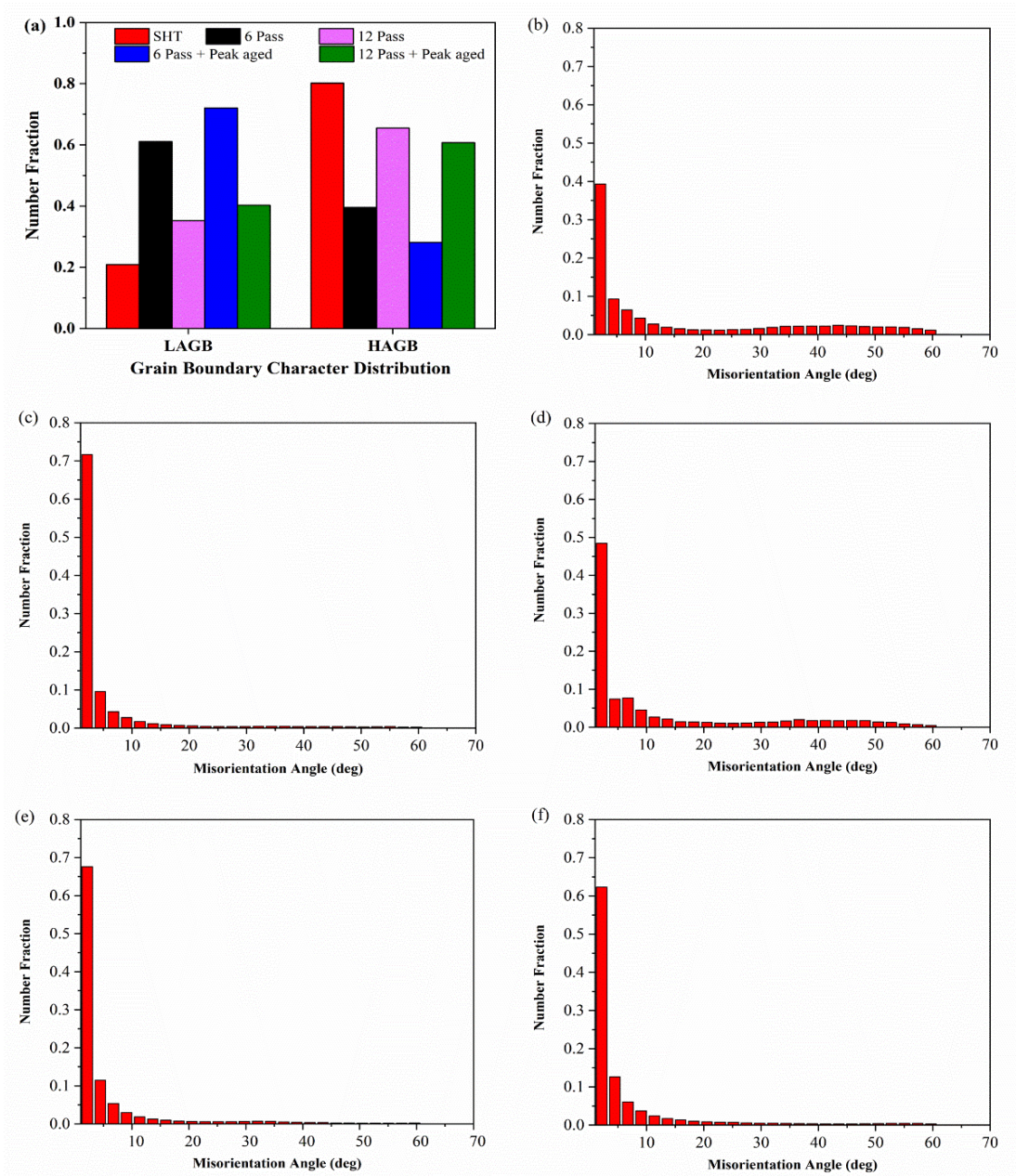


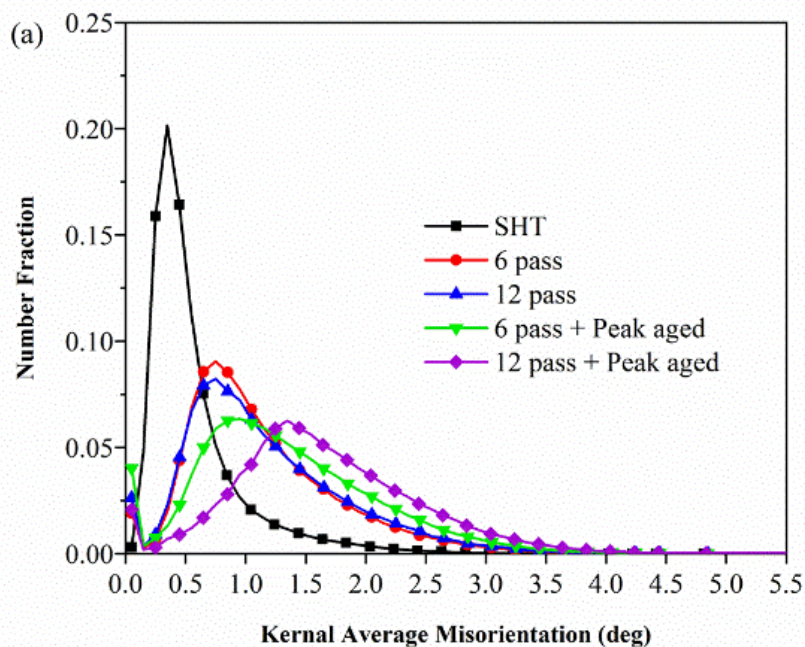
Figure 4.9 (a) Grain boundary character distribution, and Misorientation angle distribution for (b) SHT, (c) 6 pass, (d) 12 pass, (e) 6 pass + peak aged, (f) 12 pass + peak aged sample conditions.

#### 4.1.2.3 Kernel average misorientation (KAM) and grain orientation spread (GOS)

Intra-grain misorientation parameters such as KAM and GOS obtained from EBSD data, to estimate the strain accumulation within and across the grains for various processing conditions, is shown in Figure 4.10. KAM is an average misorientation at

the centre of kernel, calculated by considering the average of local misorientations between the centre and points on perimeter of kernel and excluding the misorientation greater than  $5^\circ$  (Suresh et al. 2018). Similarly, GOS is calculated by taking average of misorientations, determined by measuring the misorientation angle between each measuring point and overall average misorientation angle of grain (Suresh et al. 2019; Wright et al. 2011).

Higher fractions have been observed at low angles of KAM for SHT Sample, which indicate less strain within the grain and large fraction of recrystallized grains (Suresh et al. 2013) and is reflected in Figure 4.10(a). In Figure 4.10(b), GOS value of SHT samples are observed at low angles, specifies the low dislocation content and strain free grains. From Figure 4.10 for MAF processed 6 pass sample, KAM and GOS peaks are slightly ahead of SHT peaks, ensuring higher dislocation content. 12 pass samples showed similar characteristics as that of 6<sup>th</sup> pass sample, with slight decrease in average KAM and GOS, as at higher strains, due to dynamic recrystallization (Ikeda et al. 2019; Suresh et al. 2013).



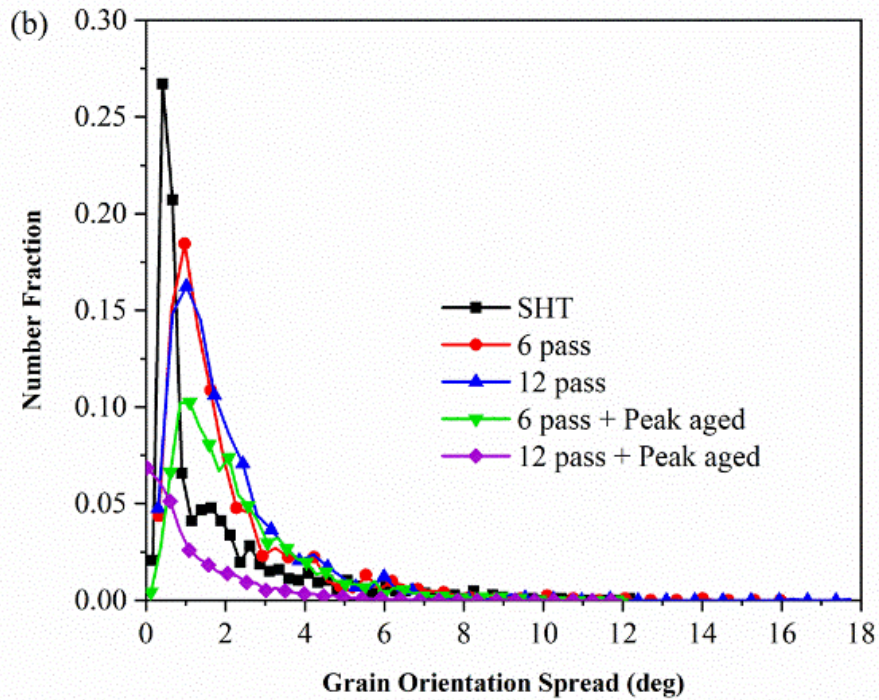


Figure 4.10 EBSD generated (a) kernel average misorientation (KAM) and (b) grain orientation spread (GOS) for various processed conditions.

### 4.1.3 Transmission Electron microscopy

Samples at different processing conditions such as SHT, 6 and 12 pass MAF processed, and peaked aged 6 and 12 pass MAF processed samples are subjected to TEM studies. The studies provide useful information on grain structure modification, formation of various precipitates and phases during MAF processing and post MAF artificial aging.

#### 4.1.3.1 Effect of MAF on microstructures

Bright-field TEM micrographs and selected area electron diffraction (SAED) pattern of SHT sample is shown in the Figure. 4.11(a,d). Microstructure appears to be free from strain with no indication of dislocation clusters and the corresponding SAED patterns display periodically arranged clear spots indexed to various Al lattice planes. Furthermore, SAED patterns do not show any major spots or streaks in between Al matrix spots, corresponding to secondary phases. This indicates the complete dissolution of secondary phases into Al matrix, leading to the formation of supersaturated solid solution, during solution heat treatment (Dhal et al. 2015).

Microstructure of 6 and 12 pass samples are characterized by high density of dislocation forests, revealing the formation of highly strained grains, as seen in Figure. 4.11(b,c). Additionally, 12 pass sample exhibits fine grains that are predominantly surrounded by large dislocation clusters. From Figure. 4.11(b,c) it is also evident that significant number of deformation bands were formed upon MAF. There was no traces of precipitates along the grain boundaries or grain interiors. SAED patterns display less wider (narrow) ring-like patterns for the 6 and 12 pass samples (Figure. 4.11(e,f)), indicating the formation of fine and deformed grains with no spots or streaks corresponding to precipitates. Murayama et al. reported similar dissolution of precipitates during equal channel angular pressing of Al-Cu alloy (Murayama et al. 2001).

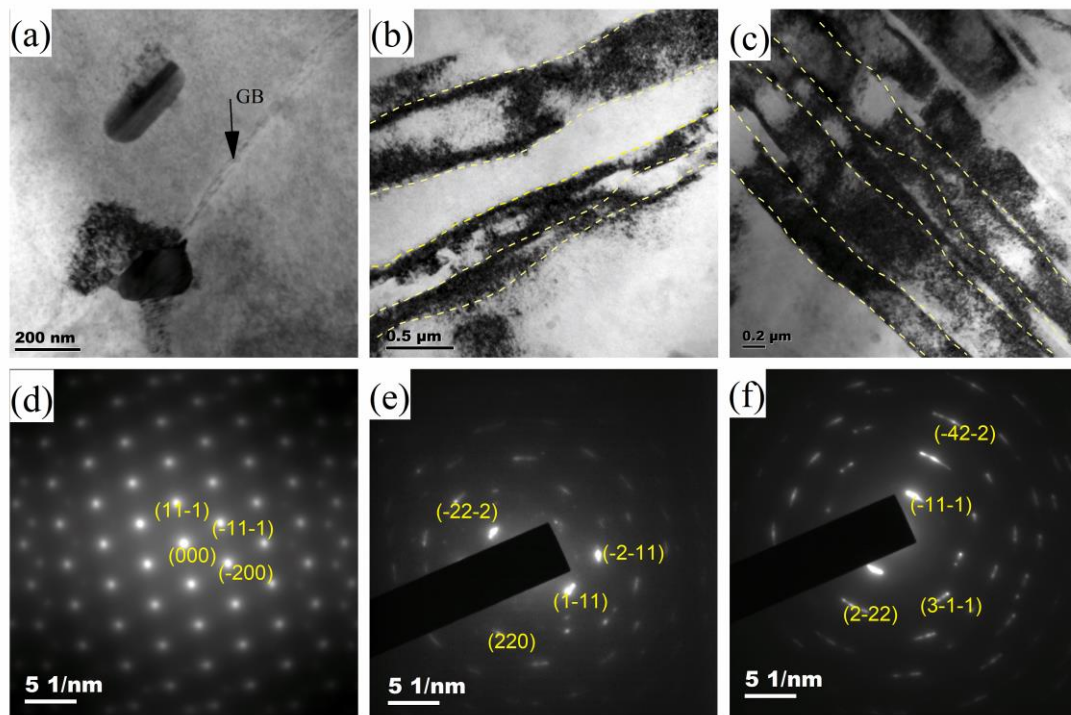


Figure. 4.11 TEM micrographs of AA2050 alloy in different processed conditions: Bright field image and SAED pattern of (a,d) SHT sample, (b,e) 6 pass MAF processed sample, and (c,f) 12 pass MAF processed sample.

#### 4.1.3.2 Effect of artificial aging heat treatment on microstructures

The effect of peak aging on microstructure and precipitation behavior of AA2050 Al-Cu-Li alloy was investigated for specimens subjected to SHT, 6 pass, and 12 pass MAF processing. Aging of Al-Cu-Li alloys resulted in evolution of various precipitates,

depending on the initial processed conditions and aging parameters. Based upon the previous studies, to identify the complex precipitates evolved, schematic representation of the typical diffraction spots and streaks of SAED patterns, is provided in Figure 4.12. This schematic depicts major precipitates ( $T_1$ ,  $\theta'$ ,  $\delta'/\beta'$ ) observed in 3<sup>rd</sup> generation Al-Cu-Li alloys in their main zone axes. Bright field transmission electron micrograph of the SHT and peak-aged samples revealed strain-free grains with continuous intergranular phases at the grain boundaries (GBs), as depicted in Figure 4.13(a). Typically, in polycrystalline materials, GBs serve as heterogeneous nucleation sites for secondary phases/precipitates due to the high density of dislocations and vacancies. In Al-Cu-Li alloys, Cu atoms diffuse into GBs, leading to the precipitation of continuous Cu-rich phases. Moreover, the grain interiors exhibit substantial precipitation of rod-like  $T_1$  phases as shown in Figure 4.13(b). SAED patterns of SHT + peak aged sample confirms the formation of  $T_1$  precipitates upon aging. Excessive precipitation of Cu-rich phases at GBs and grain interiors causes Cu depletion regions, resulting in the formation of precipitate-free zones (PFZ) adjacent to GBs, as evident in Figure 4.13(a). Bright field TEM images of 6 pass and 12 pass peak-aged samples, that exhibit dislocation cells resulting from large strains induced during MAF processing, are shown in Figure 4.13(d,g). As depicted in Figure 4.13(e,h), peak-aged 6 pass and 12 pass samples exhibit high density of fine, rod-shaped  $T_1$  precipitates within the grain interiors. In Al-Cu-Li alloys, crystallographic defects such as dislocations, vacancies, and GBs act as preferential nucleation sites for  $T_1$  precipitates. Large dislocations induced during the MAF serve as the diffusion paths for solute atoms to nucleate  $T_1$  phases. Thus, denser  $T_1$  phases nucleate and grow within grain interiors in MAF processed and peak-aged samples compared to conventionally aged samples. The substantial precipitation of  $T_1$  phases inside the grain interiors after peak aging leads to Cu depletion in the matrix. Additionally, the large dislocations pileup caused by MAF impedes the diffusion of Cu atoms towards GBs, thus hindering GB precipitation.

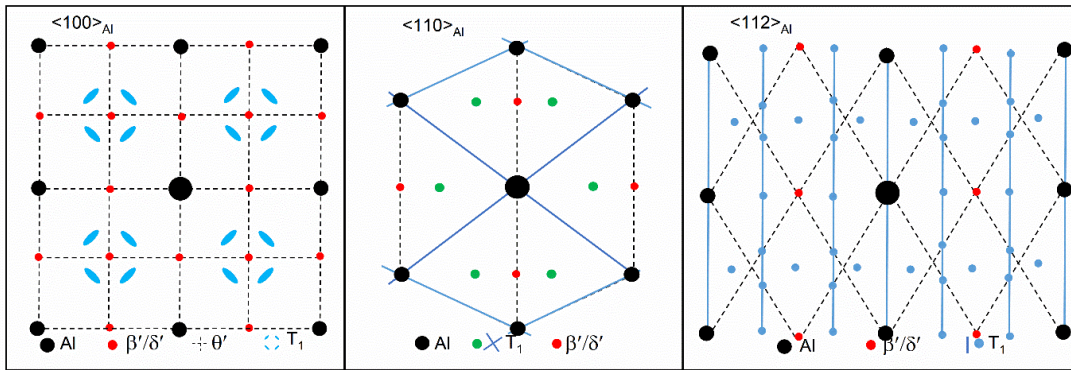


Figure 4.12 Schematic SAED pattern representation of spots and streaks corresponding to various precipitates observed in Al-Cu-Li alloys.

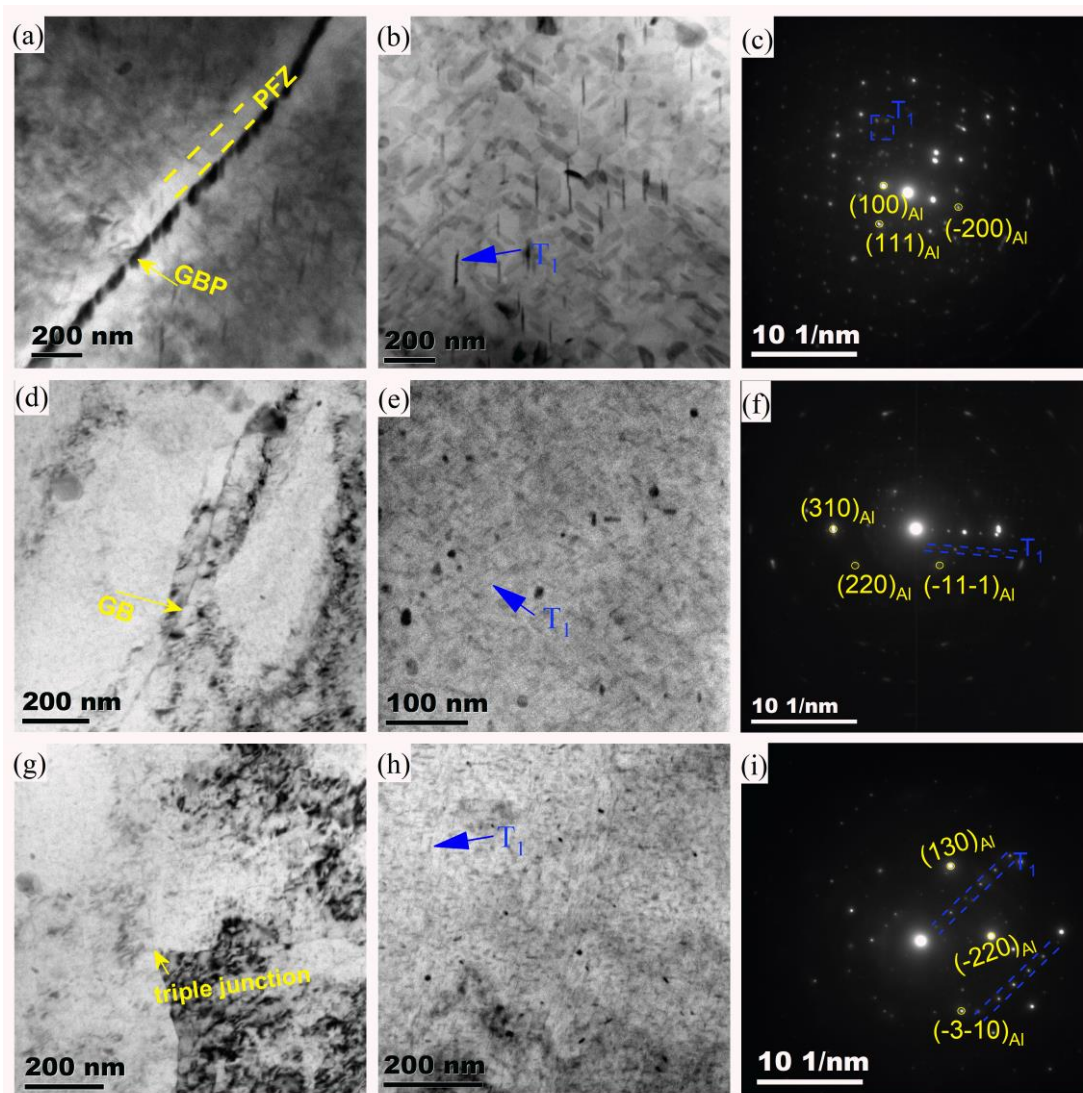


Figure 4.13 TEM micrographs of AA2050 alloy in different processed conditions: Bright field image and SAED pattern of (a,d) SHT sample, (b,e) 6 pass MAF processed sample, and (c,f) 12 pass MAF processed sample.

#### 4.1.4 X-Ray Diffraction

XRD patterns extracted for SHT, MAF processed, and post MAF peak aged samples are shown in Figure 4.14. All phases identified through XRD belong to face-centered cubic (FCC) system and peaks corresponding to Al, of all processing conditions, are indexed to (111), (220), (322), (432) and (640) hkl lattice planes. From Figure 4.14(a), variations in peak intensities are observed upon MAF processing, resulting from the formation of subgrains, change in the crystal orientations, and fine grains. Further, for more insight, peak analysis of Al (111) plane occurring at  $2\theta$  of  $38.5^\circ$  for SHT and MAF processed samples are presented in Figure 4.14(b). Shifting of peaks towards the left (lower  $2\theta$  angle) was observed, due to the accumulation of strains with MAF passes (Ramesh et al. 2019; Vigneshwaran et al. 2019). Further, width of the peaks was observed to be broadened with increase in the number of MAF passes as an effect of reduction in crystallite size, work hardening, and residual stresses (Dutta and Pradhan 2003; Vigneshwaran et al. 2019). Figure 4.14(a) also represents XRD patterns at peak aged conditions of SHT, 6<sup>th</sup>, and 12<sup>th</sup> pass MAF processed samples subjected to artificial aging heat treatment at  $155^\circ\text{C}$ . Analysis of peaks showed small intensities of peaks corresponding to  $\text{Al}_3\text{Li}$ ,  $\text{Al}_2\text{CuLi}$ , and  $\text{Al}_2\text{Cu}$  precipitates, confirming the formation of secondary particles upon artificial aging. Less change in peak intensities are observed, in comparison with their corresponding un-aged counterparts, indicating no significant changes occurred in crystal orientations during artificial aging.

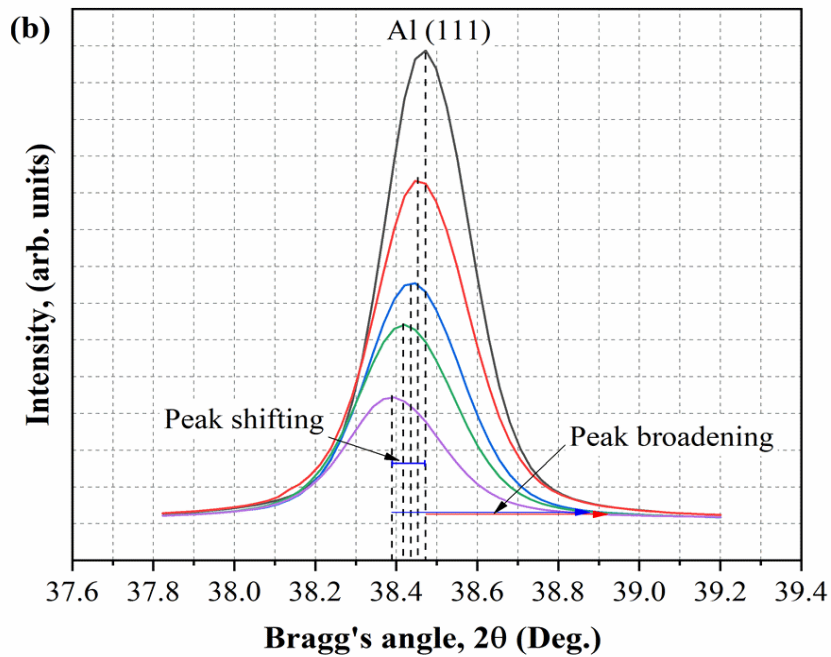
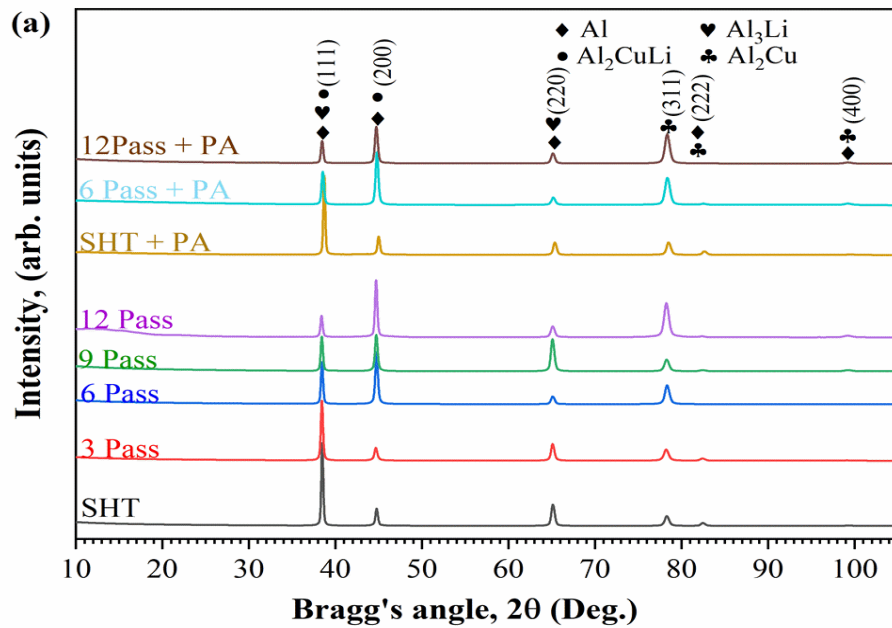


Figure 4.14 (a) X-Ray diffraction patterns, (b) analysis of X-ray diffraction peaks corresponding to (111) lattice plane of AA2050 Al-Cu-Li alloy for various processed condition.

#### 4.1.5 XRD Macro texture analysis

XRD Macro texture measurements were conducted to determine the macro texture evolution during MAF processing of AA2050 alloy and post MAF peak aging. A well-

defined and commonly used Schulz method is adopted for XRD texture measurement the procedure for the same is briefed in chapter 3. In Schulz method of XRD measurements, background intensities vary with increase in tilt angle, thus background error creeps in (Decker et al. 2004). To overcome the effect of background intensities on actual peak intensities, background corrections are made by measuring the background intensities separately along the  $2\theta$  angle and integrating it with respect to  $\phi$ . Thus, the corrected pole figure intensity is obtained from the following equation (Suwas and Ray 2014).

$$I_{corrected} = I_{measured}(\phi, \varphi) - I_{background}(\phi) \quad \text{Equation 4.1}$$

Where,  $I_{corrected}$  is the corrected pole figure intensity,  $I_{measured}(\phi, \varphi)$  is the experimentally measured intensity and  $I_{background}(\phi)$  is the background intensity measured separately.

Figure 4.15 illustrates the general representation of complete pole figures, depicting observed texture components in FCC materials in (111), (200) and (220) hkl planes respectively. As evident in Figure 4.16(a), SHT samples showed strong cube and Goss texture. Figure 4.16(b,c) depicts the pole figures of 6 pass and 12 pass MAF processed samples, after SHT for (111), (200) and (220) hkl planes, respectively. It is noticeable that, there is a substantial difference in texture characteristics between SHT and MAF processed samples. Samples, that were subjected to 6 pass MAF processing, exhibited a strong S and Gross texture. Furthermore, MAF processing up to 12 passes resulted in strengthening of Gross texture component. This change in texture characteristics is primarily due to the change in the reference plane of deformation between each individual passes during MAF. Similar texture modifications were reported by (Nayan et al. 2019) in samples subjected to crossed rolling, which involved rotation of the deformation direction along the normal direction.

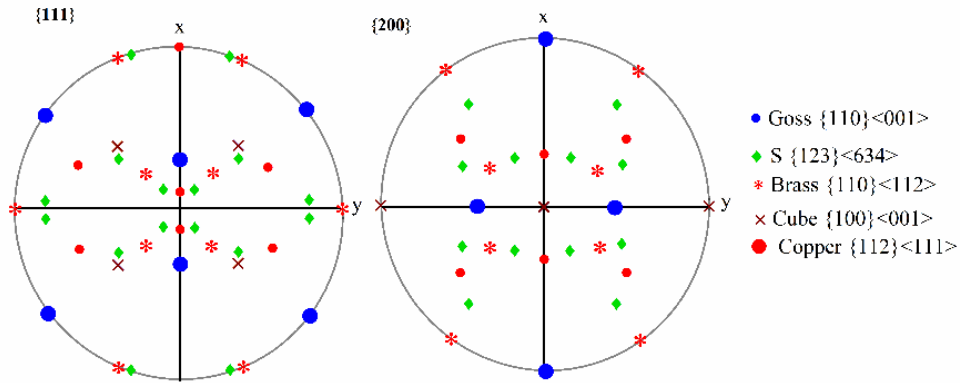


Figure 4.15 Schematic representation of typical orientation and ideal texture components of a FCC material in  $\{111\}$  and  $\{200\}$  pole figures.

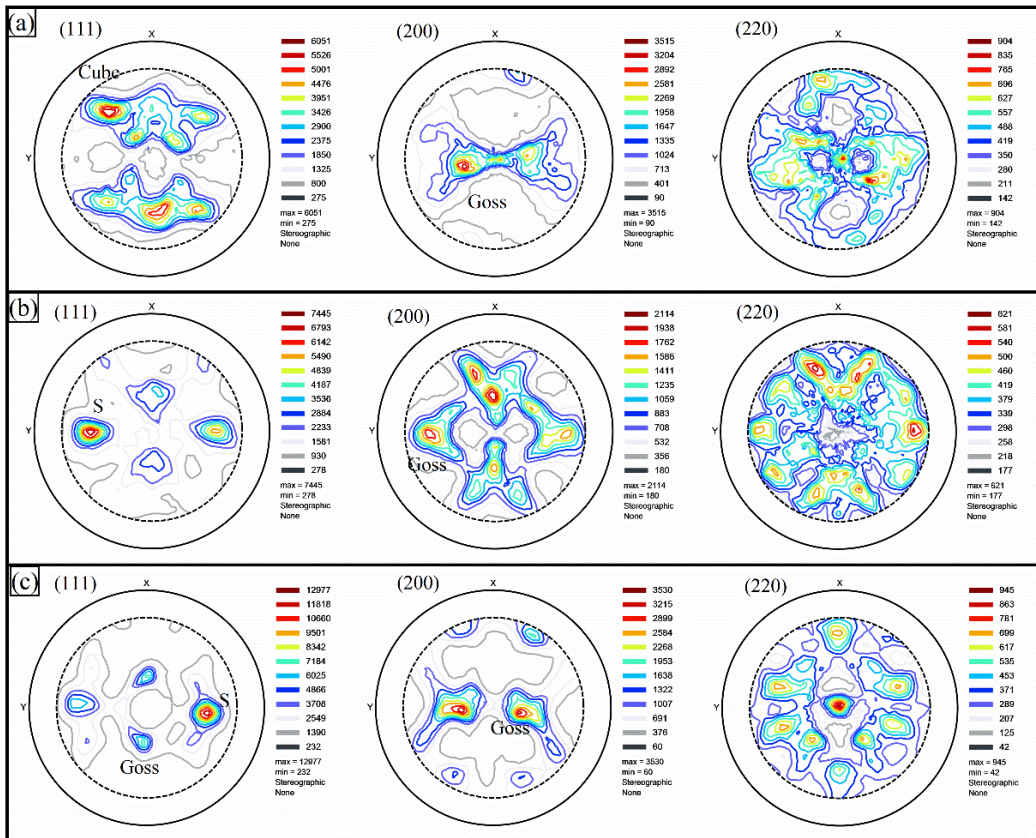


Figure 4.16  $\{111\}$ ,  $\{200\}$  and  $\{220\}$  pole figures of AA2050 alloy in different processed conditions: (a) SHT, (b) 6 pass, and (c) 12 pass MAF processed.

Figure 4.17 depicts the pole figures at peak-aged (155 °C) conditions of SHT, 6 pass, and 12 pass MAF processed samples for (111), (200) and (220) hkl planes, respectively. Texture characteristics of SHT + peak-aged samples display slight variations compared

to un-aged sample conditions, as observed in Figure 4.17(a). Furthermore, Figure 4.17(b,c), which depict pole figures of peak-aged 6 pass and 12 pass MAF samples, do not exhibit any significant changes in texture characteristics, either in terms of texture intensities or texture components. This is due to the low aging temperature, which does not promote recrystallization of the alloy, resulting in minimal microstructural modification.

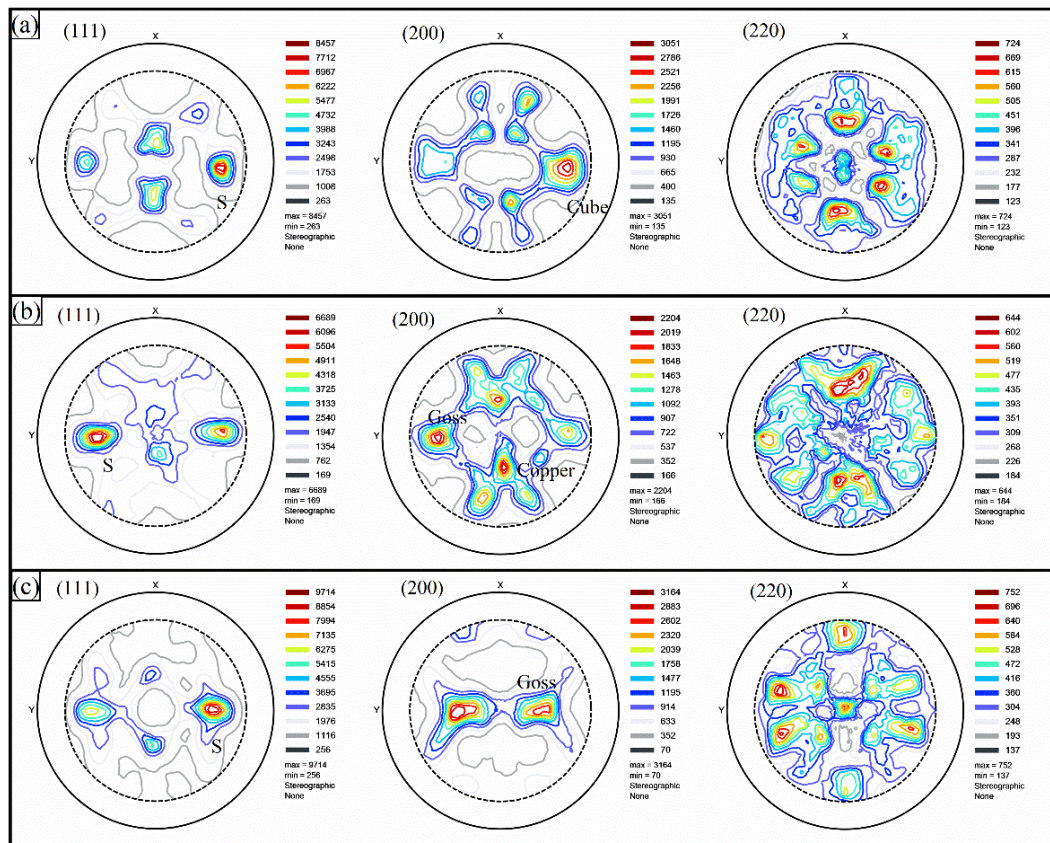


Figure 4.17  $\{111\}$ ,  $\{200\}$  and  $\{220\}$  pole figures of the AA2050 alloy in different processed conditions: (a) SHT + PA, (b) 6 pass + PA, and (c) 12 pass + PA.

## 4.2 Mechanical behavior of AA2050 Al-Cu-Li alloy

Another objective of this study is to enhance the mechanical behavior of the lightweight AA2050 alloy through MAF and post-MAF aging treatments. As discussed in chapter 2, MAF is a process in which the material is deformed along multiple directions, causing changes in the material's properties, such as hardness and tensile properties, due to the introduction of dislocations. Resistance to deformation increases as dislocations, act as crystal defects. In this regard, tensile studies and micro-hardness

tests were conducted to understand the influence of MAF and post-MAF aging on the mechanical properties of the AA2050 alloy. The study first examined the effect of MAF on the alloy by conducting micro-hardness and tensile tests on SHT and SHT+MAF processed samples. Based on the results of tensile and hardness studies, 6 pass and 12 pass MAF samples were selected for further aging heat treatments and compared with non-MAF processed (SHT) samples.

As highlighted in the literature review in chapter 2, aging temperature has a significant impact on material properties. Therefore, to determine the optimal aging temperature, several sets of 6 pass, 12 pass, and SHT samples were aged at 150, 175, and 200 °C, and their corresponding micro hardness was measured at selected time intervals. Based on the micro hardness results, optimal aging temperature, peak-aged, and over-aged conditions were determined. Furthermore, tensile tests were conducted on peak-aged samples that were aged at the optimized aging temperature, for all sample processing conditions to understand the influence of the MAF process on aging behaviors. This study helped in determining the optimal MAF conditions and aging parameters for enhanced material properties, taking into account that SPD processes have a trade-off between mechanical properties in terms of strength and ductility.

#### **4.2.1 Microhardness characterization**

Vickers micro hardness measurements are widely used to determine the hardness of materials by determining the resistance to indentation. This section explains the influence of MAF processing and post MAF aging heat treatment on Vicker's microhardness of the alloy AA2050.

##### **4.2.1.1 Effect of MAF processing on microhardness**

Al alloy AA2050 were processed by MAF to study the influence of MAF on mechanical properties and hardness. Vickers microhardness tests were performed for different MAF processed samples and are presented in Figure 4.18. The outcomes indicate that the solution heat treated (SHT) samples condition displayed minimum hardness of approximately 80 HV. This result is predictable because the age hardenable Al alloys in its SHT state does not contain any strengthening precipitates and the samples are unprocessed.

With MAF, notable enhancement in hardness was apparent. However, an abrupt increase in hardness was detected up to 6 pass of MAF, exhibiting 50% from SHT (80 HV) to 3 pass (120 HV) and 19% from 3 pass to 6 pass (143 HV). The dramatic increase in hardness noted in the initial stages of MAF is attributed to the higher rate of strain hardening. In the initial passes, the induced strain results in the accumulation of larger dislocations in the material, causing it to become significantly harder. Further, from 6 pass to 12 passes of MAF, a minimal increase in hardness (8%) has been observed. This phenomenon occurs because, with the increase in number of MAF passes, the accumulation of dislocations reduces. Thus, fewer dislocations are introduced into the material, leading to a minimal increase in hardness. Furthermore, since the material is already in a hardened state, it becomes more challenging to introduce new dislocations, resulting in decrease in rate of increase in hardness. These results are consistent with the previous findings reported in the literature (Kim et al. 2019; Kotan et al. 2013), thereby demonstrating that Vickers micro hardness measurements are a dependable method to determine the hardness of Al alloy AA2050 after MAF processing.

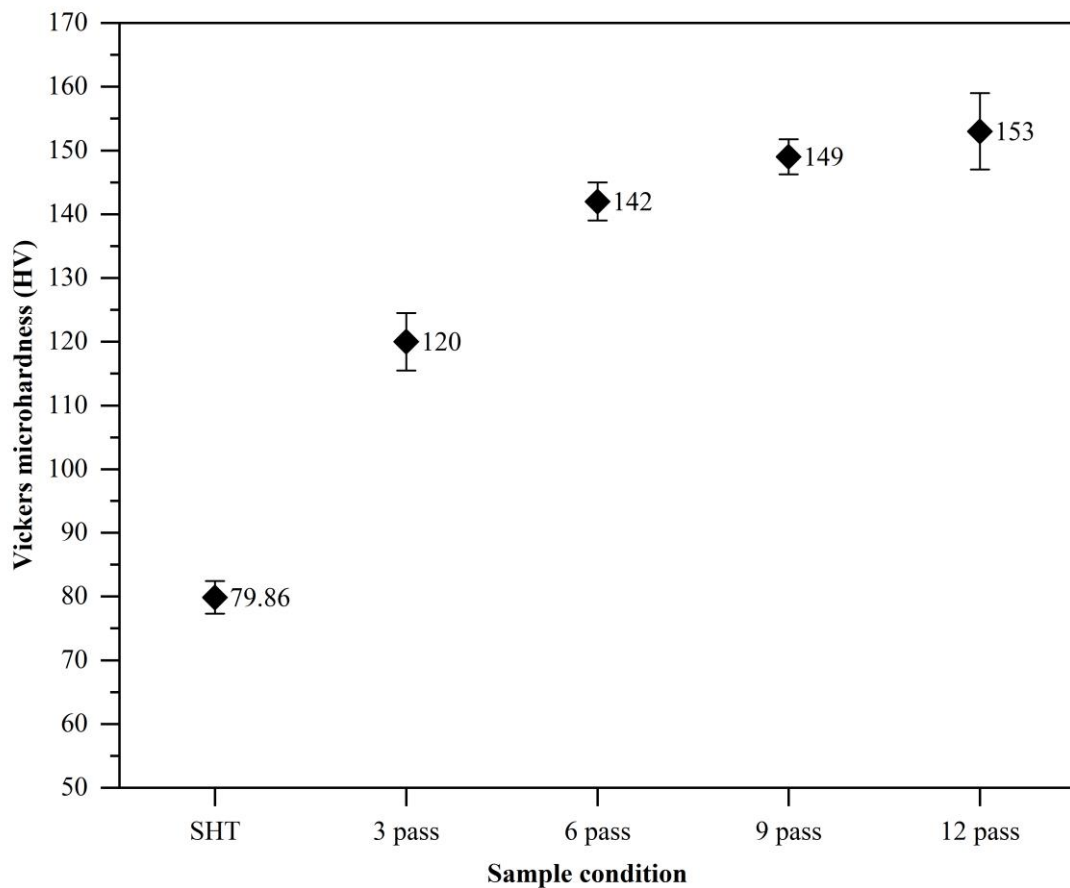


Figure 4.18 Variation of Vickers microhardness of AA2050 Al-Cu-Li alloy subjected to MAF process.

#### 4.2.1.2 Effect of artificial ageing on microhardness

Figure 4.19 illustrates the variation of Vickers microhardness with aging time for samples processed by MAF at 6 and 12 pass and solution treated. The samples were artificially aged for 80 hours at a temperature of 125 °C. The SHT samples exhibited an upward trend in average hardness values until reaching a peak of 139.5 HV at 80 hours of aging. This peak hardness value is considered to be the result of the precipitation of alloying elements within the microstructure of the material, leading to an increase in the hardness. Further, 6<sup>th</sup> and 12<sup>th</sup> pass MAF + aged samples displayed a different trend in hardness values compared to SHT sample. No significant increase in hardness was observed during aging treatment of 6 and 12 pass MAF process samples up to 80 hours of aging. This is due to the low aging temperature of 125°C which is less than the MAF process temperature. The hardness results observed confirms that, aging at lower temperature or temperature below the MAF processing temperature does not have significant effect on the MAF processed samples and thus aging at 125°C is not a optimized temperature for post MAF aging.

Further, Figure 4.20 illustrates the comparison of age-hardening curves for different sample conditions during artificial aging at a temperature of 155°C for a period of up to 80 hours. The sample conditions include Solution Heat Treated (SHT) samples, 6<sup>th</sup> pass, and 12<sup>th</sup> pass MAF processed samples. The SHT samples exhibited an upward trend in average hardness values until reaching a peak of 154 HV at 70 hours of aging. This peak hardness value is considered to be the result of the precipitation of alloying elements within the microstructure of the material, leading to an increase in the hardness. However, with no significant increase in hardness, rather a little drop in hardness has been observed after 70 hours of aging, up to 80 hours. This can be attributed to the fact of over aging that is commonly observed in age hardenable Al alloys.

In contrast, the MAF + aged samples displayed initial softening characteristics until approximately one hour of aging. This is because the MAF process lead to the formation of a large number of defects such as dislocations and sub-grains in the microstructure,

which act as nucleation sites for the precipitation of alloying elements. However, these defects also lead to an initial decrease in hardness until the defects are annealed out by the aging process. Following this initial softening, a gradual increase in hardness was observed until reaching a peak value of 162 HV for the 6th pass samples and 177 HV for the 12th pass samples at 40 hours of aging, respectively. This peak hardness value is an outcome of the precipitation of alloying elements within the microstructure of the material, leading to an increase in the hardness as in SHT samples. Beyond these peak aging conditions, a decrease in hardness was observed for both the 6th and 12th pass samples until the end of the study period at 80 hours. This decrease in hardness is a result of the over-aging of the samples, where the precipitation of alloying elements becomes too excessive leading to coarsening of the precipitates, which in turn leads to a decrease in hardness.

Similar artificial aging were carried out for SHT, 6<sup>th</sup> and 12<sup>th</sup> pass MAF processed samples at 175°C up to 80 hours and the corresponding microhardness were measured at various intervals and reported in Figure 4.21. Similar trends of initial softening during the initial aging periods for MAF processed samples were observed. Additionally, it was noted that the 6<sup>th</sup> pass and 12<sup>th</sup> pass samples attained peak hardness much earlier compared to samples aged at 155°C, at around 25 hours. Also, SHT sample showed peak hardness at 40 hours. Further, a decrease in hardness after attaining peak hardness, attributed to over-aging, and was observed in all sample conditions when aged beyond the peak aging conditions.

It is evident from Figure 4.20 and Figure 4.21 that, SHT samples showed longer duration than MAF processed samples in attaining peak hardness. This indicates the enhanced aging kinetics (Kim et al. 2005; Mazzini and Caretti 1991; Shanmugasundaram et al. 2006). Further holding of samples post peak aging for longer durations reveals the over-aging effect, where a reduction in hardness value has been noticed (Liang et al. 2008).

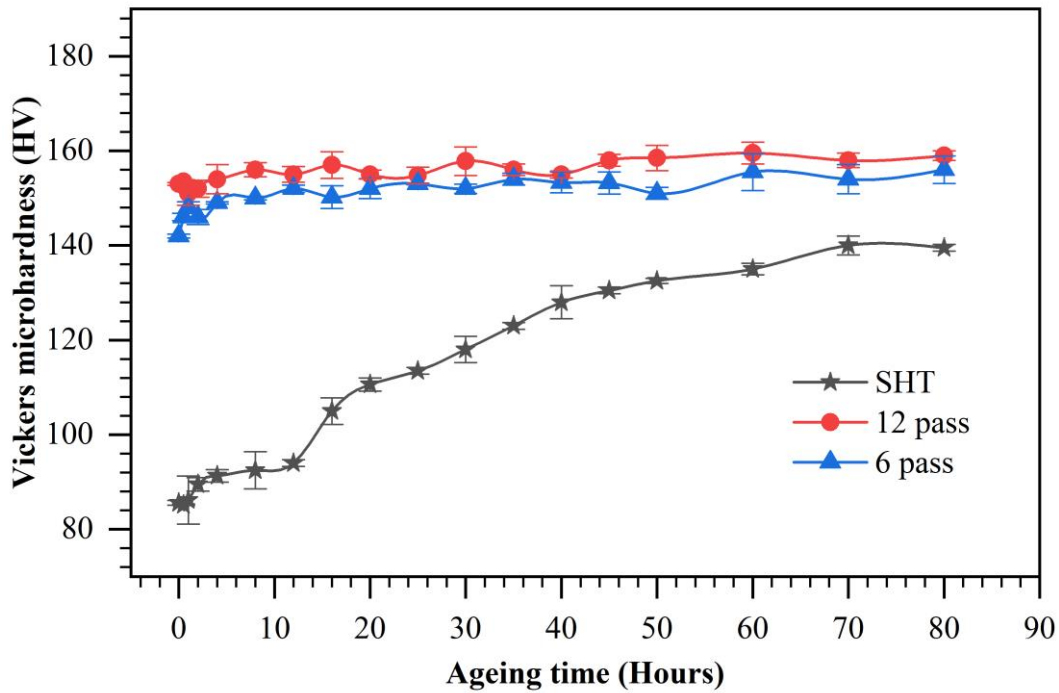


Figure 4.19 Variation of Vickers microhardness of AA2050 alloy artificially aged at 125 °C under different processed conditions.

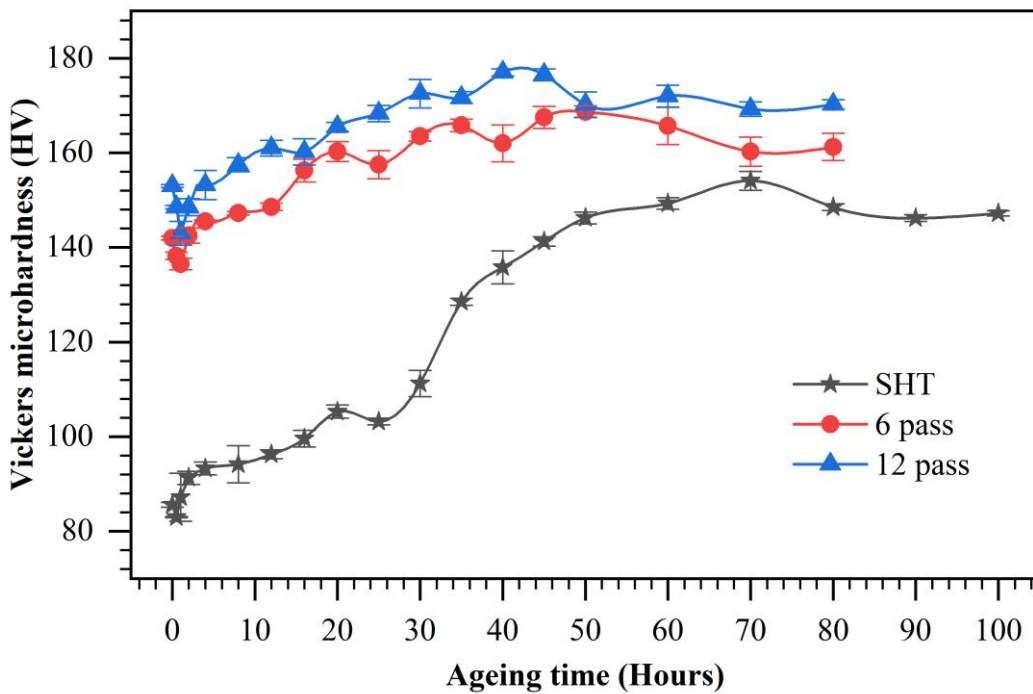


Figure 4.20 Variation of Vickers microhardness of AA2050 alloy artificially aged at 155°C under different processed conditions.

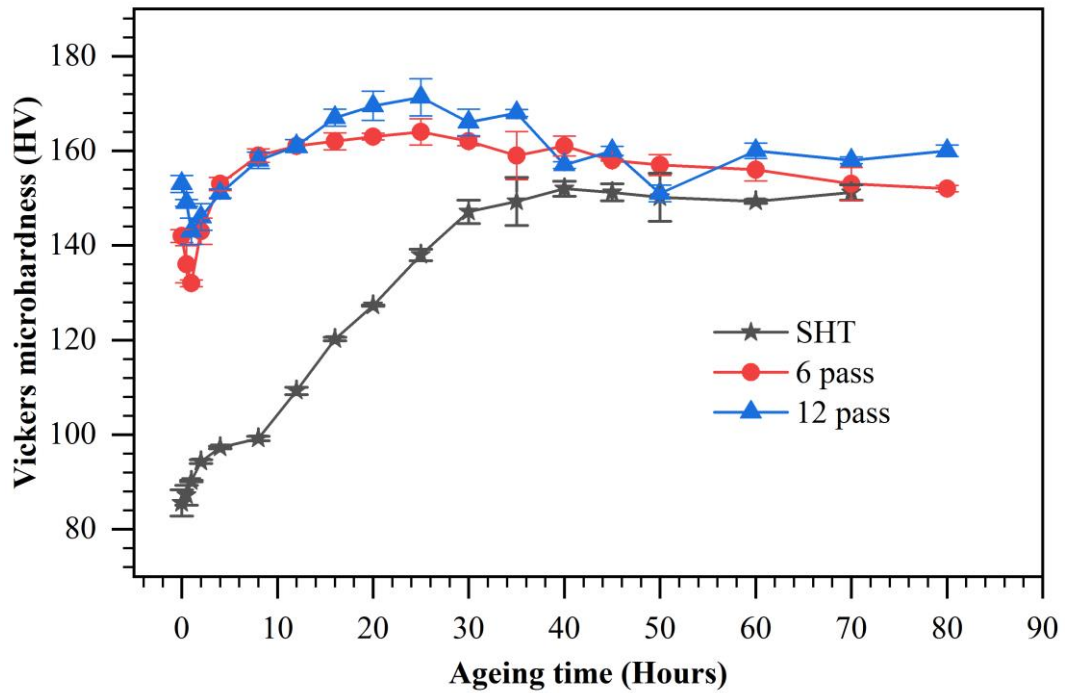


Figure 4.21 Variation of Vickers microhardness of AA2050 alloy artificially aged at 175°C under different processed conditions.

Table 4.1 Vickers microhardness at peak aged conditions for selected sample conditions aged at different temperatures.

Sample	Aging at 125 °C		Aging at 155 °C		Aging at 175 °C	
	Peak micro hardness, (HV)	Peak aging time, (Hours)	Peak micro hardness, (HV)	Peak aging time, (Hours)	Peak micro hardness, (HV)	Peak aging time, (Hours)
SHT	139.5	80	154	70	152	40
6 Pass	149	80	162	40	164	25
12 Pass	156	80	177	40	172.5	25

#### 4.2.2 Tensile behaviour of MAF processed AA2050 Al-Cu-Li alloy

This section explains the influence of MAF processing and post MAF aging on mechanical behaviors of AA2050 Al-Cu-Li Al alloy, characterized using tensile studies. To determine the effect of MAF on the mechanical properties of AA2050 alloy, tensile properties up to 4 cycles of MAF are compared with the SHT samples. Further, tensile studies of 6 and 12 pass MAF processed samples peak aged at 155 °C were carried out to determine the effect of artificial aging post MAF process on mechanical behavior.

#### **4.2.2.1 Effect of MAF processing on tensile behaviour of AA2050 Al-Cu-Li alloy**

Engineering stress-strain curves and the corresponding mechanical properties of the alloy, subjected to MAF processing are shown in Figure 4.22 and Figure 4.23, respectively. Aluminum alloys, having FCC crystal structure, exhibit good ductility, but do not show significant yielding in the plastic region. From Figure 4.22 and Figure 4.23 it is evident that an increase in yield strength (YS) and ultimate tensile strength (UTS) was observed after every MAF cycle. Yield strength (YS) and ultimate tensile strength (UTS) have notably increased after MAF processing, from 204 MPa and 340 MPa in SHT condition to 500 MPa and 517 MPa in 12 pass MAF processed conditions, respectively. An overall increase of 136 MPa has been obtained upon 12 pass MAF processing, however with obvious decrease in ductility from 24% elongation to 8.15% elongation. A overall reduction of 15.85% elongation from SHT condition to 12<sup>th</sup> pass MAF processed condition was observed. During SPD processing of Al alloys, such an increase in strengths with a trade-off with ductility is more commonly reported in the literature (Ramesh et al. 2021b; Sitdikov et al. 2005). This behavior of increase in strengths and reduction in ductility, with an increase in induced strains during SPD, is attributed to grain boundary strengthening and dislocation strengthening (Decreus et al. 2013a; Mazzini and Caretti 1991; Sitdikov et al. 2005).

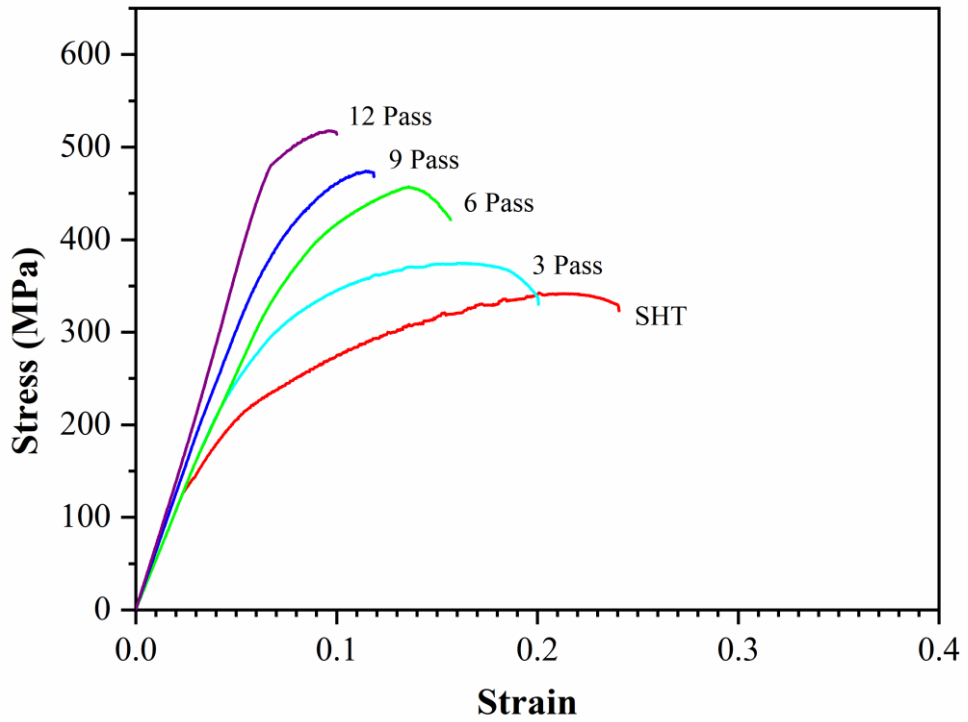


Figure 4.22 Engineering stress-strain curves of AA2050 alloy subjected to MAF process.

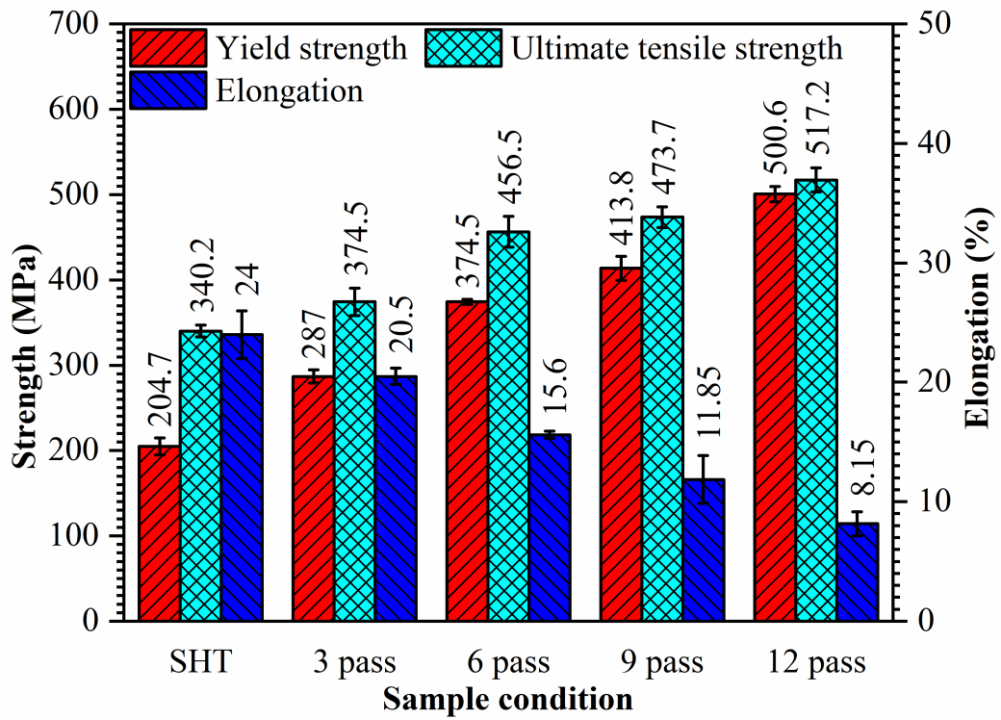


Figure 4.23 Mechanical properties of MAF processed AA2050 Al-Cu-Li alloy.

#### **4.2.2.2 Effect of artificial ageing on tensile behaviour of MAF processed AA2050 Al-Cu-Li alloy on tensile behaviour**

Figure 4.24 depicts engineering stress-strain curves of AA2050 Al-Cu-Li Al alloy investigated at peak-aged conditions of SHT, 6 pass and 12 pass MAF processed samples under aging temperature of 155 °C. Figure 4.25 provides an overview of mechanical properties depicting the effect of artificial ageing on MAF processed samples. Upon MAF processing, UTS increased remarkably from 345 MPa in SHT condition to 478 MPa after 6 Pass MAF and further to 481 MPa after 12 pass MAF processing. An overall increase of 136 MPa has been obtained upon 12 pass MAF processing. However, with oblivious decrease in ductility from 46% elongation to 33% elongation. A very little increase in strength of about 5 MPa was been observed between peak aged samples of 6 pass and 12 pass MAF processing. But, interestingly an increase in elongation by 6% was observed.

Figure 4.24 depicts the stress-strain behaviour of samples at peak aged conditions after subjecting to artificial ageing treatment at 155°C. Peak aging duration of 70 hours for SHT samples and 40 hours for MAF processed samples (6 pass and 12 pass) were reported in microhardness studies. The average values of tensile properties and microhardness of samples processed at various conditions are tabulated in Table 4.2. A increase in microhardness, yield strength and tensile strength has been observed upon aging of MAF samples. MAF + aging of shows better results and 12 pass MAF + aging sample shows highest strength and hardness of 576 MPa and 177 HV, respectively. SHT sample showed highest elongation of 24 % and SHT + MAF 12<sup>th</sup> pass sample showed least elongation of 8 %. Hence, as strength increases ductility of the material decreases, as it subjected to work hardening.

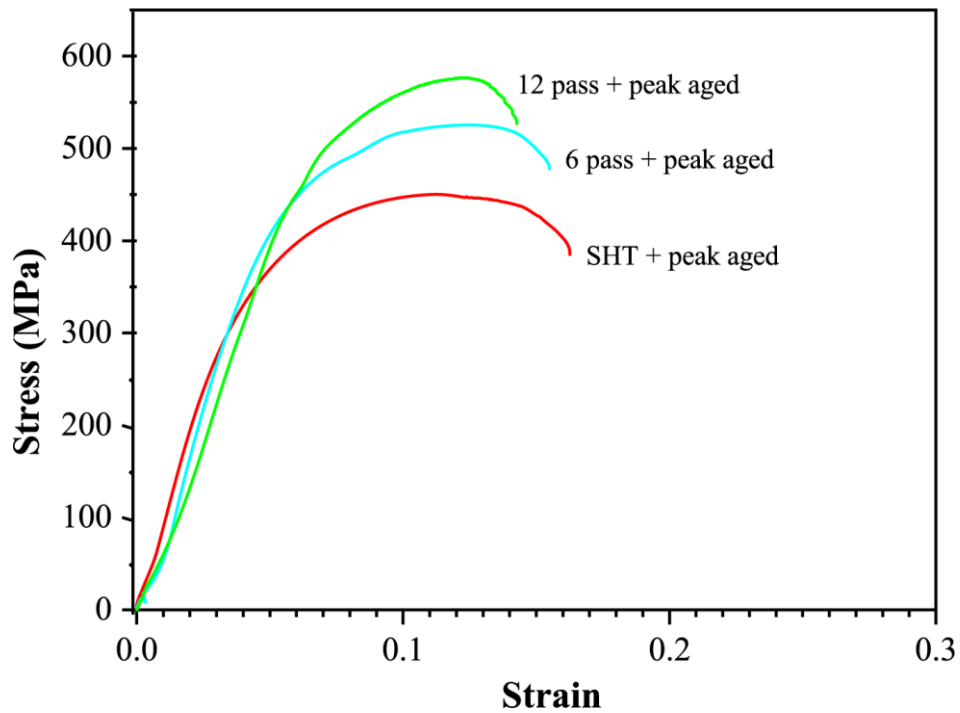


Figure 4.24 (a) Engineering stress-strain curves of MAF processed AA2050 Al-Cu-Li alloy at peak aged condition.

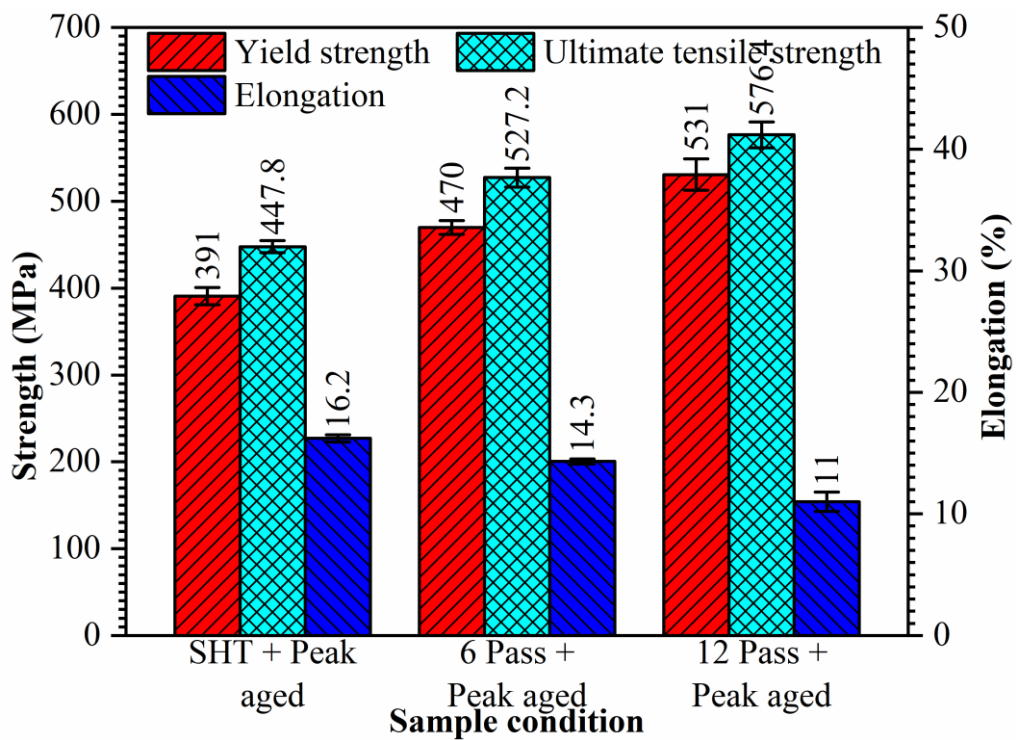


Figure 4.25 Mechanical properties of AA2050 Al-Cu-Li alloy of SHT and MAF processed samples after peak aging.

Table 4.2 The average values of mechanical properties of AA2050 Al-Cu-Li alloy at different processed conditions.

Sample condition	Yield strength, YS (MPa)	Ultimate tensile strength, UTS (MPa)	Elongation at failure (%)	Vickers microhardness, (HV)
SHT	205 ± 10	340 ± 7	24 ± 2	79.86
3 Pass	287 ± 8	375 ± 16	20.5 ± 0.7	120
6 Pass	375 ± 3	457 ± 18	15.6 ± 0.3	142
9 Pass	414 ± 14	474 ± 12	11.9 ± 2	149
12 Pass	501 ± 9	517 ± 14	8.2 ± 1	153
SHT + PA at 155 °C	391 ± 10	448 ± 7	16.2 ± 0.3	154
6 Pass + PA at 155 °C	470 ± 8	527 ± 11	14.3 ± 0.2	162
12 Pass + PA at 155 °C	531 ± 18	576 ± 15	11 ± 0.8	177

#### 4.2.3 Fracture surface analysis

This section presents the SEM observations of fractured surfaces obtained during tensile tests. SEM images of fractured surfaces obtained from tensile tests of all the sample conditions were carefully studied to determine the mode of fracture.

Fractured surfaces of tensile test samples were examined for fractography to understand the mechanism of fracture. Figure 4.26 presents the fractured surface of Al-Cu-Li alloy in various processed conditions. Figure 4.26(a) presents the surface morphologies of SHT sample, where, combination of ductile and brittle fractures was observed. Large number of different sized dimples, were resulting from the more ductile type fracture were identified. Figure 4.26(a) also shows small dimples along the tear ridges corresponding to brittle fracture or material tear attributing to the brittle fracture. Figure 4.26(b) shows the fractured surface of 3 pass MAF processed sample with large number of elongated dimples and the presence of rupture regions indicating transient fracture. It should be noted that the depth of the dimples are reduced when compared to SHT

sample. 3 pass MAF sample showed good agreement with increase in hardness and tensile strength, and reduction in ductility. Fractography indicates the transformation of the sample from ductile to brittle fracture during MAF process as a result of strain accumulation. Similar features are observed in 6, 9 and 12 pass MAF processed samples, showing relatively large ruptured regions with more tear ridges, following reduced ductility. It is also evident that, there was a decrease in density and size of dimples with increase in number of MAF passes. This confirms brittle mode of fracture compared to ductile mode observed in SHT samples. These observations are in good agreement with the tensile test results reported in Section 4.2.2.1.

Figure 4.27 presents the fractured surface morphologies of SHT, 6 and 12 pass MAF processed samples after subjecting to artificial aging at 155 °C in peak aged condition. Figure 4.27(a) shows a significant amount of dimples along with step ridges and this represents, the effect of aging kinetics on SHT sample, caused by dissolution of dislocation clusters. Figure 4.27(b) presents the fractured surface of 6 pass MAF sample after peak aging and shows combination of clustered dimples and ruptured region. The presence of clustered dimples along the tear ridges is in good agreement with the reduced ductility observed when compared to SHT + peak aged condition. Similarly, Figure 4.27(c) shows the fractured surface of 12 pass peak aged sample with long straight ridges by coalescence of small dimples in the pattern of straight lines indicating mixed mode of fracture with further reduction in ductility. Presence of more dimples and less ruptured regions on 6 and 12 pass peak aged samples as seen in Figure 4.27(b, c) indicate more ductility in the samples as compared to un-aged counterparts in Figure 4.26(c, e) and are in good agreement with increase in ductility observed upon aging. Thus, the observed fractured surface morphologies after aging are in good the tensile test results reported in Section 4.2.2.2. where a slight increase in ductility was observed post aging of MAF processed samples.

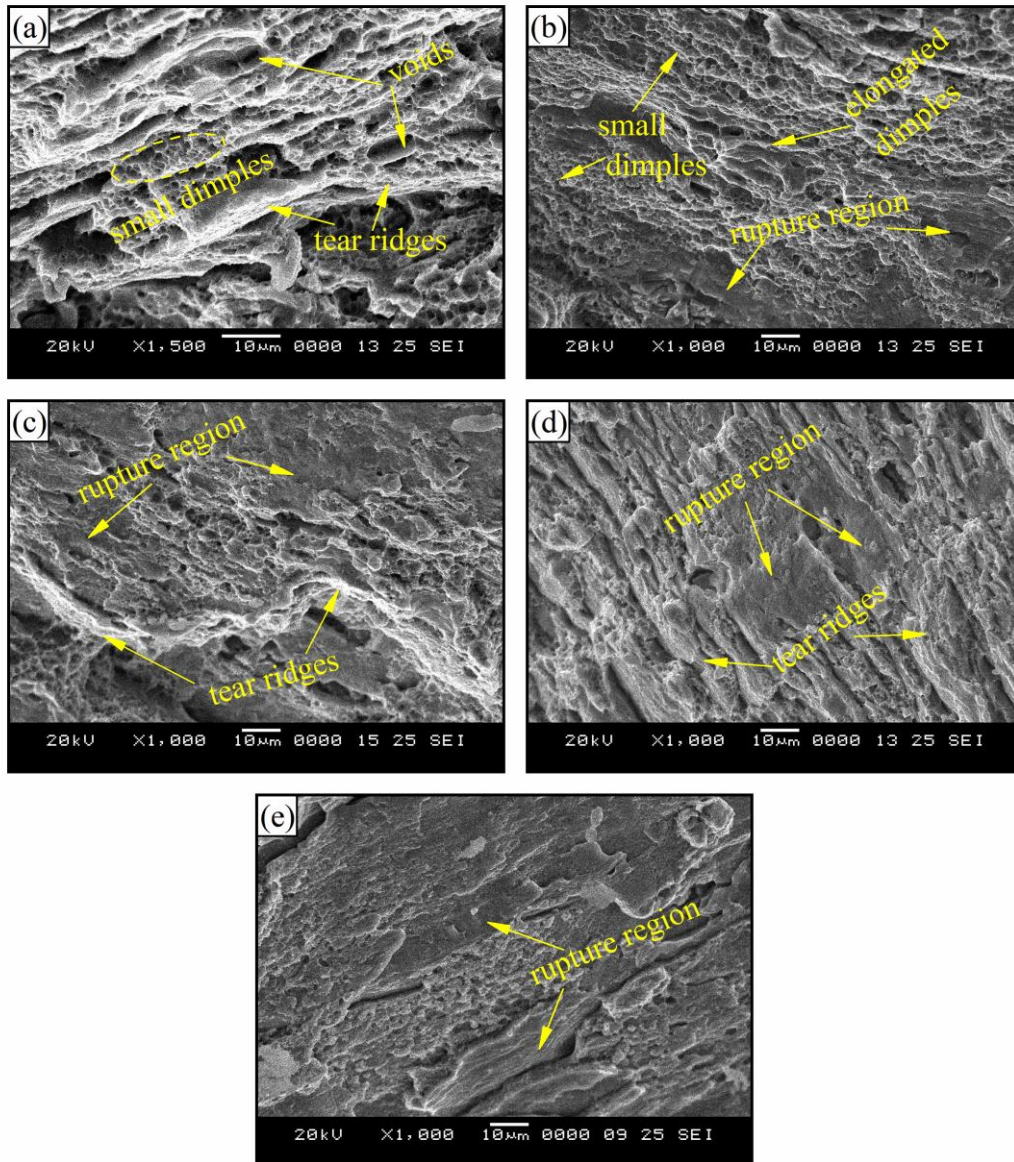


Figure 4.26 SEM observations for the fractured surfaces of the tensile samples, respectively in (a) SHT, (b) 3 pass, (c) 6 pass, (d) 9 pass, and (e) 12 pass MAF processed condition.

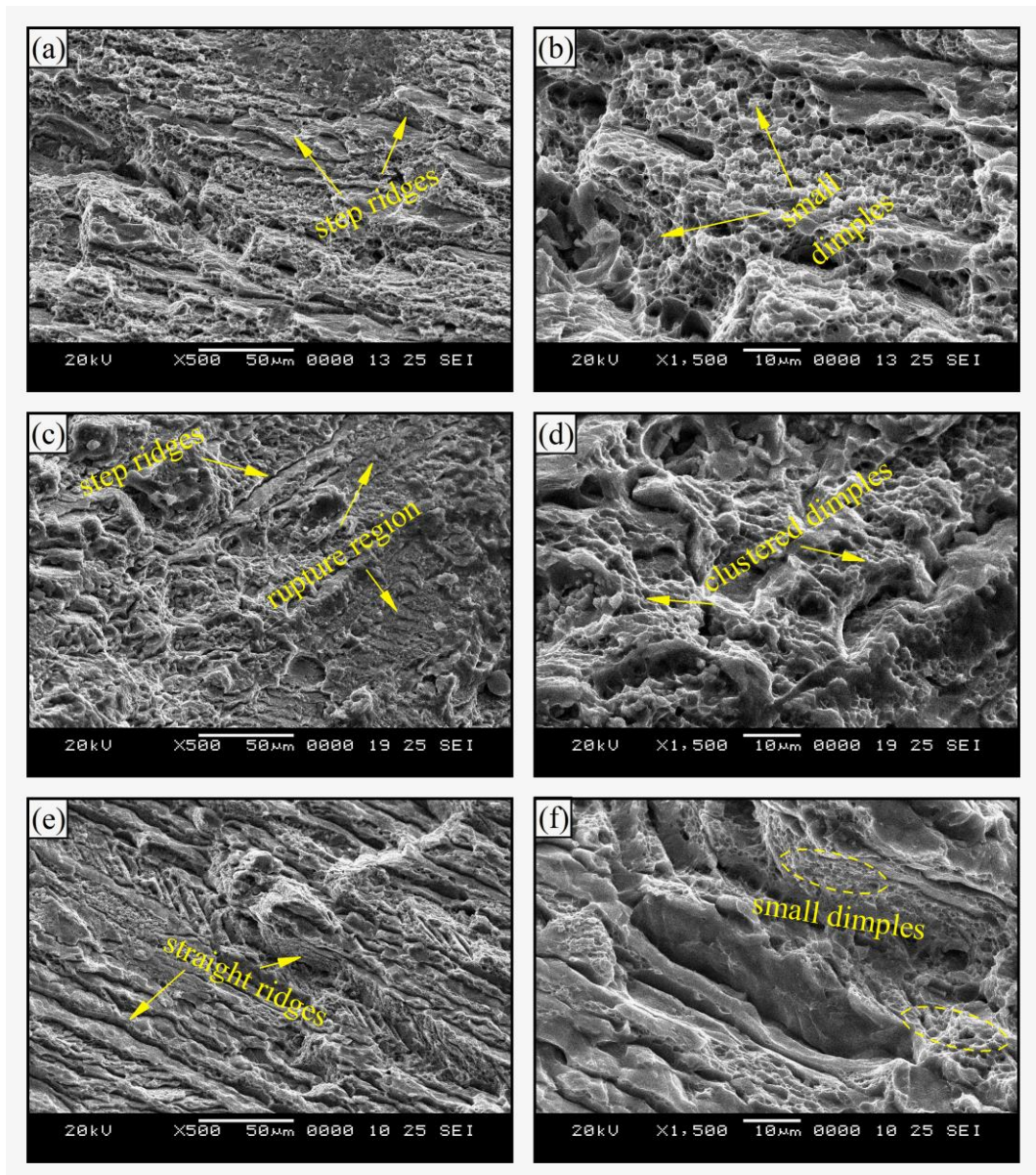


Figure 4.27 SEM observations for the fractured surfaces of the tensile samples, respectively in (a,b) SHT + PA, (c,d) SHT + 6 pass + PA, (e,f) 12 pass + PA MAF processed condition.



## CHAPTER 5

### RESULTS AND DISCUSSION: CORROSION AND WEAR STUDIES

This chapter presents results and observations obtained through a series of characterizations on corrosion and wear behaviour of AA2050 alloy in various processed conditions. This chapter presents the findings from various characterizations and the correlation of the same with the existing literature.

#### 5.1 Corrosion studies

Al-Cu-Li alloys find widespread application in the aerospace sector due to their lightweight and impressive strength-to-weight ratio. However, like all metals, Al-Cu-Li alloys are prone to corrosion. A process involving chemical or electrochemical reactions between the material and its surroundings, leading to the degradation of the material properties. In this case, corrosion of Al-Cu-Li alloys can substantially affect the mechanical properties and ultimately lead to their failure. In this section, the electrochemical behaviour of Al-Cu-Li alloys after various processing conditions in 3.5 wt.% NaCl solution are investigated. Further, the corroded surfaces are inspected to conclude the corrosion mechanism. Cross sections of the corroded surfaces were also investigated to observe pitting behaviour of Al-Cu-Li alloy in different processed conditions.

##### 5.1.1 Open circuit potential (OCP) of AA2050

Variation of OCP in 3.5 wt.% NaCl solution with respect to aging period for various processed conditions of AA2050 alloy is shown in Figure 5.1. OCP represents the corrosion potential of the material in environmental conditions without the influence of external potential or current. Overall OCP values ( $E_{ocp}$ ) varied within the range of  $-0.75 \pm 0.06$  mV and are in good agreement with the  $E_{ocp}$  values reported for various Al-Cu-Li alloys (Zou and Chen 2018) and are relatively positive when comparison to other Al alloys, indicating good corrosion resistance. As shown in Figure 5.1, OCP of 6 and 12 pass samples is more noble than the SHT sample, indicating stable oxide film formation during the study period. It's worth noting that, for all processed conditions, upon artificial aging, the potentials shift towards negative values.

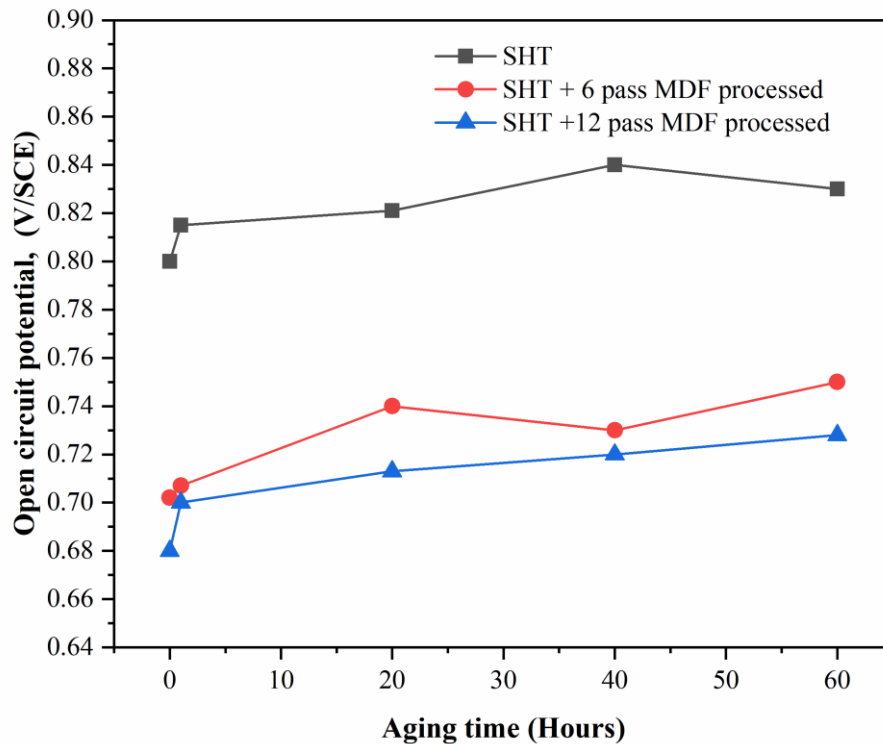


Figure 5.1 Open circuit potential over aging time at 155 °C for various processing conditions of AA 2050 Al-Cu-Li alloy.

### 5.1.2 Potentiodynamic polarization studies

Corrosion susceptibility of AA2050 Al-Cu-Li alloy under various processed conditions were evaluated using polarization studies. As depicted in Figure 5.2, the initial anodic curves of 6 pass and 12 pass MAF processed samples exhibit minimal change in current density with increasing applied potential. This indicates the initial passivation of the alloy. However, as the applied potential surpasses  $\sim 700$  mV/SCE, MAF processed samples display an increase in current density with increase in applied potential, indicating de-passivation as a result of dissolution of the alloy (Zhang et al. 2022). Potential at which de-passivation occurs is referred to as the breakaway potential ( $E_b$ ) and was found to be approximately the same for both 6 pass and 12 pass samples. In contrast, the anodic curve of SHT samples exhibit early de-passivation, which indicate that the oxide film on the SHT sample is less stable.

Figure 5.3 illustrates anodic polarization curves at peak aged conditions of SHT, 6 pass and 12 pass MAF processed samples. In contrast to non-aged samples, peak aged samples exhibit a greater change in current density with minimal increase in applied potential and no signs of anodic passivation. However, corrosion potentials shift to

more positive values after peak aging. Jiang et al. (2020) reported similar trends of corrosion potential which become more noble with increase in aging duration in Al-Cu-Li alloys. Tafel analysis was performed to determine the current densities ( $I_{\text{corr}}$ ), corrosion potential ( $E_{\text{corr}}$ ), and corrosion rate (CR) and is reported in Table 5.1. SHT and MAF processed samples displayed lower resistance to corrosion due to the presence of large crystalline defects. However, peak aged samples of all processed conditions exhibited improved corrosion resistance compared to un-aged sample conditions, with the 12 pass and peak aged sample showing highest resistance to corrosion. This is likely as a result of formation of large grain/subgrain boundaries, distribution of fine intragranular precipitates, and the prevention of GB precipitates, as a result of induced strains during MAF processing.

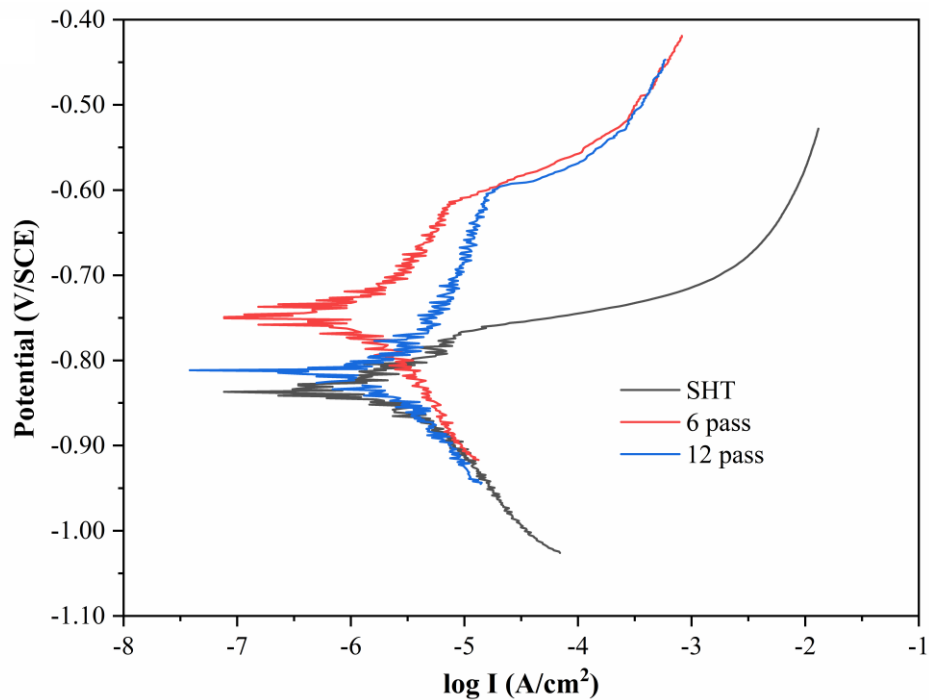


Figure 5.2 Polarization curves of AA2050 alloy in different processed conditions prior to artificial aging in 3.5 wt% NaCl solution.

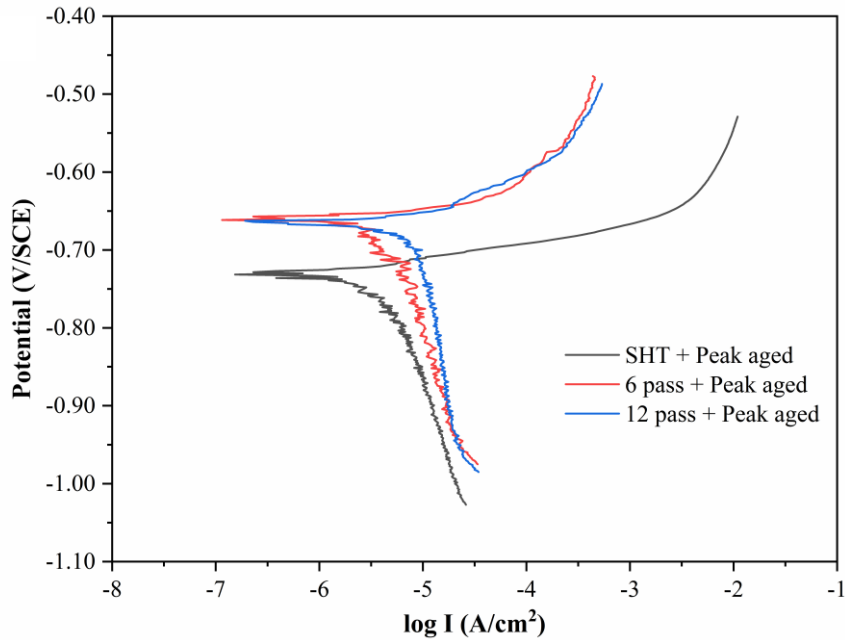


Figure 5.3 Polarization curves of AA2050 alloy in different processed conditions after peak ageing in 3.5 wt% NaCl solution.

Table 5.1 Electrochemical parameters of AA2050 alloy under different processed conditions derived from polarization curves.

Sample condition	Corrosion potential	current densities	corrosion rate
	( $E_{corr}$ )(V/SCE)	( $I_{corr}$ ) (A/cm <sup>2</sup> )	CR (mm/y)
SHT	-0.843	5.54	0.060
6 pass	-0.752	5.80	0.061
12 pass	-0.812	5.76	0.064
SHT +Peak aged	-0.731	5.39	0.059
6 pass + Peak aged	-0.661	5.37	0.058
12 pass + peak aged	-0.665	5.12	0.055

### 5.1.3 Corrosion surface morphology

Corroded surface morphologies of AA2050 alloy samples at various processed conditions are examined and are shown in the Figure 5.4. Corroded surface of SHT specimen, shown in Figure 5.4(a, b) is similar to that of a nearly flat surface, without formation of pits. Exfoliation of scales formed with corrosion particles embedded on the surface is apparent. In contrast, as seen in Figure 5.4(c, d), corroded surface morphology of the 6th pass MAF processed sample exhibits reduction in corrosion products. It is apparent from Figure 5.4(d) that the heavier film has been peeled off,

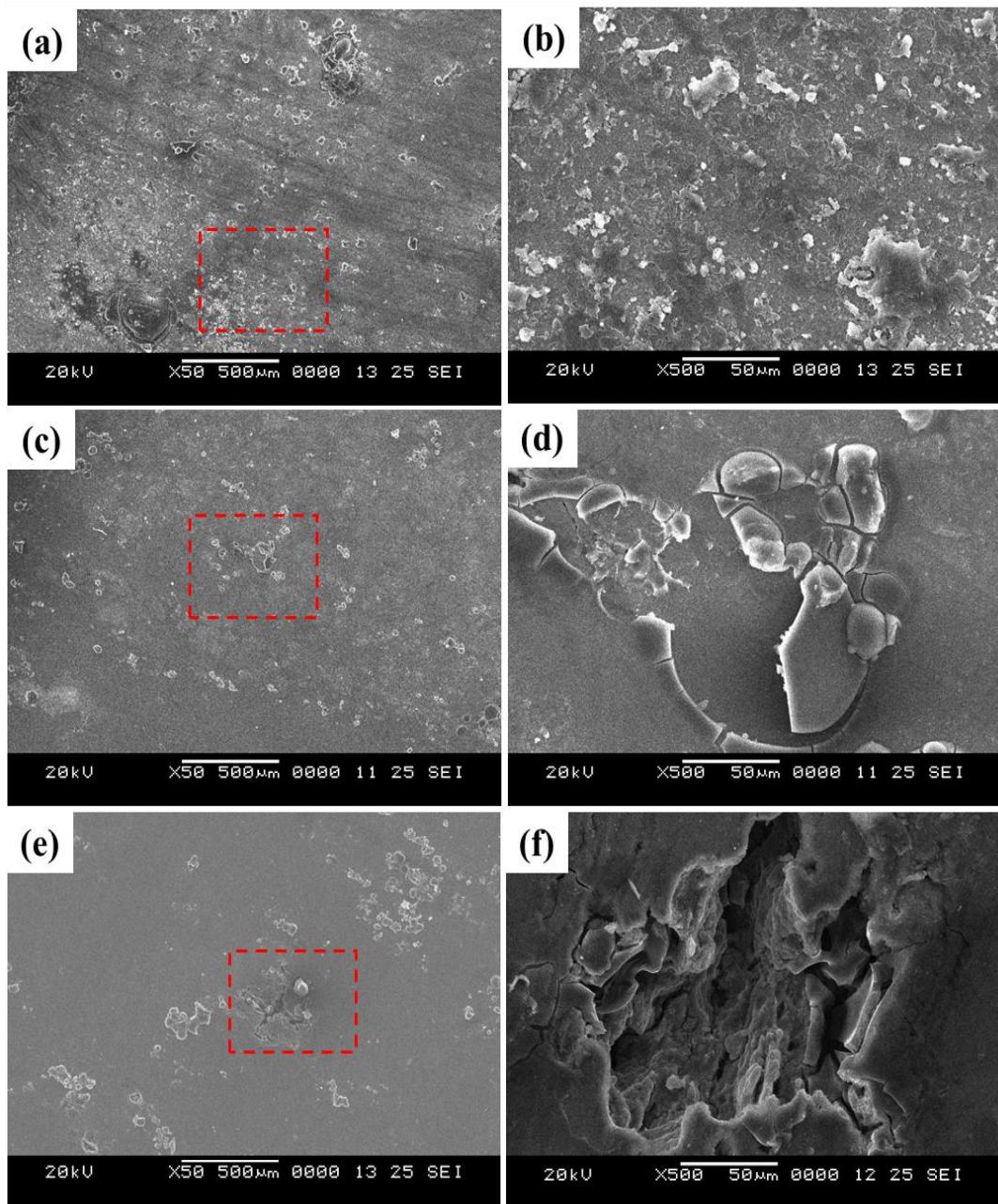


Figure 5.4 SEM corrosion surface morphologies of AA2050 Al-Cu-Li alloy in different processed conditions: (a,b) solution heat treated, (c,d) 6th pass MAF processed, and (e,f) 12th pass MAF processed.

revealing the flat internal matrix alloy surface. These observations align with the Tafel plots (Figure 5.2), which indicate that de-passivation has occurred at faster rate in SHT sample compared to MAF samples. In 12th pass sample, in addition to the exfoliation of the corrosion film, deepest corrosion ditches are also apparent as seen in Figure 5.4(e,f). SHT sample displayed flat corrosion surfaces, indicating uniform corrosion. Previous studies by Zou and Chen (2018) and Wen et al. (2022) reported the improved

corrosion resistance when Al-Cu-Li alloy is solution heat-treated, because of absence of intermetallic phases/precipitates. With increase in strain due to MAF processing, shallow and wider corrosion ditches are formed indicating reduction in corrosion resistance in MAF 12 pass samples.

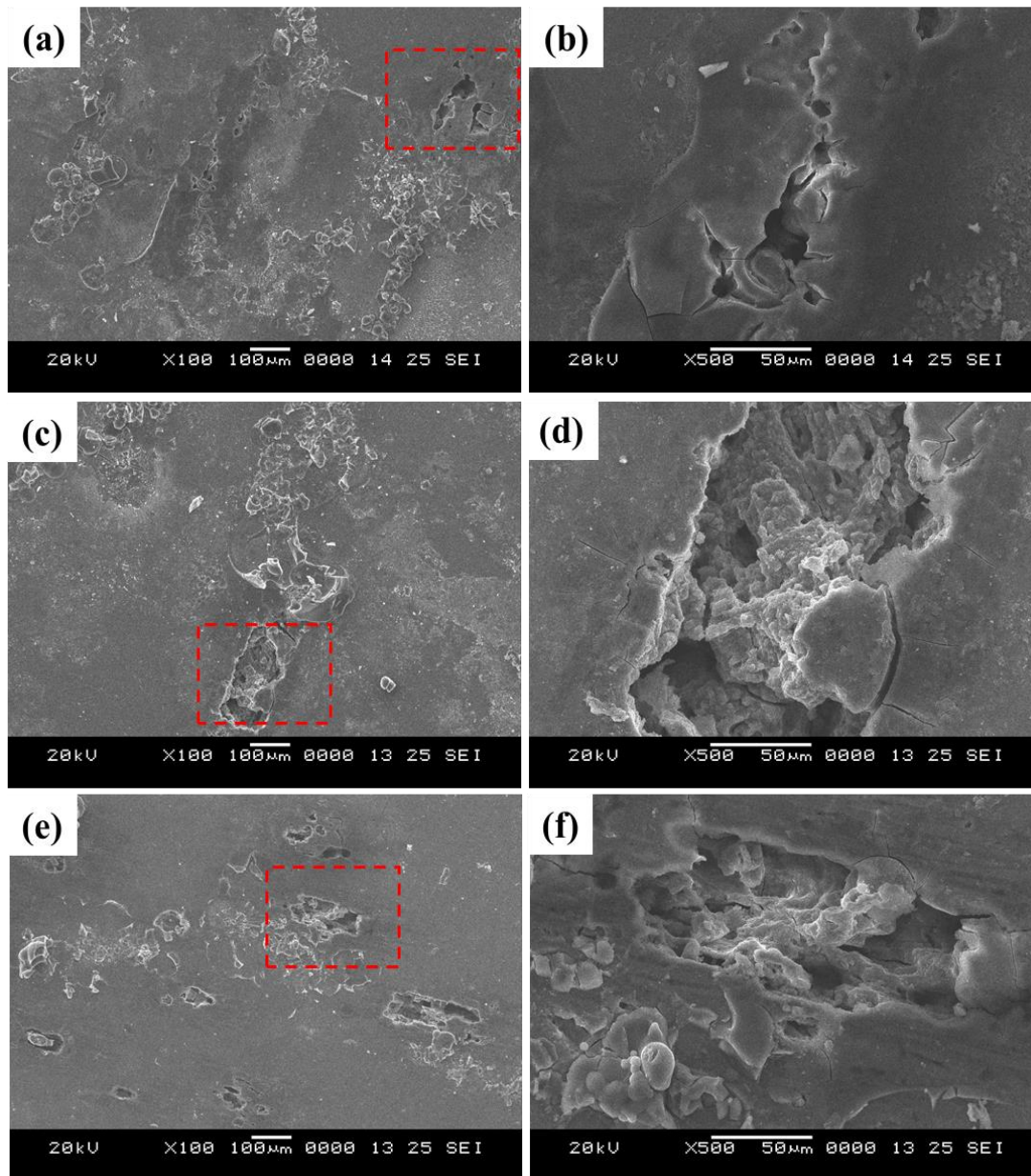


Figure 5.5 SEM corrosion surface morphologies of AA2050 Al-Cu-Li alloy in different processed conditions: (a,b) SHT + peak aged, (c,d) 6th pass + peak aged, and (e,f) 12th pass + peak aged.

Figure 5.5 illustrates SEM morphologies of corroded surfaces of SHT, 6th pass, and 12th pass samples in peak aged condition during aging at 155 °C. A change in corrosion

susceptibility and morphology after aging heat treatment was noticed. SHT + peak aged samples exhibit pits on the corroded surface, indicating severe localized corrosion (SLC). The size of the pits was observed to be larger in 6 pass + peak aged samples. An additional increase in width of the pits was observed in 12 pass + peak aged samples.

#### **5.1.3.1 Intergranular corrosion (IGC)**

Figure 5.6(a) illustrates the corrosion morphology of SHT specimen along the L-LT (longitudinal to longitudinal transverse) planes following a 10 hour exposure to a 3.5 wt.% NaCl solution. Corrosion anomalies examined along the L-LT planes of SHT samples, were predominantly located within the grain interiors with homogeneous distribution resembling uniform, less detrimental, intragranular corrosion. 6 pass and 12 pass MAF processed samples also displayed similar susceptibility to intragranular corrosion as depicted in Figure 5.6(b, c). However, in MAF treated specimens, the corrosion areas were discontinuous, with wider and deeper corrosion depths, indicative of pitting corrosion. As depicted in Figure 5.6(d), in peak aged sample after SHT, corrosion mode was primarily intergranular corrosion (IGC) and the observed results were in concordance with TEM results. Corrosion potential of  $T_1$  precipitates were found to be more negative in comparison to the matrix, with a value of -1.076 V/SCE for  $T_1$  precipitates and -0.855 V/SCE for the matrix in a 4 wt.% NaCl solution (Jiang et al. 2022). Furthermore, as evidenced in Figure 4.13(a-c), SHT + peak aged specimens exhibited large  $T_1$  precipitates at grain boundaries with PFZ formation. This resulted in a shift in GB potential to a more negative value, leading to galvanic coupling between the precipitates and the adjacent matrix, resulting in IGC. Further propagation of corrosion damage was observed to be severe. In Al-Cu-Li alloys, Similar findings of change in corrosion susceptibility from intragranular to IGC was reported by Jiang et al. (2020). However, peak aged samples, after MAF processing displayed different modes of corrosion compared to conventionally aged specimens (SHT + peak aged). The 6 pass + peak aged samples, exhibited corrosion characteristics, primarily composed of pitting with only slight IGC as depicted in Figure 5.6(e). Additionally, it was also evident that the corrosion was not uniform throughout the L-LT surface. Furthermore, the 12 pass + peak aged specimen solely exhibited susceptibility to intragranular corrosion with U-shaped pits, as depicted in Figure 5.6(f). As discussed in TEM characterization in Section 4.1.3, MAF prior to aging, promoted intragranular

fine precipitation by the consumption of Cu solute atoms in the matrix, resulted in suppression of subgrain/grain boundary precipitates. The existence of high density of fine  $T_1$  precipitates within the grains and the absence of GB precipitates, may result in a shift in the intragranular matrix's corrosion potential, towards a more negative value, compared to the subgrain/grain boundary. This makes the grain interiors more susceptible to corrosion, resulting in intragranular corrosion.

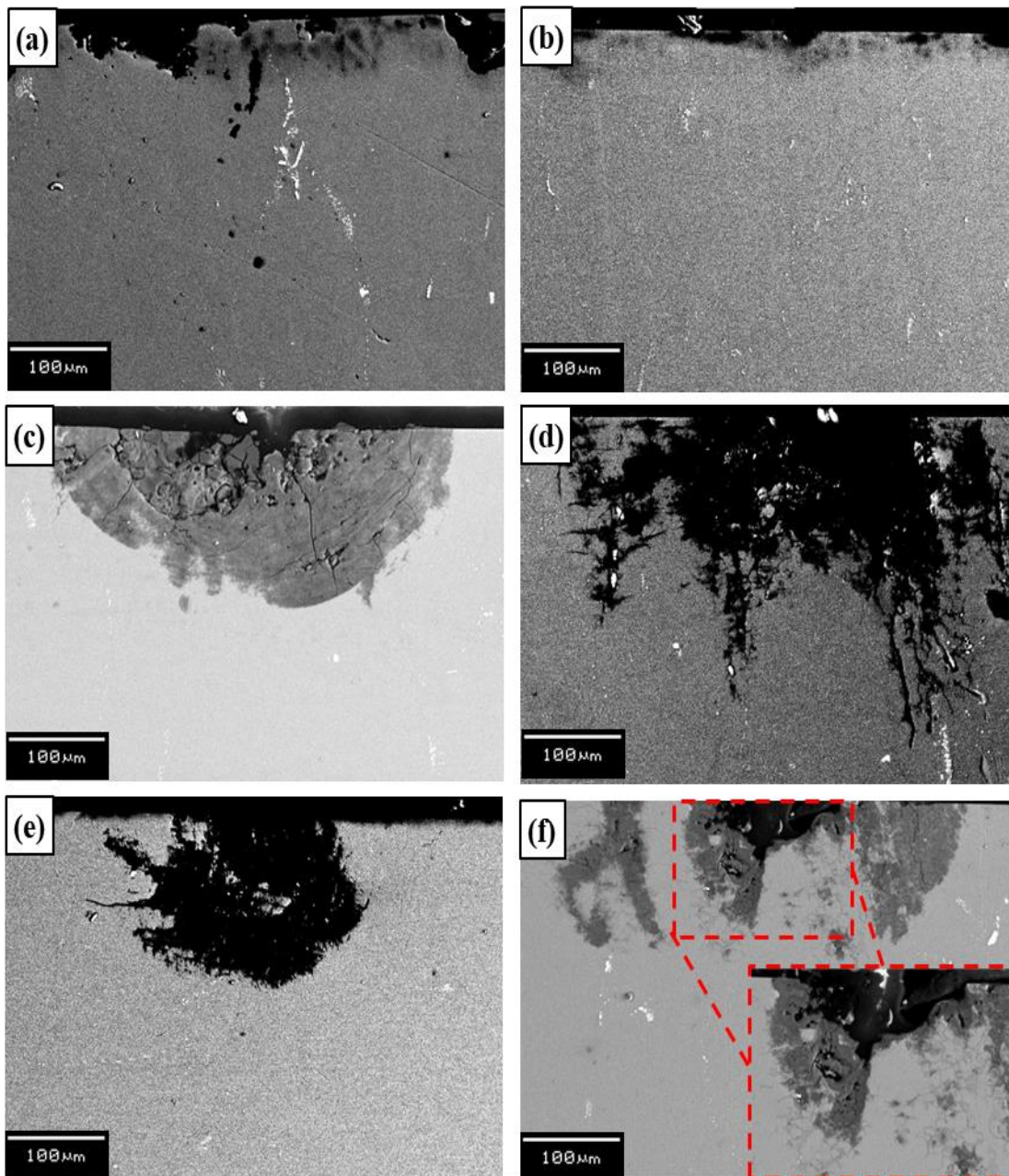


Figure 5.6 Corrosion surface micrographs of the AA2050 in the L-LT plane for (a)SHT, (b) 6 pass, (c) 12 pass, (d) SHT + peak aged, (e) 6 pass + peak aged, and (f) 12 pass + peak aged samples after 10 hours of immersion in the electrolyte.

## 5.2 Wear analysis results

This section presents the results obtained from various characterizations to understand the effect of MAF and post MAF artificial aging on wear behaviors of AA2050 alloy. Worn surface observations, counter surface morphologies and wear debris characterizations are also presented.

### 5.2.1 Wear properties

Figure 5.7 to Figure 5.12 depicts the variation in coefficient of friction (COF) of AA2050 alloy in various processed conditions under normal load conditions of 2, 4, 6 and 10 N during reciprocating sliding wear tests. SHT samples exhibited high COF initially, which gradually decreases and stabilizes, characterizing the "running-in" stage, that lasts up to ~1500 cycles for all loading conditions. However, for the 6 pass and 12 pass MAF processed samples, the "running-in" stage reduces to ~500 cycles and further decreases under normal loads of 6 and 10 N. Moreover, COF fluctuates largely with lower normal loads (2 and 4 N) for all processed conditions, while the amplitude of fluctuation reduces at higher loads (6 and 10 N). Thus, it can be summarized that with increase in normal load, contact area increases, and fluctuation of COF decreases for all processing conditions. Further, for all samples that were subjected to aging heat treatment, running-in stage was lower than ~250 cycles, and the fluctuating amplitude was low for all load conditions. Additionally, variation in COF remained stable throughout the study period (up to 5000 cycles).

#### 5.2.1.1 Average coefficient of friction (COF)

To gain further insight into the wear behavior of AA2050 alloy under different normal load conditions, variation of average COF for various processing conditions was plotted against normal loads in Figure 5.13. SHT, 6 and 12 pass MAF processed samples exhibited a decreasing trend of COF, with increase in normal loads, as shown in Figure 5.13(a). SHT samples demonstrated lower COF than MAF processed samples under all normal load conditions, with 6 pass samples exhibiting higher COF. However, 12 pass MAF processed samples displayed intermediate values of COF compared to SHT and 6 pass samples with a similar decreasing trend with an increase in normal loads.

Furthermore, artificially aged SHT, 6, and 12 pass samples exhibited similar trend of decreasing COF with increase in normal loads, as depicted in Figure 5.13(b). Similar

to unaged samples, shown in Figure 5.13(a), aged SHT samples displayed lower COF compared to aged 6 and 12 pass samples. Interestingly, after aging, unlike unaged samples, 12 pass samples showed maximum COF for all normal load conditions. This suggests that, upon aging, with increase in the number of MAF passes, COF also increase. Aging of Al alloys promotes nucleation and formation of hardening precipitates resulting in the increases in hardness and thus increase in COF.

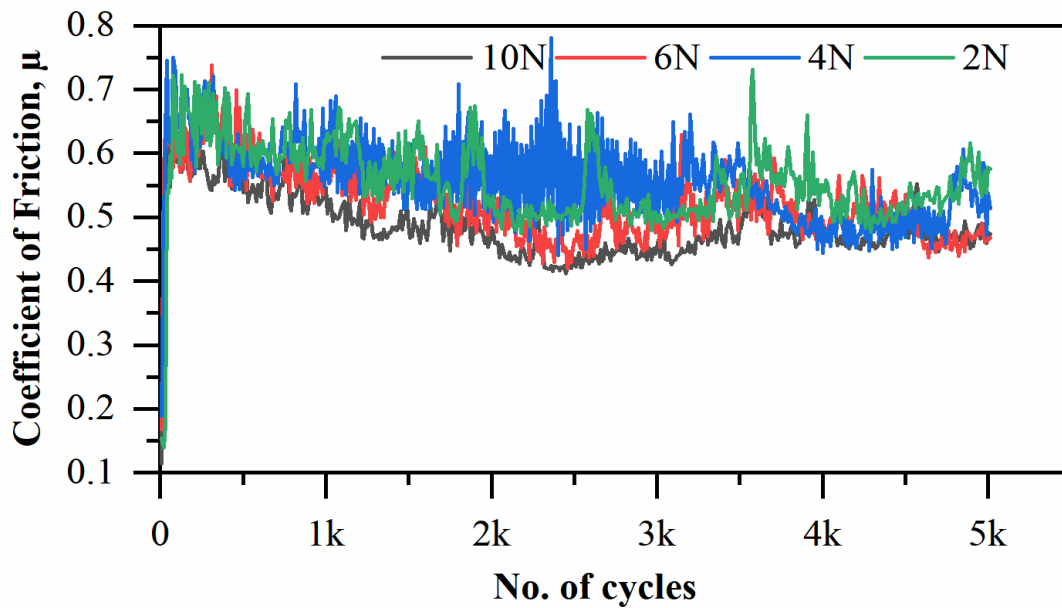


Figure 5.7 No. of reciprocating wear cycles v/s coefficient of friction (COF) at different normal load conditions in SHT sample condition.

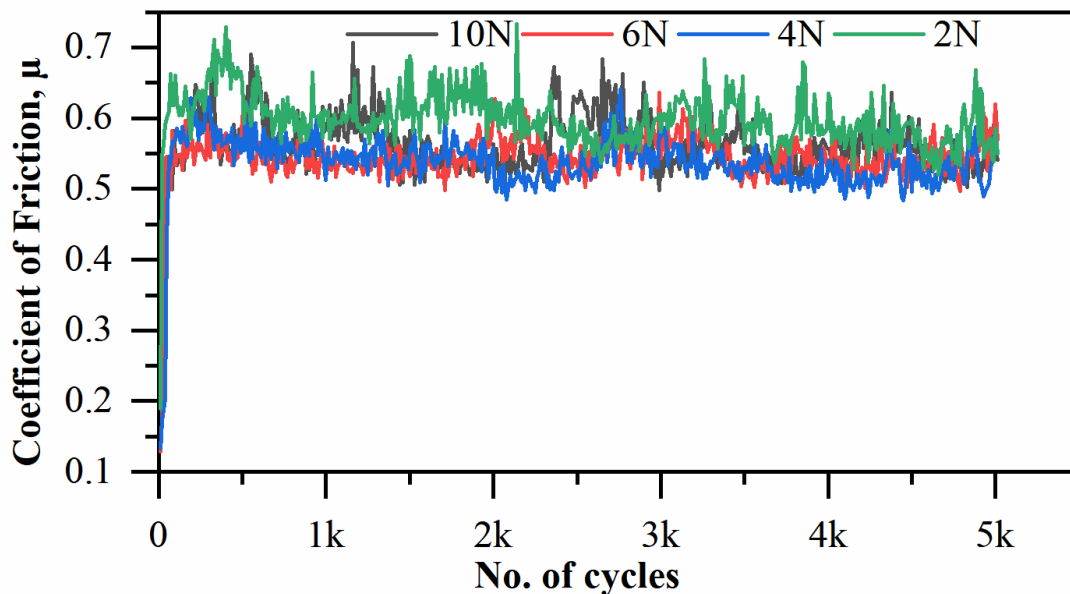


Figure 5.8 No. of reciprocating wear cycles v/s coefficient of friction (COF) at different normal load conditions in 6 pass MAF processed sample condition.

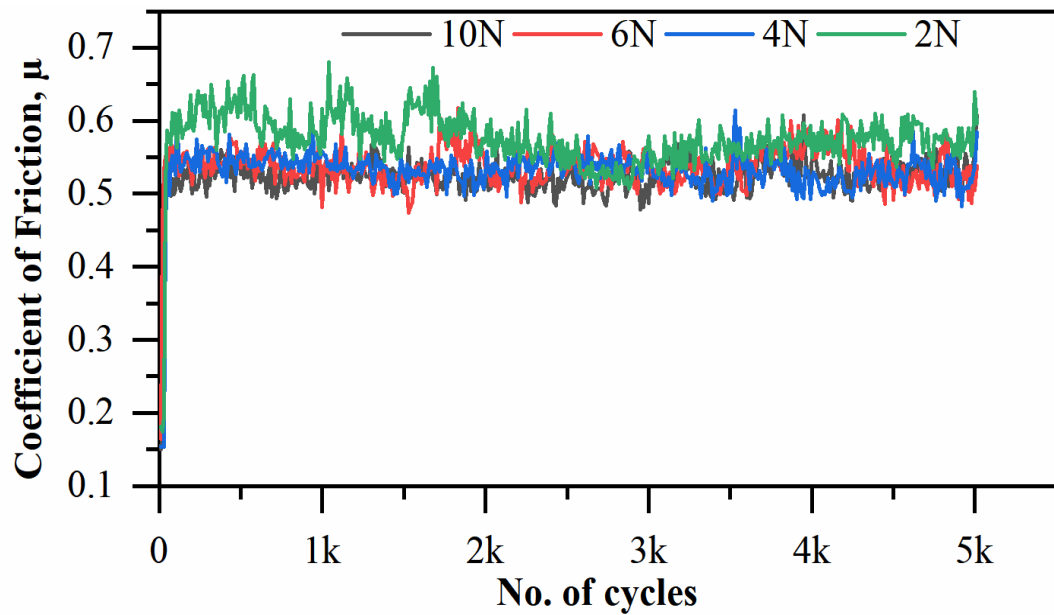


Figure 5.9 No. of reciprocating wear cycles v/s coefficient of friction (COF) at different normal load conditions in 12 pass MAF processed sample condition.

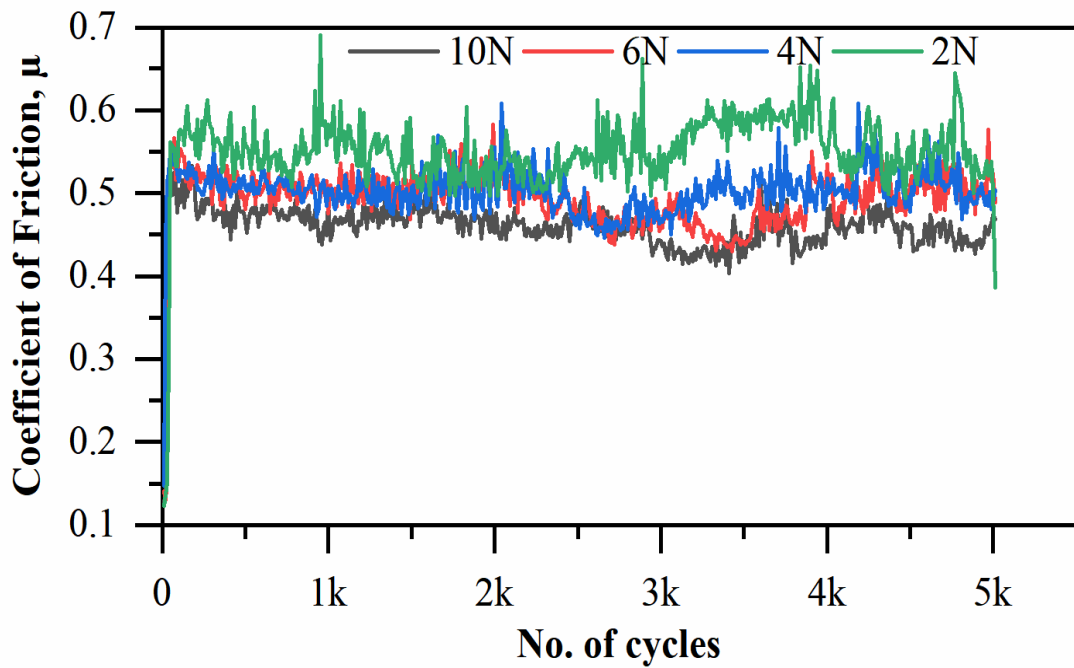


Figure 5.10 No. of reciprocating wear cycles v/s coefficient of friction (COF) at different normal load conditions in SHT+peak aged sample condition..

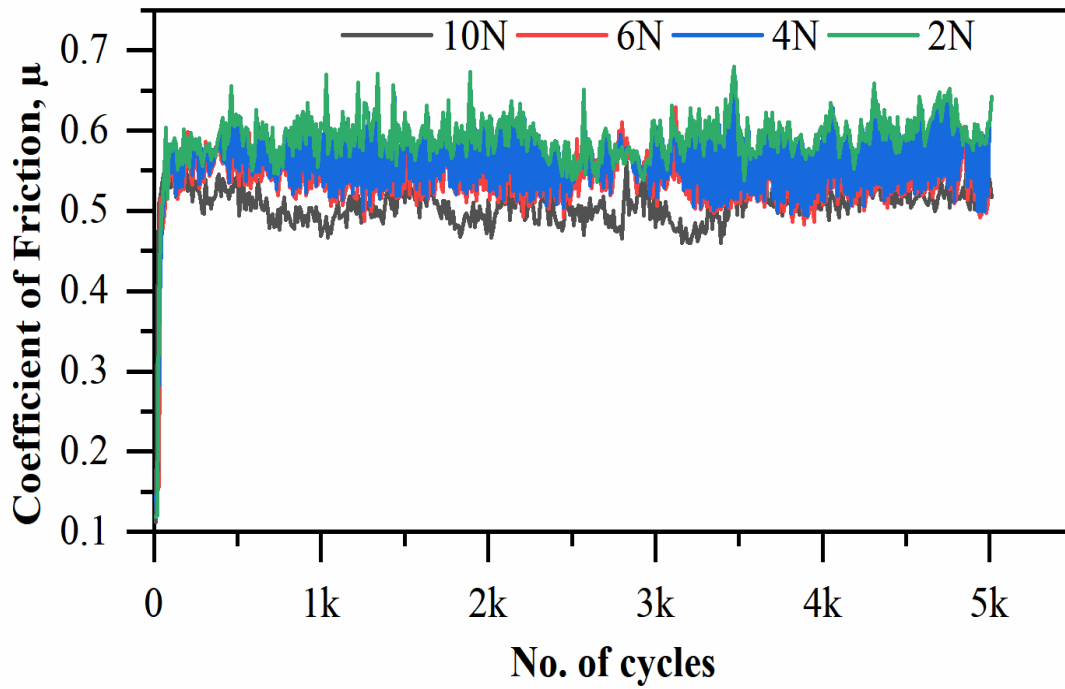


Figure 5.11 No. of reciprocating wear cycles v/s coefficient of friction (COF) at different normal load conditions in 6 pass + peak aged sample condition.

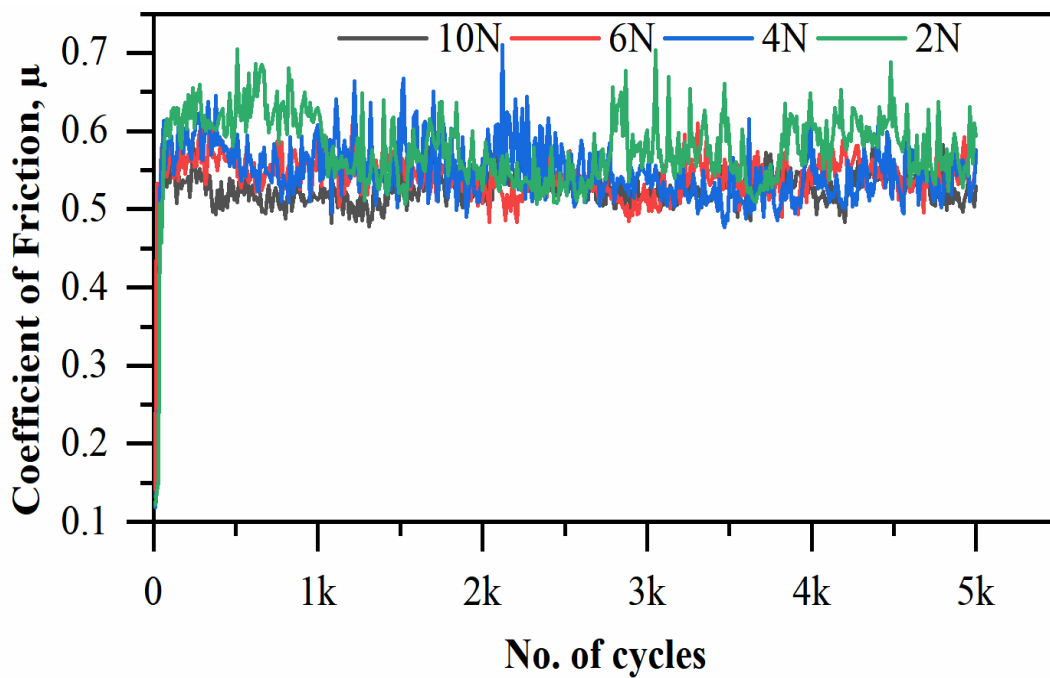


Figure 5.12 No. of reciprocating wear cycles v/s coefficient of friction (COF) at different normal load conditions in 12 pass + peak aged sample condition.

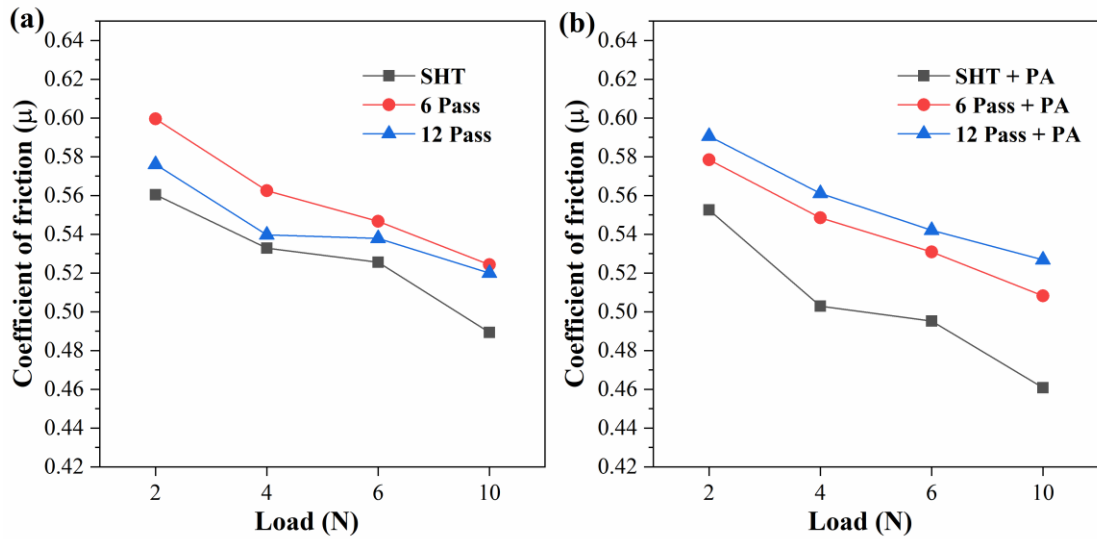


Figure 5.13 Variation of average coefficient of friction (COF) under different normal loads of AA2050 subjected to (a) MAF process, (b) after aging.

#### 5.2.1.2 Specific wear rate (SWR)

SWR, determined from volume losses obtained by 3D profilometer, is plotted as a function of processing condition of the samples and is shown in Figure 5.14. SWR is defined as the volume loss per unit length per unit-applied load, SWR realize the severity of the wear. It is evident from Figure 5.14(a), that for all processed conditions, with lower loads, higher is the SWR and with increase in applied load, SWR decreases. It is worth noting that, upon MAF processing, SWR increases and is maximum in 12 pass samples. This indicates that, MAF processing has led to decrease in wear resistance. It was also observed that with increase in MAF passes, the wear resistance further reduced.

In accordance to Archard equation, for ductile materials, the volume loss due to wear is given by

$$V = k \frac{LD}{3H} \quad \text{Equation 5.1}$$

Where, V is the volume loss due to wear, k is the wear constant, L is the normal applied load, D is the total sliding distance and H is the hardness of the sample. From Equation 5.1, it is apparent that, with increase in hardness, wear volume decreases. MAF processed samples have shown higher hardness accounting to the effect of strain hardening and refined grain structure as discussed in Section 4.2.1.1. Further, aging results in increase in hardness, as a result of precipitation, as observed in microhardness

studies (Section 4.2.1.2(Jagadeesh et al. 2023)). Hence, according to Equation 5.1, it is apparent to anticipate a decrease in volume loss rate or wear rate. However, it is evident from Figure 5.14(a) that, wear rate increases upon MAF processing and post-MAF aging. The reduction in wear resistance upon MAF is ascribed to the deficit of strain hardening ability thus leading to the formation of non-equilibrium grain boundaries, as discussed in Section 4.1. Similar findings of increases in wear rate after SPD processing in Al alloys, was reported (Kima et al. 2009; Talachi et al. 2011; Wang et al. 2011). Figure 5.14(b) shows the change in SWR, plotted for various sample conditions after subjecting to artificial aging. Similar trends of decrease in SWR with increase in applied load as seen in un-aged samples (Figure 5.14(a)), is also observed, after subjecting to artificial ageing. However, after aging, 12 pass MAF processed samples showed reduced SWR, compared to 6 pass processed samples, with SHT + aged samples showing least SWR. During aging of Al alloys, dislocations formed due to the induced strain act as nucleation sites for the precipitates to occur, resulting in strain relaxation in the alloy (Wang et al. 2021; Xie et al. 2022). Thus, the observed decrease in SWR in 12 pass samples is due to the effect of strain relaxation occurred during aging, due to formation of hardening precipitates.

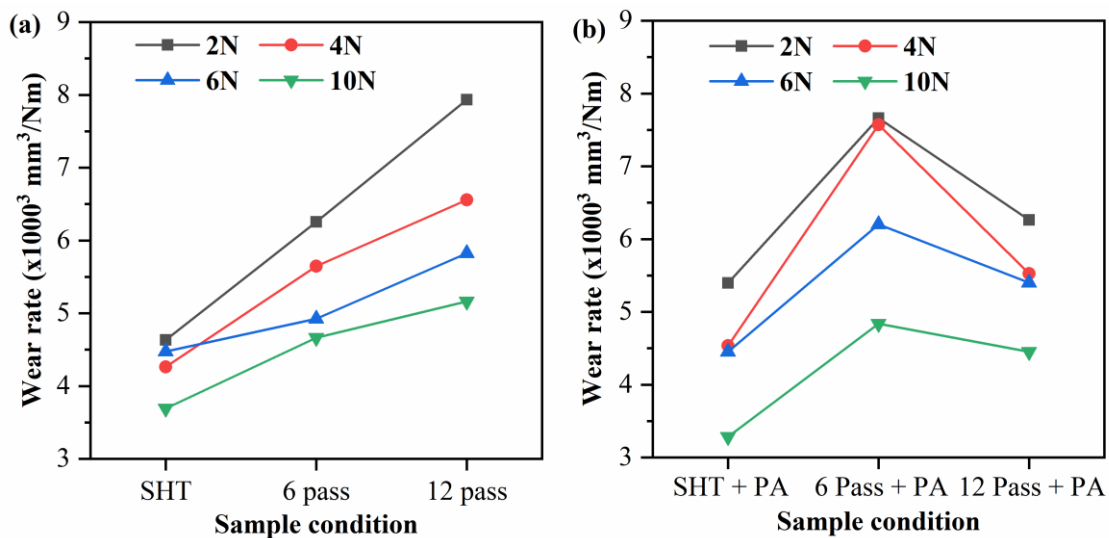


Figure 5.14 Variation of specific wear rate with various samples conditions for AA2050 Al alloy subjecting to (a) MAF process, (b) after aging.

### 5.2.2 Wear surface topography analysis through 3D profilometer

To determine the wear track width, depth, and volume loss during wear studies, worn surfaces of samples in all processed conditions under various nominal load conditions,

were analyzed using non-contact type 3D profilometer. 3D surface topography obtained from profilometry studies for all sample conditions under 2N and 10 N applied loads, is shown in the Figure 5.15. In all sample, for 2N normal loads, the width and depth of worn tracks were narrow and low, and samples under 10N normal loads showed wide and deep worn tracks. Increase in wear volume with increase in applied load, suggests severe deformation and is explained by Archard equation which gives a proportional relationship between applied load and wear volume (Archard 1953).

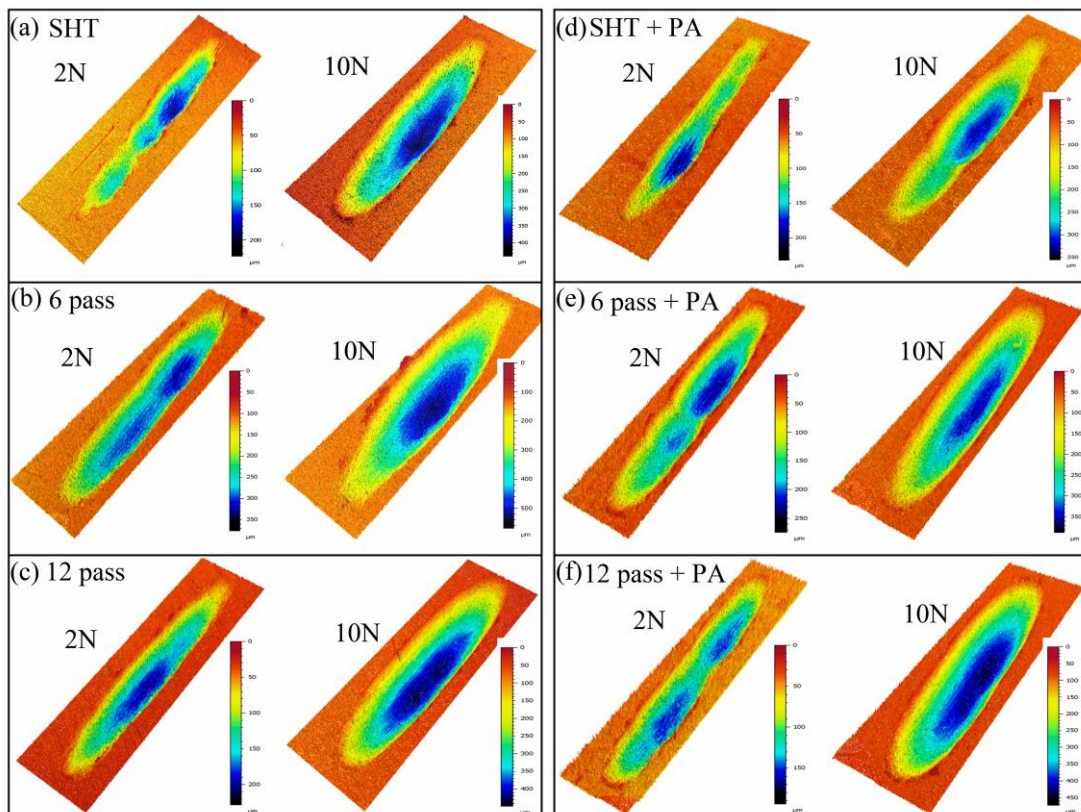


Figure 5.15 Axonometric projections of wear surface obtained using 3D profilometer in various processing and sample conditions.

### 5.2.3 Wear surface morphologies

Most of the Al alloys are wear resistant under lower loads and wear resistance deteriorates at higher load conditions. Hence, wear surfaces of samples processed at loading conditions at 2 and 10N was examined. Figure 5.16 shows the micrographs of worn surfaces of SHT, 6 and 12 pass MAF processed samples at 2N and 10N normal loads. Worn surface of SHT sample at 2N revealed clear evidence of formation of adhesive patches and abrasive grooves under the adhesive patches, indicating that the main wear mechanisms are adhesive and abrasion wear (Figure 5.16(a)). Formation of

similar adhesive layers in soft ductile materials are widely reported (Kuo and Rigney 1992; Rigney 2000; Wang et al. 2011). However, under higher applied load (10N), adhesive layer delamination or pull-off is clearly visible, as shown in Figure 5.16(b). Similar wear mechanism of adhesive and abrasive wear at lower load of 2N (Figure 5.16(c)) and adhesive, abrasive and delamination of adhesive layer was evident at higher load of 10N (Figure 5.16(d)) for 6 pass MAF processed sample. However, in 12 pass MAF processed sample, at lower load of 2N, small patches of adhesive layers with more dominating abrasive wear were evident, as seen in Figure 5.16(e). Further, at higher load of 10N, more dominantly abrasive wear mechanism with no signs of delamination was evident, as seen in Figure 5.16(f).

Micrographs of worn surfaces of peak-aged samples, after SHT, 6 and 12 pass MAF process, at 2N and 10N normal loads is shown in Figure 5.17. Not much significant differences were observed on peak-aged samples compared to unaged counterparts. SHT + aged sample surfaces revealed abrasion wear and adhesive wear at lower load conditions (2N) and abrasion, adhesive wear and delamination wear as the predominant wear mechanisms at higher loading conditions (10N), as seen in Figure 5.17(a,b) respectively. Similar wear characteristics were observed in 6 pass + aged samples as seen in Figure 5.17(c,d). However, 12 pass + aged samples show abrasion grooves and smaller adhesive patches at 2N loading conditions (Figure 5.17(e)) with dominating abrasion grooves at 10N load conditions (Figure 5.17(f)).

EDS maps, measured at various spots marked in Figure 5.16 and Figure 5.17 are shown in Figure 5.18. From EDS maps, it is evident that, surface under the delimitated layer shows elements corresponding to base AA2050 Al alloy with no sharper peaks of oxygen. However, EDS maps on adhesive layer shows the presence of high oxygen content (EDS spots 1, 2 and 5). Thus, confirming the formation of adhesive layer by compaction of oxidized abrasive particles. The friction at the interface of the surfaces leads an increase in temperature, resulting in oxidation of abrasive particles. Also, EDS maps does not show elements corresponding to counter ball surface depicting no transfer of counter ball material on to the wear surface.

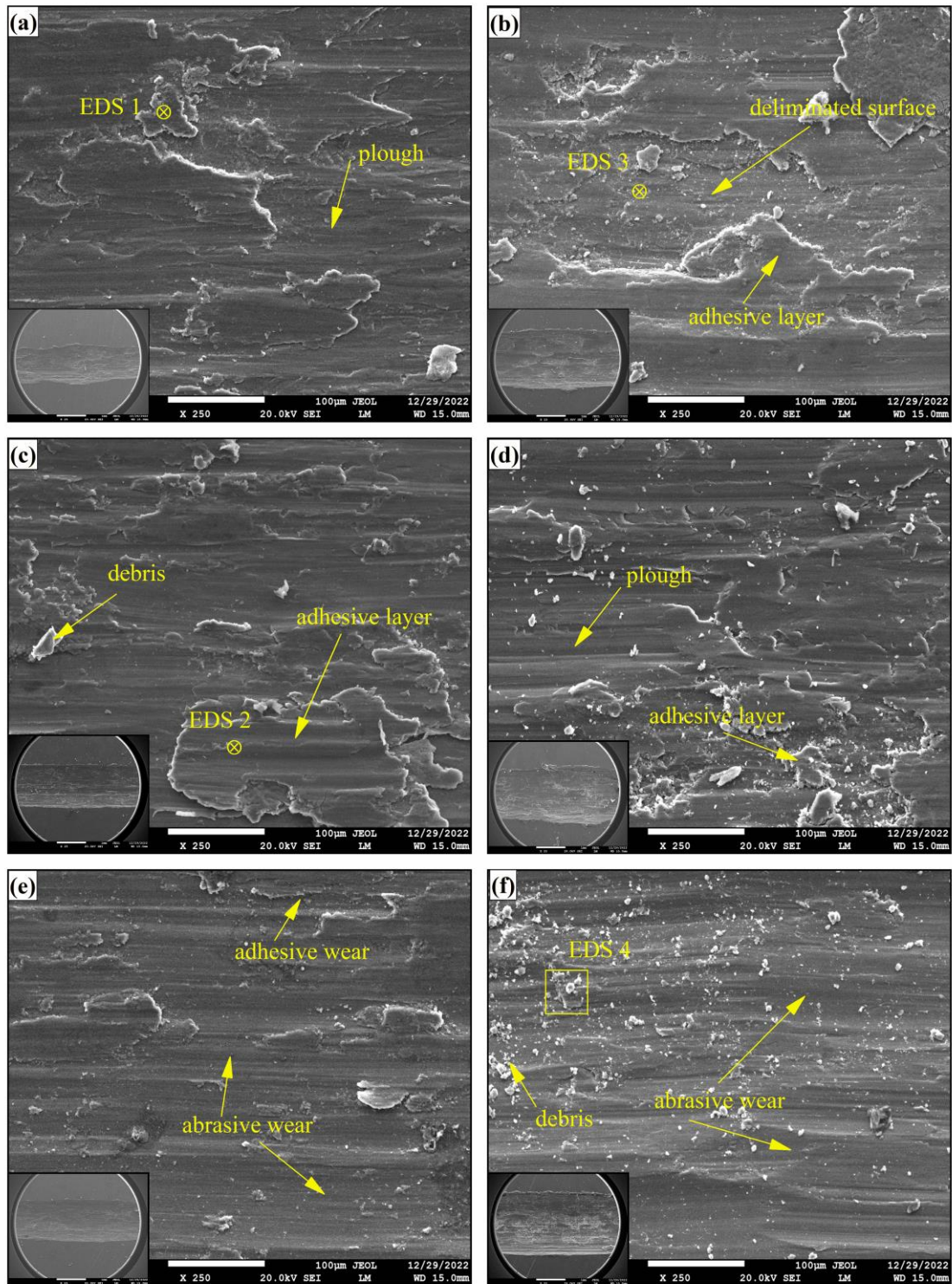


Figure 5.16 FESEM micrograph of AA2050 alloy wear track of SHT sample in (a) 2N, (b) 10N; 6 pass sample in (c) 2N, (d) 10N; and 12 pass sample in (e) 2N, (f) 10N loading conditions.

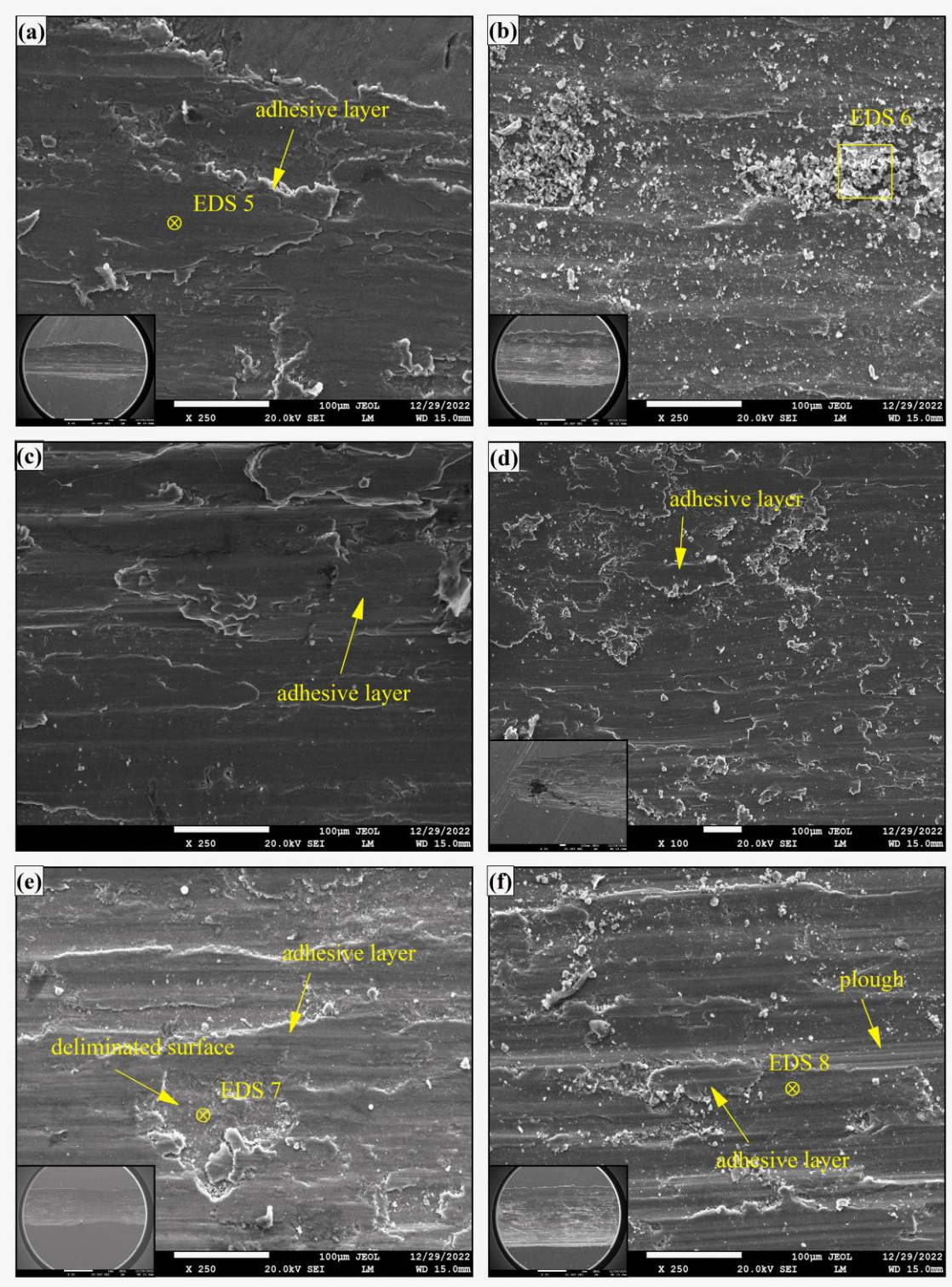


Figure 5.17 FESEM micrograph of AA2050 alloy wear track of SHT + PA sample in (a) 2N, (b) 10N; 6 pass + PA sample in (c) 2N, (d) 10N; and 12 pass + PA sample in (e) 2N, (f) 10N loading conditions.

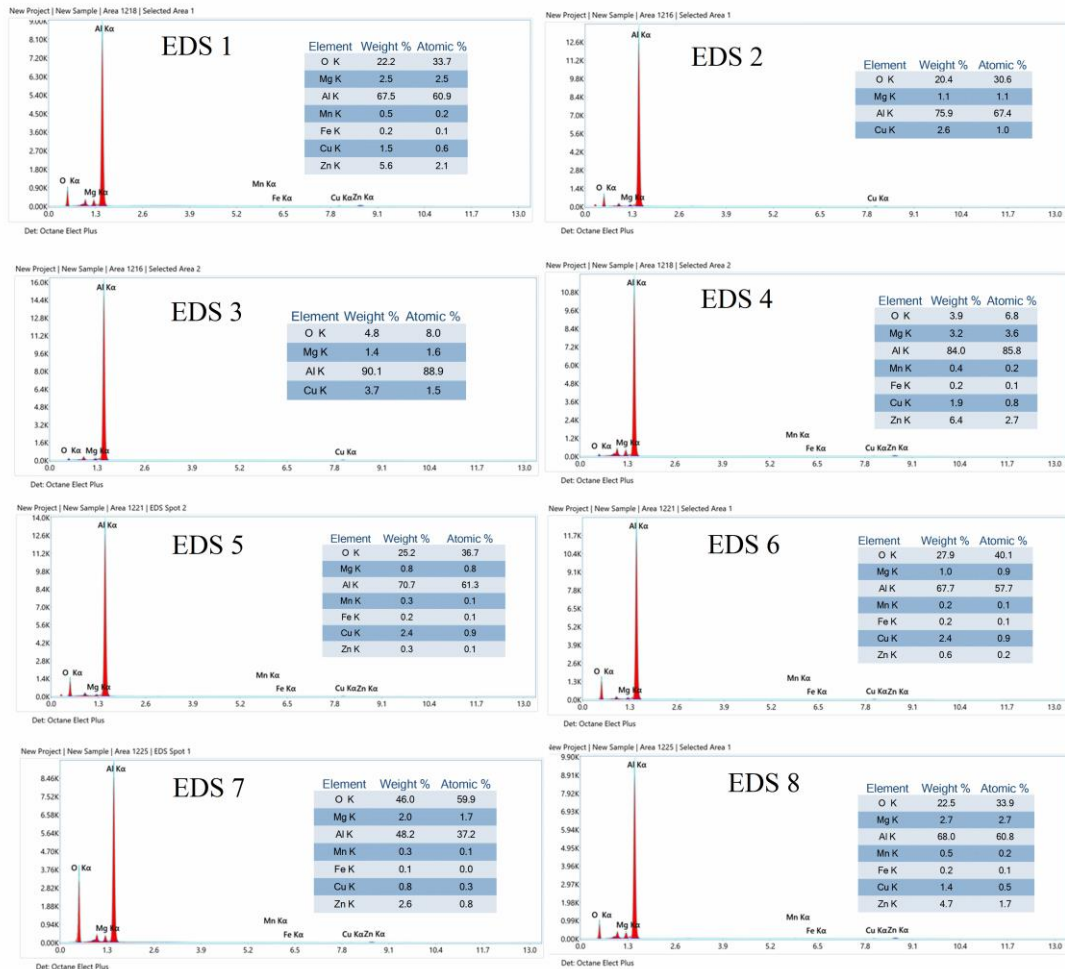


Figure 5.18 EDS maps measured at the various spots marked in Figure 5.16 and Figure 5.17.

### 5.2.4 Counter surface morphologies

Micrographs of counter ball surface obtained at regions under contact, after wear test, in SHT and SHT + aged samples are presented in Figure 5.19(a and b) respectively. Inserts represent the corresponding high-magnification images, respectively. Surface examination shows that the ball surface is partially covered by an adherent layer formed during wear tests. EDS results obtained of the adherent layer revealed the elements corresponding to Al-Cu-Li alloy with high oxygen content. The adherent layer formed could be due to two reason. Firstly, as a result of repetitive crushing of debris particles which are rich in oxygen content. Secondly, due to the transfer of delaminated layer from alloy surface onto the counter ball surface. Further, counter ball surface examination does not shown any traces of wear surface morphologies due to higher

hardness of steel balls compared to Al alloy, thus no traces of mechanical alloying. Furthermore, examination of counter ball surfaces after wear studies of MDF processed and MDF + aged as seen in Figure 5.20 shows similar surface characteristics as observed in SHT and SHT + peak aged sample conditions.

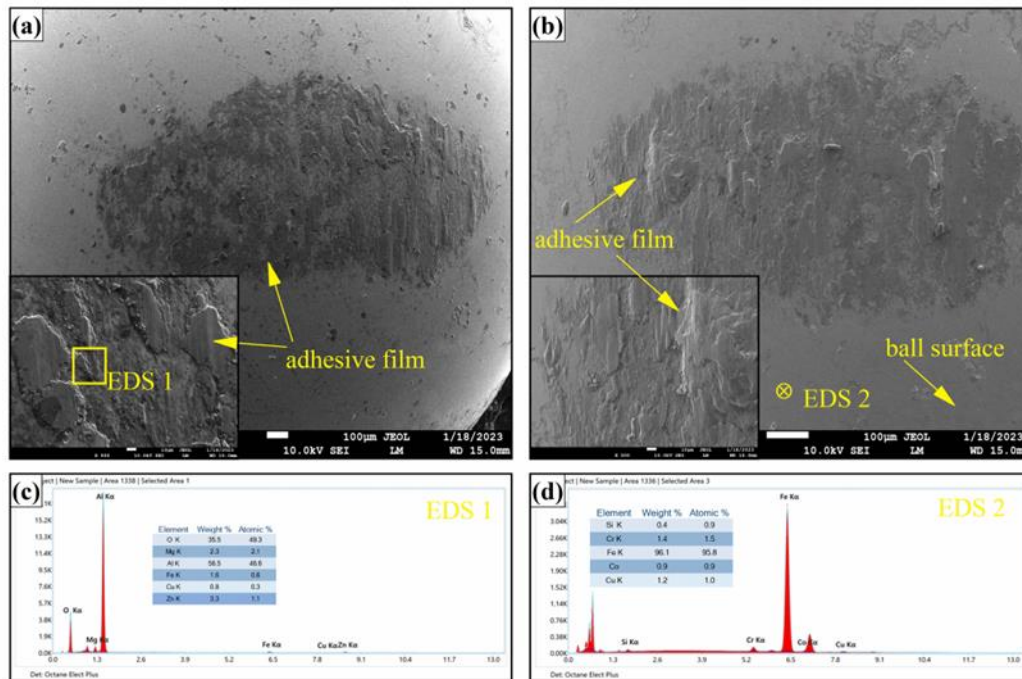


Figure 5.19 SEM micrographs of counter steel ball surface under 10 N load for (a) SHT sample, (b) SHT + aged sample and EDS spectrum for regions marked as (c) EDS 1 and (d) EDS 2.

### 5.2.5 Wear derbies characterization

SEM micrographs of wear debris formed during reciprocating wear tests of samples are shown in Figure 5.21. The debris were of various shapes and sizes in the form of flakes, chips and powders. Figure 5.21(a) represents the debris formed during the wear test of SHT sample at 10 N load condition and essentially consists of delaminated flakes produced by the fracture of compacted materials. EDS, at spot 1, as shown in Figure 5.21(e) further confirms the presence of oxide particles resulting from oxidation wear. Morphological observations of worn tracks and debris collected, clearly indicate delamination of sintered layer, formed due to oxidation wear conditions.

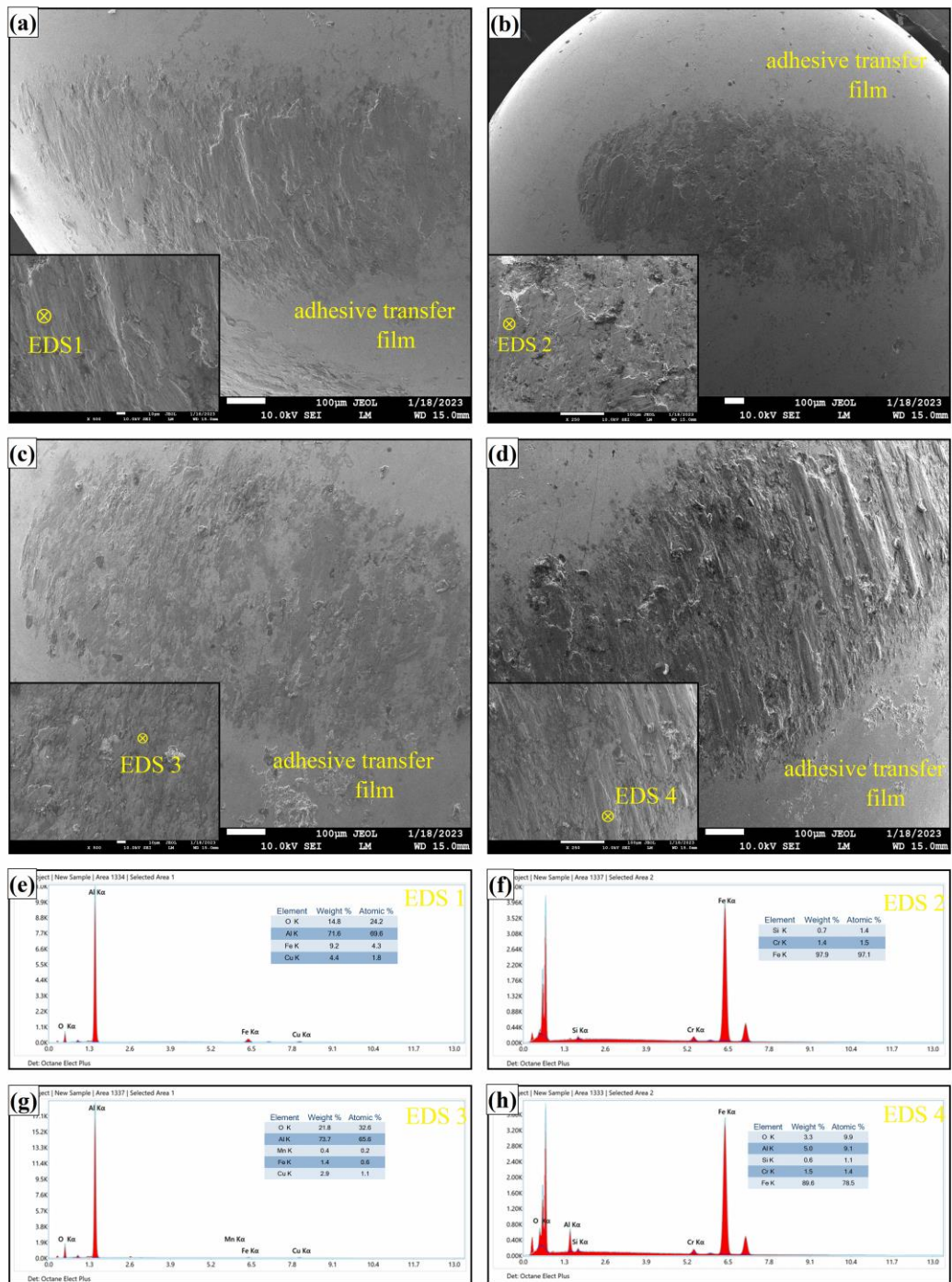


Figure 5.20 SEM micrographs of counter steel ball surface under 10 N load for (a) 6 pass, (b) 6 pass + peak aged, (c) 12 pass, (d) 12 pass + peak aged sample and EDS spectrum for regions marked as (e) EDS1, (f) EDS2, (g) EDS 3 and (h) EDS 4.

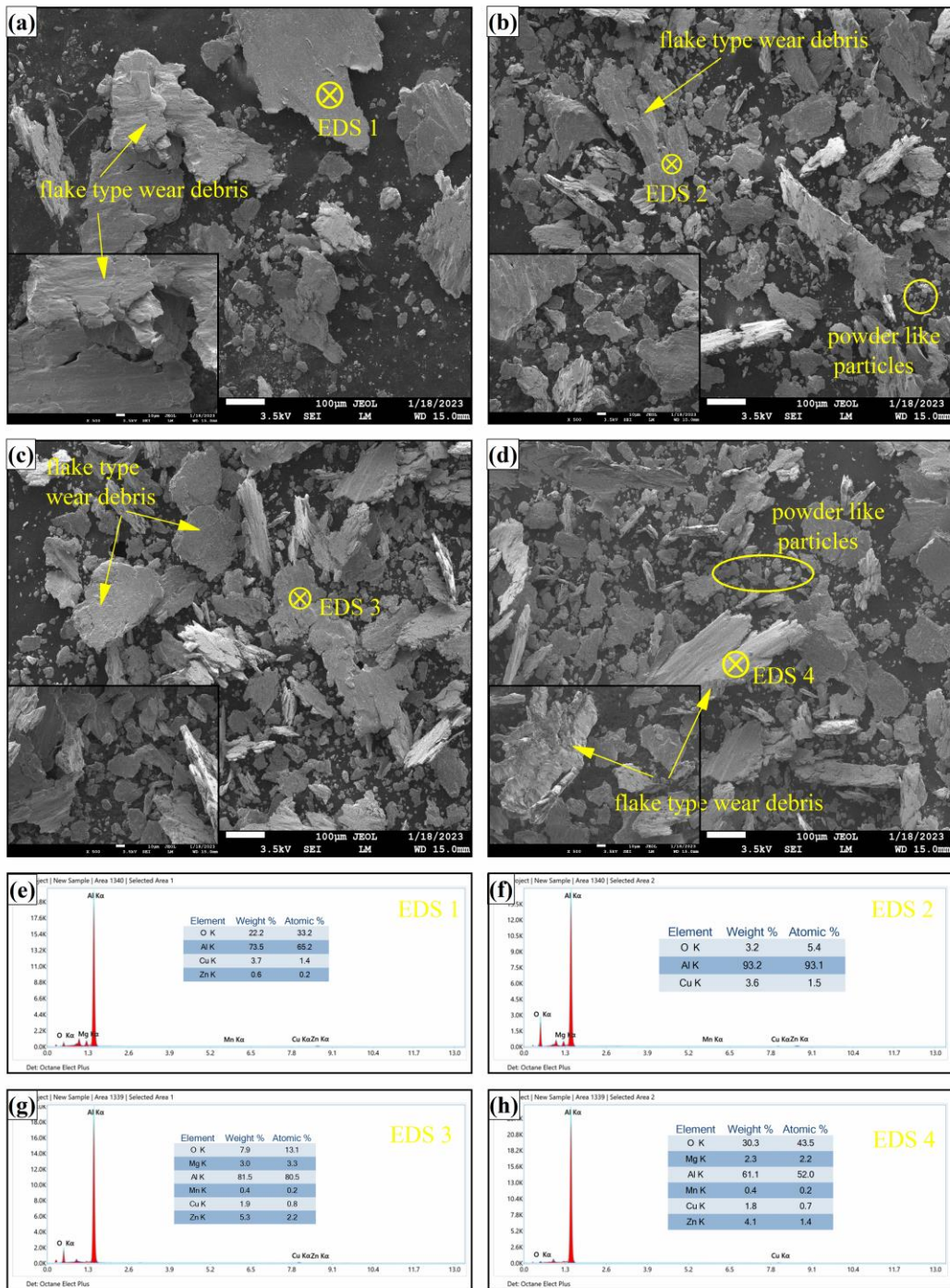


Figure 5.21 SEM micrographs of wear debris obtained during the reciprocating wear tests carried at load of 10N for (a) SHT, (b) 12 pass, (c) SHT + peak aged, and (d) 12 pass + peak aged sample conditions, (e-h) EDS plots of various spots.

## CHAPTER 6

### CONCLUSION

In the present work, effect of MAF and post MAF aging heat treatment on AA2050 Al-Cu-Li alloy is studied. Solution heat treated AA2050 alloy was subjected to MAF at 175 °C up to 12 pass (4 cycles). Also, several sets of SHT, 6 and 12 pass MAF processed samples were artificially aged at 125, 155, 175 °C up to 80 hours. Further, samples were extracted in various processed conditions and are subjected to several characterizations. The results obtained from these characterizations are critically analyzed, compared with the available literature and their implications are drawn. Important conclusions drawn from the present studies are as follows.

- Optical microscope images of SHT samples showed the presence of large elongated grains. Upon MAF, alloys developed fine grain microstructure with formation of large density of deformation bands, resulting in the non-uniform discontinuous grain boundaries. Density of deformation bands increased with increase in the number of MAF passes. Further, aging of SHT and MAF processed samples did not show any microstructural modifications, due to low temperature aging.
- EBSD micrographs further confirm fragmentation of coarse laminar grains, due to the formation of shear/deformation bands, at lower strains. Further these deformation bands transferred into high angle subgrains with gradual increase in misorientation angles at higher strains. At higher strains, fine grains are promoted at the intersections of shear bands due to continuous dynamic recrystallization.
- SHT sample shows average grain size of 74.3  $\mu\text{m}$ . MAF has resulted in a decrease in average grain size I.e, 38.81  $\mu\text{m}$  at 6<sup>th</sup> pass to 22.1  $\mu\text{m}$  at 12<sup>th</sup> pass samples respectively. Misorientation and GBCD results showed high fraction of HAGBs with misorientations distributed over wide range in SHT samples. After 6 and 12 pass of MAF, considerable increase in LAGBs with decrease in HAGBs was observed with average misorientation shifting towards lower angles.
- TEM studies revealed that MAF processed samples exhibited a high density of dislocations and deformation bands, as an account of substantial strain induced during MAF processing. SHT + peak aged samples displayed large continuous GB

precipitates and  $T_1$  precipitates at the grain interiors with PFZ formation at the grain boundaries. In contrast, artificial aging of MAF processed samples resulted in a distribution of fine  $T_1$  precipitates in the grain interiors.

- Macro texture studies showed that MAF has led to the development of strong S and Goss texture components in 6 pass sample. Further, S and Goss texture intensities were increased in 12 pass sample as a result of continuous change in compression axis between each MAF pass. Artificially peak aging of MAF processed and SHT samples did not result in any significant textural modifications.
- Microhardness tests shows a significant increase in hardness upto 6 passes from 80 HV to 142 HV, as a result of work hardening. A slight increase up to 153 HV after 12 passes was observed. 12<sup>th</sup> pass MAF processed sample showed maximum hardness of 173 HV during post deformation artificial aging.
- With increase in number of MAF passes, enhancement in strength with a trade-off in ductility was observed. This is because of effect of strain hardening and grain refinement. Meanwhile, artificial aging of MAF samples shows further increase in strengths, with slight increase in ductility, because of combined effect of grain refinement, strain hardening and precipitation hardening. Work hardening, high dislocation densities and grain refinement are primary causes of strength improvement in MAF samples. Apparently, precipitation hardening enhances material strength on MAF + aged samples.
- Fractography demonstrates mixed mode of fracture in differently processed samples, with SHT samples showing dominance of dimples. Upon MAF, with increase in number of MDF passes, fractured surface morphologies were dominated by ruptured regions and tearing ridges.
- in SHT and MAF samples, potentiodynamic polarization studies revealed the formation of corrosion film at initial corrosion potentials and breakdown at higher potentials. However, peak aged samples did not show corrosion film formation. Overall, an increase in corrosion resistance was observed in all sample upon peak aging, with 12 pass + peak aged samples showing better corrosion resistance.
- Corrosion mechanism, related to the peak aged samples, is attributed to galvanic coupling between cathodic constituent particles and the anodic matrix. SHT peak aged samples are characterized by intergranular corrosion as a result of cathodic

GB precipitates, while MAF peak aged samples exhibit intragranular corrosion due to the presence of fine, denser  $T_1$  precipitates in the grain interiors.

- Coefficient of friction was observed to be increasing upon MDF. However, with increase in normal loads, a reducing trend of COF was observed. Similar trends were also observed in aged samples with no much deviation in COF.
- Specific wear rate followed decreasing trend with increase in applied loads for all sample conditions. Interestingly, increase in SWR was observed upon MDF processing with an increasing trend with increase in number of MDF passes because of lack of strain hardening ability upon MDF process. However, upon aging, 12 pass MDF processed samples showed a reduction in SWR on account of strain relaxation during aging heat treatment.
- Varying normal loads have shown differences in wear mechanisms. At lower normal loads, adhesive and abrasion wear mechanism were evident. With increase in load, delamination wear with adhesive and abrasion wear was evident. Counter ball surface examinations showed no wear of the counter ball. However, transfer of alloy material on to ball surface with a larger content of oxygen was evident under all processed and load conditions. Wear debris was mainly of flakes type resulting from the delamination of a sintered/adherent layer with a minor amount of powder-like particles.

### **Scope for future work**

The broader objective of the present work was to enhance the properties of 3<sup>rd</sup> generation AA2050 Al-Cu-Li alloy. AA2050 has seen extensive applications in aerospace and aircraft applications and known to be a substitute for conventional 2XXX and 7XXX series Al alloys. To further enhance the properties, AA2050 alloy was SPD processes by MAF and also artificial aged. Crucial observations made during the study are presented in the above section. There is a scope for further work that can be carried out. As outlined in the preceding sections, our study has reported significant outcomes obtained through MAF and the subsequent artificial aging process. These observations underscore the potential for further investigations and improvements in overall development of AA2050 alloy. Some of the key areas where further research and experimentation can be undertaken, elucidating the potential benefits and applications are enlisted below:

- Al-Cu-Li is known to possess superior fatigue strengths compared to conventional Al alloys in T6 and T8 conditions. However, effect of pre deformation or SPD on fatigue strengths are not reported. Further, effect of aging heat treatment on MDF processed samples on fatigue behaviour remains unexplored. Hence, studies on fatigue properties are crucial in application point of view.
- Al-Cu-Li alloys possess inherent anisotropic properties because of strong texture. Our studies have shown a significant effect on texture upon MDF processing. The work can be further extended to study the effect of MAF on anisotropic behavior.
- Al alloys exhibit good thermal stability at higher temperatures. Strain-induced deformation can promote recrystallization under the influence of temperature. Hence, effect of MAF on thermal stability has to be explored.
- In the present study, wear properties of the alloy in different processed conditions were carried out in dry conditions at ambient temperature. Further the work can be extended to determine the wear behavior of the MAF processes and subsequently aged alloy in lubrication conditions as well as at higher temperatures.

## REFERENCES

- Abd El Aal, M. I., Mahallawy, N. El, Shehata, F. A., Abd El Hameed, M., Yoon, E. Y., and Kim, H. S. (2010). "Wear properties of ECAP-processed ultrafine grained Al-Cu alloys." *Mater. Sci. Eng. A*, 527(16–17), 3726–3732.
- Ahmed, B., and Wu, S. (2014). "Aluminum Lithium Alloys ( Al-Li-Cu-X ) -New Generation Material for Aerospace Applications." 440, 104–111.
- Aoba, T., Kobayashi, M., and Miura, H. (2017). "Microstructural evolution and enhancement of mechanical properties by multi-directional forging and aging of 6000 series aluminum alloy." *J. Japan Inst. Light Met.*, 67(7), 277–283.
- Archard, J. F. (1953). "Contact and rubbing of flat surfaces." *J. Appl. Phys.*, 24(8), 981–988.
- ASM Handbook, A. (1993). "Aluminum and Aluminum Alloys - Extrusion." *ASM Int.*, 117.
- Azushima, A., Kopp, R., Korhonen, A., Yang, D. Y., Micari, F., Lahoti, G. D., Groche, P., Yanagimoto, J., Tsuji, N., Rosochowski, A., and Yanagida, A. (2008). "Severe plastic deformation (SPD) processes for metals." *CIRP Ann.*, 57(2), 716–735.
- Bagherpour, E., Pardis, N., Reihanian, M., and Ebrahimi, R. (2018). "An overview on severe plastic deformation: research status, techniques classification, microstructure evolution, and applications." *Int. J. Adv. Manuf. Technol.*, 1647–1694.
- Balducci, E., Ceschini, L., Messieri, S., Wenner, S., and Holmestad, R. (2017). "Effects of overaging on microstructure and tensile properties of the 2055 Al-Cu-Li-Ag alloy." *Mater. Sci. Eng. A*, 707, 221–231.
- Bridgman, P. W. (1952). "Studies in Large Plastic Flow and Fracture: With Special Emphasis on the Effects of Hydrostatic Pressure." *New York-London McGraw-Hill*.
- Calderon, N., and Morris, D. G. (2008). "Refinement of precipitates and deformation substructure in an Al – Cu – Li alloy during heavy rolling at elevated temperatures." 492, 268–275.
- Cassada, W. A., Shiflet, G. J., and Starke, E. A. (1991a). "Mechanism of Al CuLi (T 1) nucleation and growth." *Metall. Trans. A*, 22(2), 287–297.
- Cassada, W. A., Shiflet, G. J., and Starke, E. A. (1991b). "The effect of plastic deformation on Al<sub>2</sub>CuLi (T 1) precipitation." *Metall. Trans. A*, 22(2), 299–306.
- Chang, Y. P., Chu, L. M., Liu, C. T., Wang, J. C., and Chen, K. W. (2021). "Effects of shot peening on the tribological properties of aluminum alloys with T6 treatment." *J. Phys. Conf. Ser.*, 2020(1).
- Chen, P. S., and Bhat, B. N. (2002). "Time-Temperature-Precipitation Behavior in Al-Li Alloy 2195." *NASATEchnical Rep*.
- Chen, P. S., Kuruvilla, A. K., Malone, T. W., and Stanton, W. P. (1998). "The Effects of Artificial Aging on the Microstructure and Fracture Toughness of Al-Cu-Li Alloy 2195." *J. Mater. Eng. Perform.*, 7(5), 682–690.

- Davis, J. (1999). *Corrosion of aluminum and aluminum alloys*. Asm International.
- Decker, B. F., Asp, E. T., and Harker, D. (2004). “Preferred Orientation Determination Using a Geiger Counter X-Ray Diffraction Goniometer.” *J. Appl. Phys.*, 19(4), 388.
- Decreus, B., Deschamps, A., Geuser, F. De, Donnadieu, P., Sigli, C., and Weyland, M. (2013a). “The influence of Cu/Li ratio on precipitation in Al-Cu-Li-x alloys.” *Acta Mater.*, 61(6), 2207–2218.
- Decreus, B., Deschamps, A., Geuser, F. De, Donnadieu, P., Sigli, C., and Weyland, M. (2013b). “The influence of Cu/Li ratio on precipitation in Al-Cu-Li-x alloys.” *Acta Mater.*, 61(6), 2207–2218.
- Deschamps, A., Decreus, B., Geuser, F. De, Dorin, T., and Weyland, M. (2013). “The influence of precipitation on plastic deformation of Al-Cu-Li alloys.” *Acta Mater.*, 61(11), 4010–4021.
- Dhal, A., Panigrahi, S. K., and Shunmugam, M. S. (2015). “Precipitation phenomena, thermal stability and grain growth kinetics in an ultra-fine grained Al 2014 alloy after annealing treatment.” *J. Alloys Compd.*, 649, 229–238.
- Dorin, T., Deschamps, A., Geuser, F. De, Lefebvre, W., and Sigli, C. (2014). “Quantitative description of the T 1 formation kinetics in an Al-Cu-Li alloy using differential scanning calorimetry, small-angle X-ray scattering and transmission electron microscopy.” *Philos. Mag.*, 94(10), 1012–1030.
- Duan, S., Guo, F., Wu, D., Wang, T., Tsuchiya, T., Matsuda, K., and Zou, Y. (2021). “Influences of pre-rolling deformation on aging precipitates and mechanical properties for a novel Al-Cu-Li alloy.” *J. Mater. Res. Technol.*, 15, 2379–2392.
- Dursun, T., and Soutis, C. (2014). “Recent developments in advanced aircraft aluminium alloys.” *J. Mater.*, 56, 862-871 Dursun, Tolga, and Costas Soutis. 2014. “Re.
- Dutta, H., and Pradhan, S. K. (2003). “Microstructure characterization of high energy ball-milled nanocrystalline V2O5 by Rietveld analysis.” *Mater. Chem. Phys.*, 77(3), 868–877.
- Elias, C. N., Meyers, M. A., Valiev, R. Z., and Monteiro, S. N. (2013). “Ultrafine grained titanium for biomedical applications: An overview of performance.” *J. Mater. Res. Technol.*
- Eswara Prasad, N., Gokhale, A. A., and Wanhill, R. J. H. (2013). *Aluminum : Lithium Alloys*. Butterworth-Heinemann, Elsevier.
- Ferrasse, S., Segal, V. M., Alford, F., Kardokus, J., and Strothers, S. (2008). “Scale up and application of equal-channel angular extrusion for the electronics and aerospace industries.” *Mater. Sci. Eng. A*, 493(1–2), 130–140.
- Furukawa, M., Berbon, P. B., Langdon, T. G., Horita, Z., Nemoto, M., Tsenev, N. K., and Valiev, R. Z. (1998). “Age hardening and the potential for superplasticity in a fine-grained Al-Mg-Li-Zr alloy.” *Metall. Mater. Trans. A*, 29(1), 169–177.
- Gable, B. M., Zhu, A. W., Csontos, A. A., and Jr, E. A. S. (2001). “The role of plastic

deformation on the competitive microstructural evolution and mechanical properties of a novel Al ± Li ± Cu ± X alloy.” 1.

Ghazani, M., and Shaban, M. (2014). “3D finite element study of temperature variations during equal channel angular pressing.” *J. Adv. Mater.*

Gupta, R., Srivastava, S., Kishor, N., and Panthi, S. K. (2016). “High leaded tin bronze processing during multi-directional forging : Effect on microstructure and mechanical properties.” 654, 282–291.

Heinz, A., Haszler, A., Keidel, C., Moldenhauer, S., Benedictus, R., and Miller, W. . (2000). “Recent development in aluminium alloys for aerospace applications.” *Mater. Sci. Eng. A*, 280(1), 102–107.

Hurley, P. J., and Humphreys, F. J. (2003). “The application of EBSD to the study of substructural development in a cold rolled single-phase aluminium alloy.” 51, 1087–1102.

Ikeda, M., Kashihara, K., and Aoba, T. (2019). “AZ31F Change in microstructures and mechanical properties during annealing of AZ31F magnesium alloy multi-directionally forged under decreasing temperature conditions.” 228–234.

Iwahashi, Y., Horita, Z., Nemoto, M., and Langdon, T. G. (1997). “An investigation of microstructural evolution during equal-channel angular pressing.” *Acta Mater.*, 45(11), 4733–4741.

Jafari, M., Enayati, M. H., Abbasi, M. H., and Karimzadeh, F. (2010). “Compressive and wear behaviors of bulk nanostructured Al2024 alloy.” *Mater. Des.*, 31(2), 663–669.

Jagadeesh, C., Nayaka, H. S., Ramesh, S., and Praveen, T. R. (2023). “Effect of Multi-directional Forging on the Evolution of Microstructural and Mechanical Properties of Lightweight Al-Cu-Li Alloy AA2050.” *J. Mater. Eng. Perform.*, 1–15.

Jazaeri, H., and Humphreys, F. J. (2004). “Quantifying recrystallization by electron backscatter diffraction.” *J. Microsc.*, 213(3), 241–246.

Jiang, B., Cao, F., Wang, H., Yi, D., Jiang, Y., Shen, F., Wang, B., and Liu, H. (2019). “Effect of aging time on the microstructure evolution and mechanical property in an Al-Cu-Li alloy sheet.” *Mater. Sci. Eng. A*, 740–741, 157–164.

Jiang, B., Wang, C., Song, R., Li, S., Cao, F., and Yi, D. (2022). “Effect of creep ageing on the corrosion behaviour of an Al–Cu–Li alloy.” *Corros. Sci.*, 202(September 2021), 110314.

Jiang, B., Wang, H., Tian, Y., Yi, D., Liu, H., and Hu, Z. (2020). “Effects of aging time on corrosion behavior of an Al-Cu-Li alloy.” *Corros. Sci.*, 173, 108759.

Jiang, F., Xu, X., Jiang, J., Tang, Z., Yan, N., Peng, Y., and Xu, P. (2018). “Coarsening of Al<sub>3</sub>Sc precipitates in Al-Mg-Sc alloys.” *J. Alloys Compd.*, 781, 209–215.

Kaigorodova, L. I., Rasposienko, D. Y., Pushin, V. G., Pilyugin, V. P., and Smirnov, S. V. (2018). “Influence of Severe Plastic Deformation on the Structure and Properties of Al – Li – Cu – Mg – Zr – Sc – Zn Alloy.” 119(2), 161–168.

- Kapil, R., Joshi, A., Jayaganthan, R., Gairola, S., and Verma, R. (2019). "Improvement of fracture toughness of ultra fine grained Al–Li 8090 alloy processed through multi axial forging." *Mater. Res. Express*, 6(8), 085064.
- Kapoor, R., Sarkar, A., Behera, A. N., and Sunil, S. (2020). "Materials Science & Engineering A Multi-axial forging of Nb-1wt .% Zr: Effect of annealing on microstructure and mechanical properties." *Mater. Sci. Eng. A*, 772(December 2019), 138805.
- Ke, D., Hengcheng, L., Qiumin, J., and Yun, T. (2010). "Effect of hot extrusion on mechanical properties and microstructure of near eutectic Al-12.0%Si-0.2%Mg alloy." *Mater. Sci. Eng. A*.
- Kecskes, L. J., Cho, K. C., Dowding, R. J., Schuster, B. E., Valiev, R. Z., and Wei, Q. (2007). "Grain size engineering of bcc refractory metals: Top-down and bottom-up-Application to tungsten." *Mater. Sci. Eng. A*.
- Khamsepour, P., and Kazeminezhad, M. (2020). "The effect of strain rate on multi-directional forged aluminum: Examining the experimental data and modeling results." *Mater. Chem. Phys.*, 239, 122022.
- Kim, J. K., Kim, H. K., Park, J. W., and Kim, W. J. (2005). "Large enhancement in mechanical properties of the 6061 Al alloys after a single pressing by ECAP." *Scr. Mater.*, 53(10), 1207–1211.
- Kim, M.-S., Kwon, S.-C., Kim, S.-T., Lee, S., Jeong, H.-T., and Choi, S.-H. (2019). "Effect of Forging Type on the Deformation Heterogeneities in Multi-Axial Diagonal Forged AA1100." *Met. Mater. Int.*, 25(3), 779–793.
- Kim, W. J., Chung, C. S., Ma, D. S., Hong, S. I., and Kim, H. K. (2003). "Optimization of strength and ductility of 2024 Al by equal channel angular pressing (ECAP) and post-ECAP aging." *Scr. Mater.*, 49(4), 333–338.
- Kim, W. J., Kim, J. K., Park, T. Y., Hong, S. I., Kim, D. I., Kim, Y. S., and Lee, J. D. (2002). "Enhancement of Strength and Superplasticity in a 6061 Al Alloy Processed by Equal-Channel-Angular-Pressing." 33(October), 3155–3164.
- Kim, Y. S., Ha, J. S., and Kim, W. J. (2004). "Dry sliding wear characteristics of severely deformed 6061 aluminum and AZ61 magnesium alloys." *Mater. Sci. Forum*, 449–452(I), 597–600.
- Kima, Y. S., Yua, H. S., and Shin, D. H. (2009). "Low sliding-wear resistance of ultrafine-grained Al alloys and steel having undergone severe plastic deformation." *Int. J. Mater. Res.*, 100(6), 871–874.
- Kotan, G., Tan, E., and Kalay, Y. E. (2013). "Homogenization of ECAPed Al 2024 alloy through age-hardening." 559(0921), 601–606.
- Kumar, S., Sarma, V. S., and Murty, B. S. (2007). "Influence of in situ formed TiB<sub>2</sub> particles on the abrasive wear behaviour of Al-4Cu alloy." *Mater. Sci. Eng. A*, 465(1–2), 160–164.
- Kuo, S. M., and Rigney, D. A. (1992). "Sliding behavior of aluminum." *Mater. Sci.*

*Eng. A*, 157(2), 131–143.

Langdon, T. G., Hasegawa, H., Komura, S., Utsunomiya, A., Horita, Z., Furukawa, M., and Nemoto, M. (1998). “Thermal stability of ultrafine-grained aluminum in the presence of Mg and Zr additions.” *Mater. Sci. Eng. A*, 265(1–2), 188–196.

Lee, S., Horita, Z., Hirose, S., and Matsuda, K. (2012). “Age-hardening of an Al–Li–Cu–Mg alloy (2091) processed by high-pressure torsion.” *Mater. Sci. Eng. A*, 546, 82–89.

Liang, W., Pan, Q., He, Y., Li, Y., Zhou, Y., and Lu, C. (2008). “Effect of aging on the mechanical properties and corrosion susceptibility of an Al–Cu–Li–Zr alloy containing Sc.” *Rare Met.*, 27(2), 146–152.

Mao, J., Kang, S. B., and Park, J. O. (2005). “Grain refinement, thermal stability and tensile properties of 2024 aluminum alloy after equal-channel angular pressing.” 159, 314–320.

Mazzini, S. G., and Caretti, J. C. (1991). “Effect of deformation at elevated temperature before age-hardening on the mechanical properties of 2024 commercial aluminium alloy.” *Scr. Metall. Mater.*, 25(8), 1987–1990.

Mishnaevsky, L., Levashov, E., Valiev, R. Z., Segurado, J., Sabirov, I., Enikeev, N., Prokoshkin, S., Solov’Yov, A. V., Korotitskiy, A., Gutmanas, E., Gotman, I., Rabkin, E., Psakh’E, S., Dluhoš, L., Seefeldt, M., and Smolin, A. (2014). “Nanostructured titanium-based materials for medical implants: Modeling and development.” *Mater. Sci. Eng. R Reports*.

Moradi, M., Nili-Ahmadabadi, M., and Heidarian, B. (2009). “Improvement of mechanical properties of AL (A356) cast alloy processed by ecap with different heat treatments.” *Int. J. Mater. Form.*

Murayama, M., Horita, Z., and Hono, K. (2001). “Microstructure of two-phase Al–1.7 at% Cu alloy deformed by equal-channel angular pressing.” *Acta Mater.*, 49(1), 21–29.

Nayan, N., Yadava, M., Gurao, N. P., Murty, S. V. S. N., Mahesh, S., Prasad, M. J. N. V., and Samajdar, I. (2019). “Sub-zero Temperature Dependence of Tensile Response of Friction Stir Welded Al–Cu–Li (AA2198) Alloy.” *Metall. Mater. Trans. A* 2019 513, 51(3), 1173–1182.

Noble, B., and Bray, S. . (1998). “On the  $\alpha(\text{Al})/\delta'(\text{Al}_3\text{Li})$  metastable solvus in aluminium–lithium alloys.” *Acta Mater.*, 46(17), 6163–6171.

Noble, B., and Thompson, G. E. (2010). “T1 (Al<sub>2</sub>CuLi) Precipitation in Aluminium–Copper–Lithium Alloys.” *Met. Sci. J.*, 6(1), 167–174.

Noda, M., Hirohashi, M., Funami, K., Suwahara, Y., and Kobayashi, M. (2002). “Effect of Strain Loading Process on Grain Refinement in Aluminum Alloy.” *J. Japan Inst. Met.*, 66(2), 101–108.

O Hall E. (1951). “The deformation and ageing of mild steel.” *Proc. Phys. Soc. Sect. B*, 64(9), 747.

- Ortiz-Cuellar, E., Hernandez-Rodriguez, M. A. L., and García-Sánchez, E. (2011). "Evaluation of the tribological properties of an Al-Mg-Si alloy processed by severe plastic deformation." *Wear*, 271(9–10), 1828–1832.
- Rambabu, P., Prasad, N. E., and Kutumbarao, V. V. (2017). "Aluminium Alloys for Aerospace Applications."
- Ramesh, S., Anne, G., Kumar, G., Jagadeesh, C., and Nayaka, H. S. (2021a). "Influence of Ball Burnishing Process on Equal Channel Angular Pressed Mg-Zn-Si Alloy on the Evolution of Microstructure and Corrosion Properties." *Silicon*, 13(5), 1549–1560.
- Ramesh, S., Anne, G., Naik, G. M., Jagadeesh, C., and Nayaka, H. S. (2021b). "Microstructural and mechanical characterisation of Al-Zn-Mg-Cu alloy processed by multi-directional cryo-forging." *Mater. Today Proc.*
- Ramesh, S., Nayaka, H. S., Sahu, S., Gopi, K. R., Shivaram, M. J., and Arya, S. (2019). "Influence of Multiaxial Cryoforging on Microstructural, Mechanical, and Corrosion Properties of Copper-Titanium Alloy." *J. Mater. Eng. Perform.*, 28(12), 7629–7641.
- Rao, P. N., Singh, D., Brokmeier, H.-G., and Jayaganthan, R. (2015). "Effect of ageing on tensile behavior of ultrafine grained Al 6061 alloy." *Mater. Sci. Eng. A*, 641, 391–401.
- Rigney, D. A. (2000). "Transfer, mixing and associated chemical and mechanical processes during the sliding of ductile materials." *Wear*, 245(1–2), 1–9.
- Rioja, R. J., and Liu, J. (2012). "The Evolution of Al-Li Base Products for Aerospace and Space Applications." *Metall. Mater. Trans. A*, 43(September), 3325–3337.
- Rodríguez, A., Calleja, A., López de Lacalle, L. N., Pereira, O., González, H., Urbikain, G., and Laye, J. (2019). "Burnishing of FSW Aluminum Al-Cu-Li components." *Metals (Basel)*, 9(2), 1–16.
- Saito, Y., Utsunomiya, H., Tsuji, N., and Sakai, T. (1999). "Novel ultra-high straining process for bulk materials—development of the accumulative roll-bonding (ARB) process." *Acta Mater.*, 47(2), 579–583.
- Sakai, G., Horita, Z., and Langdon, T. G. (2005). "Grain refinement and superplasticity in an aluminum alloy processed by high-pressure torsion." *Mater. Sci. Eng. A*, 393(1–2), 344–351.
- Sakai, T., Belyakov, A., Kaibyshev, R., Miura, H., and Jonas, J. J. (2014). "Dynamic and post-dynamic recrystallization under hot, cold and severe plastic deformation conditions." *Prog. Mater. Sci.*, 60, 130–207.
- Sarma, V. S., Wang, J., Jian, W. W., Kauffmann, A., Conrad, H., Freudenberger, J., and Zhu, Y. T. (2010). "Role of stacking fault energy in strengthening due to cryo-deformation of FCC metals." *Mater. Sci. Eng. A*.
- Segal, V. M. (1995a). "Materials processing by simple shear." *Mater. Sci. Eng. A*, 197(2), 157–164.
- Segal, V. M. (1995b). "Materials processing by simple shear." *Mater. Sci. Eng. A*,

197(2), 157–164.

Sergueeva, A. V., Stolyarov, V. V., Valiev, R. Z., and Mukherjee, A. K. (2001). “Advanced mechanical properties of pure titanium with ultrafine grained structure.” *Scr. Mater.*

Shanmugasundaram, T., Murty, B. S., and Subramanya Sarma, V. (2006). “Development of ultrafine grained high strength Al-Cu alloy by cryorolling.” *Scr. Mater.*, 54(12), 2013–2017.

Sitdikov, O., Sakai, T., Goloborodko, A., Miura, H., and Kaibyshev, R. (2005). “Grain refinement in coarse-grained 7475 Al alloy during severe hot forging.” *Philos. Mag.*, 85(11), 1159–1175.

Sitdikov, O., Sakai, T., Goloborodko, A., Miura, H., and Kaibyshev, R. (2006). “Grain refinement in coarse-grained 7475 Al alloy during severe hot forging.” 6435.

Socrates, G. (2003). “Texture analysis in materials science — 2Ed.” *Mater. Des.*

Sun, J., Zhang, L., Wu, G., Zhang, X., Rong, M., and Wang, C. (2019). “Microstructural characteristics and mechanical properties of extruded Al- 4Cu-1Li-0 . 4Mg-0 . 1Zr- x Zn alloy.” *Mater. Sci. Eng. A*, 743(September 2018), 223–232.

Suresh, K. S., Gurao, N. P., Singh D., S., Suwas, S., Chattopadhyay, K., Zhrebtsov, S. V., and Salishchev, G. A. (2013). “Effect of equal channel angular pressing on grain refinement and texture evolution in a biomedical alloy Ti13Nb13Zr.” *Mater. Charact.*, 82, 73–85.

Suresh, M., Sharma, A., More, A. M., Kalsar, R., Bisht, A., Nayan, N., and Suwas, S. (2019). “Effect of equal channel angular pressing ( ECAP ) on the evolution of texture , microstructure and mechanical properties in the Al-Cu-Li alloy AA2195.” *J. Alloys Compd.*, 785, 972–983.

Suresh, M., Sharma, A., More, A. M., Nayan, N., and Suwas, S. (2018). “Effect of Scandium addition on evolution of microstructure , texture and mechanical properties of thermo-mechanically processed Al-Li alloy AA2195.” *J. Alloys Compd.*, 740, 364–374.

Suwas, S., and Ray, R. K. (2014). *Deformation Textures*.

Talachi, A. K., Eizadjou, M., Manesh, H. D., and Janghorban, K. (2011). “Wear characteristics of severely deformed aluminum sheets by accumulative roll bonding (ARB) process.” *Mater. Charact.*, 62(1), 12–21.

Valiev, R. Z., Sabirov, I., Zhilyaev, A. P., and Langdon, T. G. (2012). “Bulk Nanostructured Metals for Innovative Applications.” *JOM*, 64(10), 1134–1142.

Valiev, R. Z., Zehetbauer, M. J., Estrin, Y., Höppel, H. W., Ivanisenko, Y., Hahn, H., Wilde, G., Roven, H. J., Sauvage, X., and Langdon, T. G. (2007). “The innovation potential of bulk nanostructured materials.” *Adv. Eng. Mater.*

Vigneshwaran, S., Sivaprasad, K., Narayanasamy, R., and Venkateswarlu, K. (2019). “Microstructure and mechanical properties of Al – 3Mg – 0.25 Sc alloy sheets produced

by cryorolling.” *Mater. Sci. Eng. A*, 740–741, 49–62.

Wang, C. T., Gao, N., Wood, R. J. K., and Langdon, T. G. (2011). “Wear behavior of an aluminum alloy processed by equal-channel angular pressing.” *J. Mater. Sci.*, 46(1), 123–130.

Wang, D., Yang, R., Huang, J., Liu, Z., Zhang, G., and Cai, B. (2021). “Effect of pre-strain on microstructure and micro-yield properties of Al-Cu-Li alloy.” *Micron*, 148.

Wang, X. M., Shao, W. Z., Jiang, J. T., Li, G. A., Wang, X. Y., and Zhen, L. (2020). “Quantitative analysis of the influences of pre-treatments on the microstructure evolution and mechanical properties during artificial ageing of an Al–Cu–Li–Mg–Ag alloy.” *Mater. Sci. Eng. A*, 782.

Wanhill, R. J. H., and Bray, G. H. (2013). “Aerostructural Design and Its Application to Aluminum-Lithium Alloys.” *Aluminum-Lithium Alloy. Process. Prop. Appl.*

Warren, A. S. (2004). “Developments and challenges for aluminum - A boeing perspective.” *Mater. Forum*, 24–31.

Wen, F., Chen, J., Han, S., Ye, J., Ren, J., Zhang, Y., Li, W., and Guan, R. (2022). “The initial corrosion behavior of Al–Cu–Li bicrystals: effect of misorientation and precipitates.” *J. Mater. Res. Technol.*, 18, 3716–3724.

Williams, D. B., and Edington, J. W. (2010). “The Precipitation of  $\delta'$  (Al<sub>3</sub>Li) in Dilute Aluminium–Lithium Alloys.” *Met. Sci.*

Wright, S. I., Nowell, M. M., and Field, D. P. (2011). “A review of strain analysis using electron backscatter diffraction.” *Microsc. Microanal.*, 17(3), 316–329.

Xia, L., Li, Y., Huang, M., Liu, J., and Hu, P. (2023). “Improved corrosion resistance of 2195 Al-Cu-Li alloy through T6I6 interrupted aging.” *J. Alloys Compd.*, 170055.

Xie, B., Huang, L., Xu, J., Su, H., Zhang, H., Xu, Y., Li, J., and Wang, Y. (2022). “Effect of the aging process and pre-deformation on the precipitated phase and mechanical properties of 2195 Al–Li alloy.” *Mater. Sci. Eng. A*, 832.

Yan, Y., Peguet, L., Gharbi, O., Deschamps, A., Hutchinson, C. R., Kairy, S. K., and Birbilis, N. (2018). “On the corrosion, electrochemistry and microstructure of Al-Cu-Li alloy AA2050 as a function of ageing.” *Materialia*, 1, 25–36.

Ye, F., Mao, L., Rong, J., Zhang, B., Wei, L., Wen, S., Jiao, H., and Wu, S. (2022). “Influence of different rolling processes on microstructure and strength of the Al–Cu–Li alloy AA2195.” *Prog. Nat. Sci. Mater. Int.*, 32(1), 87–95.

Ye, Z., Cai, W., Li, J., Chen, X., Zhang, R., Birbilis, N., Chen, Y., Zhang, X., Ma, P., and Zheng, Z. (2018). “Impact of Annealing Prior to Solution Treatment on Aging Precipitates and Intergranular Corrosion Behavior of Al-Cu-Li Alloy 2050.” *Metall. Mater. Trans. A*, 49(6), 2471–2486.

Zhang, X., Chen, Y., and Hu, J. (2018). “Recent advances in the development of aerospace materials.” *Prog. Aerosp. Sci.*, 97, 22–34.

Zhang, Y., Lv, Y., Liu, E., Cai, G., Pan, Q., Liu, B., Dong, Z., and Zhang, X. (2022).

“Materials Characterization Corrosion morphology evolution in 2A97-T6 Al-Cu-Li alloy : The influence of grain-stored energy.” *Mater. Charact.*, 191(July), 112169.

Zhao, Y. H., Liao, X. Z., Jin, Z., Valiev, R. Z., and Zhu, Y. T. (2004). “Microstructures and mechanical properties of ultrafine grained 7075 Al alloy processed by ECAP and their evolutions during annealing.” *Acta Mater.*, 52(15), 4589–4599.

Zhu, Z., Han, J., Gao, C., Liu, M., Song, J., Wang, Z., and Li, H. (2017). “Microstructures and mechanical properties of Al-Li 2198-T8 alloys processed by two different severe plastic deformation methods: A comparative study.” *Mater. Sci. Eng. A*, 681, 65–73.

Zou, Y., and Chen, X. (2018). “Corrosion behavior of 2198 Al – Cu – Li alloy in different aging stages in 3 . 5 wt % NaCl aqueous solution.”



### List of Publications based on Ph.D. Research Work

Sl. No.	Title of the paper	Authors (in the same order as in the paper. Underline the Research Scholar's name)	Name of the Journal/ Conference, Vol., No., Pages	Month, Year of Publication	Category*
1	“Effect of Multi-directional Forging on the Evolution of Microstructural and Mechanical Properties of Lightweight Al-Cu-Li Alloy AA2050”	<u>Jagadeesh C.</u> , Nayaka H. Shivananda, Ramesh S, and Praveen T. R.	Journal of Materials Engineering and Performance, <a href="https://doi.org/10.1007/s11665-023-07922-5">https://doi.org/10.1007/s11665-023-07922-5</a> (SCI Indexed)	January 2023	1
2	“Reciprocating wear behaviour of MDF processed and aged Al-Cu-Li alloy”	<u>Jagadeesh C.</u> , Nayaka H. Shivananda, and Prithivirajan S.	Materials Research Express	Under review	1
3	“Influence of MDF processing and Post MDF ageing treatment on Corrosion behaviour of AA2050 Al-Cu-Li Al alloy”	<u>Jagadeesh C.</u> , Nayaka H. Shivananda, and Gajanna Anne.	Materials Research Express	March 2024	1
4	“Investigations on the strengthening of lightweight aerospace Al-Cu-Li alloy processed through Multi-Axial Forging at cryogenic temperatures”	<u>Jagadeesh C.</u> , Nayaka H. Shivananda, And Ramesh S	NMD-ATM 2019, Trivendrum, Kerala	November 2019	4
5	“Investigation on microstructural and mechanical properties evolution of multi-axial forged (MAF) and post deformation aged lightweight Al-Cu-Li alloy”	<u>Jagadeesh C.</u> , and H Shivananda Nayaka	Advanced Materials and Manufacturing Technologies (AMMT-2023), Thiruvananthapuram, Kerala	February 2023	4

**Category\***

1 : Journal paper, full paper reviewed

3 : Conference/Symposium paper, full paper reviewed

5 : Others (including papers in Workshops, NITK Research Bulletins, Short notes etc.)

(If the paper has been accepted for publication but yet to be published, the supporting documents must be attached.)

2 : Journal paper, Abstract reviewed

4 : Conference/Symposium paper, abstract reviewed



## Bio Data

### (a) Personal details

1	Name	Jagadeesh Chandrappa
2	Correspondence address	#69, Chokkasandra Village, Huskur post, Anekal Taluk, Bangalore Rural- 560099
3	Contact details	Mobile: 9164834595 E-mail: <a href="mailto:jagadeeshc807@gmail.com">jagadeeshc807@gmail.com</a>
4	Institution	National Institute of Technology karnataka
5	Date of Birth	5 <sup>th</sup> September 1991

### (b) Educational Qualification (Undergraduate Onwards)

Sl. No.	Degree	Year	Specilization	Institution/University	Percentage scored
1	Ph.D	2020	Mechanical Engineering	National Institute of Technology Karnataka	-
2	Master of Engineering	2016	Manufacturing science and engineering	Bangalore University	82.5
3	Bachelor of Engineering	2014	Mechanical Engineering	Visvesvaraiah Technological University	70

### (c) Publications (List of publications, in year wise descending order)

Sl. No.	Autohor(s)	Title	Name of the journal	Volume , Page No. and year.
1	<b>C Jagadeesh,</b> H. Shivananda Nayaka, S Ramesh, TR Praveen	Effect of Multi-directional Forging on the Evolution of Microstructural and Mechanical Properties of Lightweight Al-Cu-Li Alloy AA2050	Journal of Materials Engineering and Performance	1-15, 2023

2	<b>C Jagadeesh</b> , S Prithivirajan, S Ramesh, G Anne	On the microstructure, texture and electrochemical properties of severely deformed and artificially aged lightweight AA2050 Al-Cu-Li alloy	Materials Research Express	11, 3, 2024
3	Maruthi Prashanth B H, Ramesh S, P S Shivakumar Gouda, Gajanan M Naik, Priyaranjan Sharma, <b>C Jagadeesh</b> , Mahantesh M Math and Gajanan Anne	Impact of ply stacking sequence on the mechanical response of hybrid Jute-Banana fiber phenoplast composites	Materials Research Express	11, 5, 2024
4	S. Aditya, Gajanan A, Ramesh, Priyaranjan Sharma, <b>C Jagadeesh</b> , Lingaraj, Gajanan Naik & G. Divya Deepak	Enhancing surface characteristics of Mg-Zn-Sr alloy through cryo-ball burnishing; modeling and experimentation	Journal of Mechanical Science and Technology	38, 1175-1185, 2024
5	S Ramesh, Goutham Kumar, <b>C Jagadeesh</b> , Gajanan Anne, H Shivananda Nayaka	Effect of Equal Channel Angular Pressing on Properties Evaluation of Biodegradable Mg-Zn-Mn Alloy	Journal of Bio-and Tribo-Corrosion	7, 1-13, 2021
6	S Ramesh, Gajanan Anne, Gajanan M Naik, <b>C Jagadeesh</b> , H Shivananda Nayaka	Microstructural and mechanical characterisation of Al-Zn-Mg-Cu alloy processed by multi-directional cryo-forging	Materials Today: Proceedings	46, 5752-5756, 2021
7	S Ramesh, Gajanan Anne, Goutham Kumar,	Influence of ball burnishing process on equal channel angular pressed Mg-Zn-Si	Silicon	13, 1549-

	<b>C Jagadeesh,</b> H Shivananda Nayaka	alloy on the evolution of microstructure and corrosion properties		1560, 2021
--	---	---	--	---------------

Jagadeesh C